Modelling and Mass Optimisation of an Aluminium Honeycomb Impact Attenuator

Master thesis

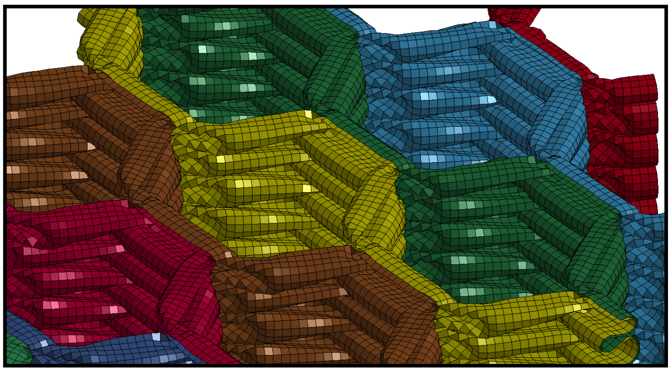

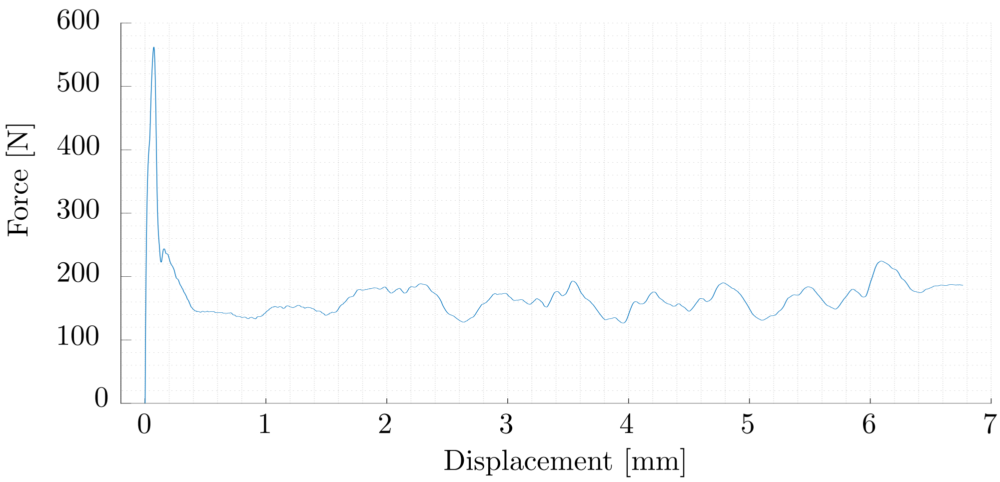

Group 14/23B
Design of Mechanical Systems
Aalborg University
3rd June 2020

The Faculty of Engineering and Science
Design of Mechanical Systems
Fibigerstræde 16
9220 Aalborg Øst
http://www.m-tech.aau.dk/

AALBORG UNIVERSITY
STUDENT REPORT

Title:
Modelling and Mass Optimisation of an Aluminium Honeycomb Impact Attenuator

Project:
DMS4 — Master thesis

Project period:
03.02.20 - 03.06.20

Project group:
14/23B

Supervisors:
Jørgen Asbøll Kepler
Benny Endelt

Participants:

Nikolaj Broberg

Christian Dam Simonsen

Jens Bonderup Sørensen

Pages: 116
Appendices: 7

Synopsis:

In this project, an optimised impact attenuator is made for AAU Racings Formula Student race car, based on a simulation of a simplified honeycomb structure and as a continuation of [Simonsen et al., 2019]. After analysing several materials, aluminium honeycombs are found to be the most suitable material. Dynamic experiments are conducted on aluminium honeycombs with a drop test, from which it is concluded that dynamic loads are insignificant and are therefore negligible in the model.
The model is developed using LS-DYNA based on knowledge obtained in [Simonsen et al., 2019] regarding stability and plasticity, and the deformation mode of honeycombs described by [Wierzbicki, 1983]. This leads to the modelling challenge of simulating the partial break of the adhesive between the cells of the honeycomb. The contact formulation used to model the adhesive is found troublesome to implement, as the contact becomes unstable. Thus, to thoroughly understand how it works, it is implemented on simpler models. This enables the implementation of the contact formulation on a honeycomb, which gives satisfactory results compared to the dynamic experiments and the honeycomb data sheet.
From this model a meta-model of the mean load during deformation is created using the Response Surface Method. The meta-model models the mean load as a function geometric parameters, which is used as a constraint for a minimisation of the mass.
To minimise the mass the MATLAB algorithm "fmincon" is used, where an optimal design is found. The optimised design has the theoretical mass of 1.29 kg, which is a reduction of 62 % of the current design.

Resumé

Dette projekt er en fortsættelse af [Simonsen et al., 2019], der omhandler modellering af et kvadratisk aluminium rørprofil i kompression. Derfor vælges det at arbejde videre med stødabsorberende strukturer. Specifikt vælges det at designe stødabsorberen på AAU Racings Formula Student racerbil.

For at gøre dette, udføres analyser og quasistatiske kompressionstest på forskellige materialer. I disse test findes det, at aluminium honeycomb er det bedst egnet materiale til at designe stødabsorberen. For at bestemme, hvor stor betydning dynamiske effekter har for aluminium honeycomb, bygges en forsøgsopstilling, hvor dynamiske laster kan pålægges. I disse eksperimenter findes det, at de dynamiske effekter er uden betydning, ved sammenstødshastighed på 7 m/s, hvilket betyder, at effekterne ikke er nødvendige at modellere.

Modellen er udviklet med grundviden, som opnås i [Simonsen et al., 2019] vedr. plasticitet og stabilitet i LS-DYNA. Modellen er primært baseret på [Wierzbicki, 1983]'s hypotese: At det kræver mindre energi at delvist bryde limsamlingen i honeycomben, end at deformere cellevæggene, hvis den ikke bryder. Dette leder til hovedudfordringen i modelleringen i dette projekt, som er at simulere et delvist brud af limsamlingen mellem honeycombens celler. For at simulere dette, anvendes den kommercielle kode LS-DYNA. LS-DYNA har flere kontaktformulering, der kan simulere limsamlinger, hvor en kontakt formulering, der er passende til dette problem, findes. Det findes, at kontaktformuleringen er svær at implementere, fordi kontakterne bliver ustabile. Det vælges derfor at implementere formuleringen på mere simple modeller, for at få en gennemgående forståelse af formuleringen. Her findes en uoverensstemmelse mellem manualen fra LS-DYNA [Livermore Software Technology Corporation, 2019] og resultaterne fra simuleringerne. Ved forståelse af hvordan kontakt formuleringen virker, er det muligt at implementere den på honeycomb modellen. Honeycomb modellen simplificeres til en "Y" sektion, hvilket er muliggjort af honeycombens symmetri. Efter nogle få iterationer med forskellige materiale modeller, giver simuleringen tilfredsstillende resultater, når de sammenlignes med eksperimenter og databladet.

Efterfølgende er modellen af "Y" sektionen sammenlignet med en honeycomb model bestående af syv celler, hvilket også giver tilfredsstillende resultater. Foruden dette, undersøges [Wierzbicki, 1983]'s hypotese, hvortil der konkluderes ved brug af modellen, at det kræver en væsentlig mindre mængde energi at deformere en honeycomb, hvis det delvise brud af limsamlingen tages med i simuleringen.

Dernæst bruges modellen til at lave en metamodel af responsfladen af middelkraften, som det kræver at deformere "Y" sektionen, afhængig de geometriske parametre der skal optimeres. Slutteligt bruges metamodellen til formoptimeringen af honeycomb'en underlagt krav vedr. geometri og ydeevne, opstillet af Formula Student [FSG, 2020]. Det findes, at massen kan reduceres med 2.13 kg, som er 62 % mindre end det nuværende design.

Preface

This master thesis is made by three students from Design of Mechanical Systems at Aalborg University. The thesis covers 30 ECTS points pr. student. The thesis is a continuation of a previous project, however, it will be clearly stated whenever previous work is presented. Sincere appreciation is expressed towards Jørgen Asbøll Kepler and Benny Endelt for supervision of the project.

Reading guide and notation

The Harvard method of referencing is used with the syntax [Last name, Year]. A complete list of references is found in the end of the report. The references for books are presented with Author, Title, Edition, and Publisher. Internet references are presented with Author, Title, URL, and date of access.

The table of content presents chapters with Arabic numerals and appendixes with Latin letters.

Figures and tables are numbered with chapter and consecutive numbers e.g "Figure 1.1" for first figure of chapter 1, "Figure 1.2" for the second figure and so on. Description texts are found beneath each figure and table.

In graphs with multiple curves, the plots are marked with symbols along the curve. In the caption it is stated how many data points there is between the symbols. This is stated by $i\# =$ number of data points.

Contents

1 — Introduction

The objective of this master thesis is to model and optimise an impact attenuator. The thesis is a continuation of the 3^{rd} semester project "Analysis and Modelling of the Deformation Behaviour of Metallic 2D Cellular Structures" [Simonsen et al., 2019]. In that project, the deformation behaviour of 2D cellular structures in compression was analysed, and a FEM model of the mechanisms was developed for a hollow square profile. The analysis and the model were done in order to design an impact attenuator using the manufacturing technique: Powder metal extrusion. However, it was found that the powder metal extrusion was ill-suited for manufacturing impact attenuators at the current time. Thus, a series of experiments are conducted on different materials and structures to analyse their deformation behaviours to find a material or structure which is more suitable as an impact attenuator. Firstly, the design case is presented and analysed.

1.1 Impact attenuator

The impact attenuator is designed for AAU Racing's Formula Student race car, G8. Formula Student is a worldwide community where several engineering competitions cooperate in formulating a joint framework for the competitions. The competitions vary slightly in rule-set, however, characteristic for the competitions is that, university students design, manufacture, and compete in single-seat, open-wheel formula style race cars. The students compete in classical racing events; drag, skid-pad, sprint, and endurance, while also participating in static events; design, cost, and business plan presentation. The team is judged and evaluated based on objectives such as the understanding of the manufacturing processes and costs associated with the construction of the different parts, as well as choices made in the design of the different parts. AAU Racing's current car is shown in Figure 1.1.

Figure 1.1: AAU Racing's race car, G8, at Formula Student Austria 2019.

The impact attenuator is a deformable, energy-absorbing device mounted on the anti intrusion plate in front of the car. The anti intrusion plate is a 1.5 mm thick steel plate welded onto the front bulkhead, which is a planar structure that is comprised of four 25 mm × 25 mm × 1.5 mm square tubes welded together, providing protection for the driver's feet. The front bulkhead, anti intrusion plate and impact attenuator, are shown in Figure 1.2.

Currently, AAU Racing is using the impact attenuator on the left of Figure 1.2. This impact attenuator is a standard model purchased from an external vendor, Formula Seven, that specialises in components for Formula Student teams [Formula Seven, 2020]. The design specifications of the current impact attenuator are seen in Figure 1.3.

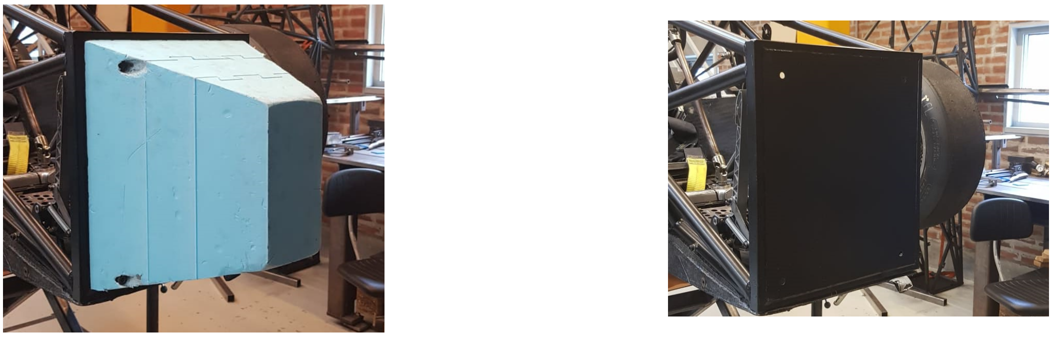

Figure 1.2: Front of G8 with front bulkhead. *Left:* Formula Seven's standard impact attenuator. *Right:* Anti intrusion plate.

Dimension	Abbreviation	Size	Unit
Width	w	355.6	[mm]
Height	h	254.0	[mm]
Length	l	304.8	[mm]
Mass	m_{IA}	0.700	[kg]

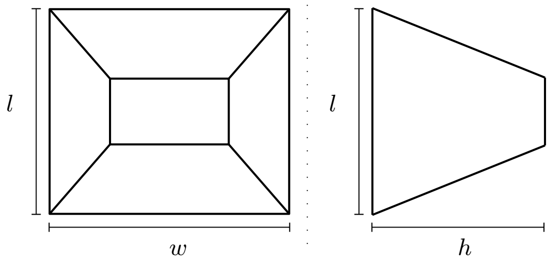

Figure 1.3: Dimensions of standard impact attenuator from Formula Seven.

Being a standard impact attenuator, it is not optimised for a specific car. This means that the size of the front bulkhead and the anti intrusion plate needs to be designed with respect to the impact attenuator. This is important because the masses of the front bulkhead and the anti intrusion plate are quite significant compared to the mass of the impact attenuator. Assuming that the impact attenuator and anti intrusion plate spans to the centre line of the front bulkhead, the mass of the front bulkhead using the standard impact attenuator is approximately:

$$\begin{aligned} A_{FBH} &\approx (25\,\text{mm})^2 - (25\,\text{mm} - 2\cdot 1.5\,\text{mm})^2 = 141\,\text{mm}^2 \\ L_{FBH} &\approx 2\,(w+l) \approx 1{,}321\,\text{mm} \\ m_{FBH} &\approx A_{FBH}\,L_{FBH}\,7{,}800\,\text{kg/m}^3 \approx 1.45\,\text{kg} \end{aligned} \tag{1.1}$$

And the mass of the anti intrusion plate is approximately:

$$m_{AIP} \approx w\,l\,1.5\,\text{mm}\cdot 7{,}800\,\text{kg/m}^3 \approx 1.27\,\text{kg} \tag{1.2}$$

i.e. the total mass of the impact attenuator, front bulkhead, and anti intrusion plate is:

$$m_{total} = m_{IA} + m_{FBH} + m_{AIP} \approx 3.42\,\text{kg} \tag{1.3}$$

Thus, the mass of the impact attenuator only represents 20% of the total mass.

$$\frac{m_{IA}}{m_{total}} \approx 20\% \tag{1.4}$$

With this, it is clear that the front bulkhead and anti intrusion plate has a significant influence on the total mass and by changing the length and width of the impact attenuator, a large amount of mass can be saved.

1.2 Formula Student rules and constraints

Choosing a Formula Student race car as the design task is advantageous as there is a well-defined set of rules regarding geometric restrictions, strength requirements, and methods of verifying the design experimentally. It is chosen to use the 2020 rules for the competition "Formula Student Germany" [FSG, 2020].

1.2.1 Geometric restrictions

The minimum geometric restrictions for the impact attenuator, as given by the rules [FSG, 2020], are tabulated in Figure 1.4. No restrictions on the maximum dimensions are given in [FSG, 2020] for the impact attenuator. However, it is stated that:

"*All aerodynamic devices must not extend further forward than 700 mm from the front of the front tires.*" [FSG, 2020]

This is illustrated on Figure 1.4. This rule determines the maximum distance that the non-structural bodywork can extend beyond the front bulkhead, which the impact attenuator is prohibited from being an integrated part of. Thus, some additional space is needed for the non-structural bodywork in front of the impact attenuator. The additional space is needed for tapering the non-structural to a tip which is considered doable with 100 mm. For simplicity, it is chosen to use the G8 chassis as a basis for the design, i.e. the distance from the front of the front tires to the front bulkhead is fixed to be 243 mm. Thereby setting a restriction on the maximum height of the impact attenuator to 357 mm.

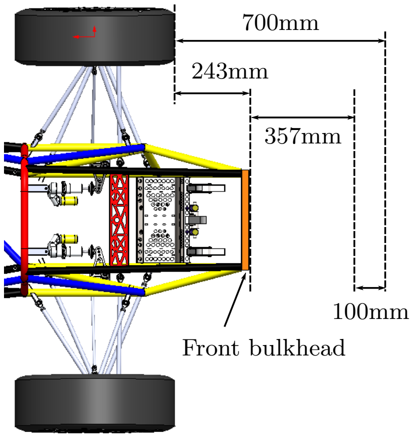

Dimension	Abbreviation	Size	Unit
Min width	w_{min}	200	[mm]
Min length	l_{min}	100	[mm]
Min height	h_{min}	200	[mm]
Max height	h_{max}	357	[mm]

Figure 1.4: Impact attenuator geometric restrictions. *Left:* Front of G8 without bodywork and with derivation of maximum height. *Right:* Table of minimum and maximum dimensions of the impact attenuator.

1.2.2 Strength requirements and testing

According to the rules, testing of the designed impact attenuator is required. In [FSG, 2020] the test method and requirements are stated as.

"The IA assembly (impact attenuator assembly), when mounted on the front of a vehicle with a total mass of 300 kg and impacting a solid, non-yielding impact barrier with a velocity of impact of 7 m/s, must meet the following requirements:" [FSG, 2020]

- The deceleration never exceeds 40 g.
  - i.e. the peak load, $P_p \leq 40 \cdot 9.81\,\mathrm{m/s^2} \cdot 300\,\mathrm{kg} \approx 120\,\mathrm{kN}$
- The average deceleration does not exceed 20 g.
  - i.e. the mean load, $P_m \leq 20 \cdot 9.81\,\mathrm{m/s^2} \cdot 300\,\mathrm{kg} \approx 60\,\mathrm{kN}$
- All kinetic energy in the test must be absorbed.
  - i.e. the energy absorption, $W \geq \frac{1}{2} \cdot 300\,\mathrm{kg} \cdot (7\,\mathrm{m/s})^2 = 7{,}350\,\mathrm{J}$

Where the combined impact attenuator and anti intrusion plate are denoted as the "impact attenuator assembly". During the test, it is also required that the impact attenuator assembly must be attached to a test fixture that has a geometry, stiffness and strength that is representative of the chassis. In practice, the test fixture is typically constructed as a copy of the front bulkhead supported by at least 50 mm of steel tubing resembling the chassis members supporting the front bulkhead, as it is illustrated in Figure 1.5. The method of impacting the 300 kg at 7 m/s can be done in several ways. [FSG, 2020] suggests a pendulum, drop tower, or a sled (as shown in Figure 1.5).

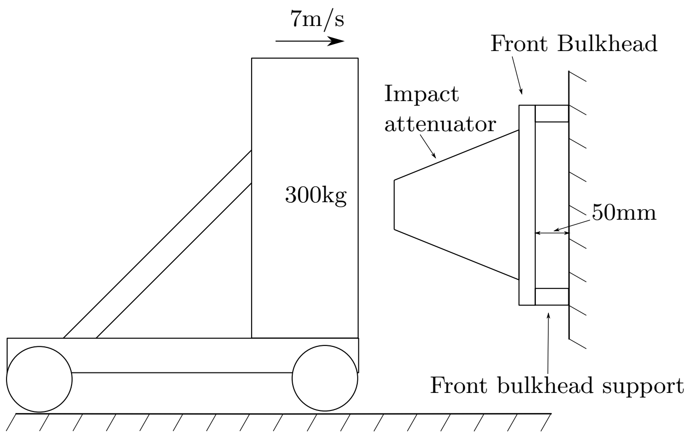

Figure 1.5: Typical test set-up for the impact attenuator verification.

1.3 Considerations

The energy absorption of the impact attenuator is equal to the area under the force-displacement curve, i.e.

$$W = \int P \, \mathrm{d}\delta \tag{1.5}$$

Ideally the energy absorption is equal to kinetic energy put into the system.

$$W = E_{kinetic} \tag{1.6}$$

To minimise the possibility of causing injuries to the driver, the ideal would be to have a constant load during the deformation of the impact attenuator i.e. a constant deceleration [Lu and Yu, 2003a]. The ideal force-displacement curve with the requirement from [FSG, 2020] implemented, is also shown on Figure 1.6. To avoid damage to the driver subsequent the collision, the impact attenuator should absorb the kinetic energy of the race car by an irreversible process such as plastic deformation, friction or fracture.

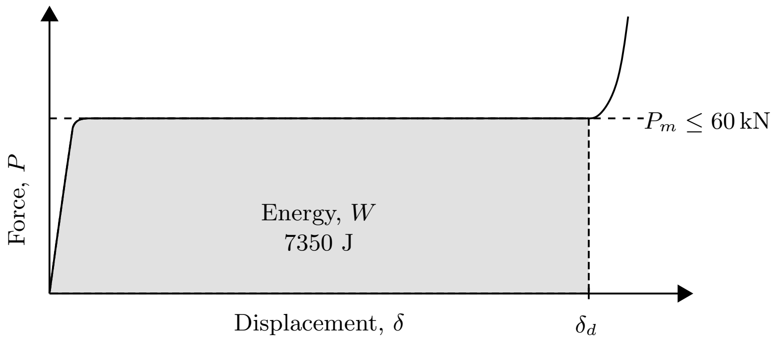

Figure 1.6: *Right*: Ideal force-displacement curve with [FSG, 2020] requirements implemented.

As the objective of the project is to minimise the mass of the impact attenuator assembly, a material, which can comply with the mechanical requirements as well as the geometric constraints, must be chosen.

Though, besides the mechanical properties, several other factors influence the choice of material. One factor, that always needs consideration in the design process, is the cost of the material and manufacturing. It is important to understand the costs associated with the production of the impact attenuator, as well as the trade-off between performance and cost. Furthermore, the chosen material has to be available on the market, such the design can be manufactured by AAU Racing. The fabrication of the impact attenuator should also be considered, such it is relatively simple to fabricate for the team members of AAU Racing. This is due to the competition rules [FSG, 2020], which states that

"Students should perform fabrication tasks where ever possible."

However, as the objective is to optimise the impact attenuator assembly, and only one impact attenuator is needed, the performance is prioritised over the cost.

2 — Material selection

Determining which material to use in the design of the impact attenuator, several factors need consideration, to ensure a good response of the impact attenuator in the event of an impact. These considerations include, mechanical properties, cost, manufacturing and the effect on the performance of the race car. These considerations are described in section 1.3. Based on these considerations, four materials are selected, and their advantages and disadvantages are analysed.

- Honeycombs
- Balsa wood
- Foams
- Fibre-reinforced polymers (FRP)

Based on this analysis a material is chosen, from which the impact attenuator is designed. To analyse the behaviour of the materials, quasi-static compression tests are conducted and presented as stress-strain curves in the following sections.

2.1 Metalic Honeycomb

A commonly used structure for crash absorbers, is metallic honeycombs. This is due to its possible extensive plastic deformation out-of-plane, as stated in [Gibson and Ashby, 1997] and [Magee and Thornton, 1978]. A minimum deformation of 70% can be achieved with commercially available honeycombs from [Plascore, 2020], when loaded perpendicular to the height of the honeycomb i.e. out of plane. [Bitzer, 1997] states that honeycombs:

> "*... has the highest crush strength-to-weight ratio of all energy absorption materials.*"

For these reasons, honeycomb structures are considered. In [Simonsen et al., 2019], experiments on hexagonal aluminium honeycombs were conducted, where the deformation mechanism and stress-strain curve are shown on Figure 2.1. The behaviour obtained is similar to the expected and seen in e.g. [Zhou et al., 2012] and [Wierzbicki, 1983]. As seen on Figure 2.1 the stress-strain curve is not as the ideal one described in section 1.3, because of the large difference between peak and mean stress. To avoid this, the honeycomb may be precrushed, as stated in [Bitzer, 1997], since this will eliminate the high peak stress. On Figure 2.2 a stress-strain curve is shown for the same aluminium honeycomb but precrushed. It is seen that the peak stress is eliminated, by precrushing the honeycomb 1.6 mm, which is suggested by [Bitzer, 1997]. The stresses are calculated based on the nominal area of the honeycomb, from Figure 2.3.

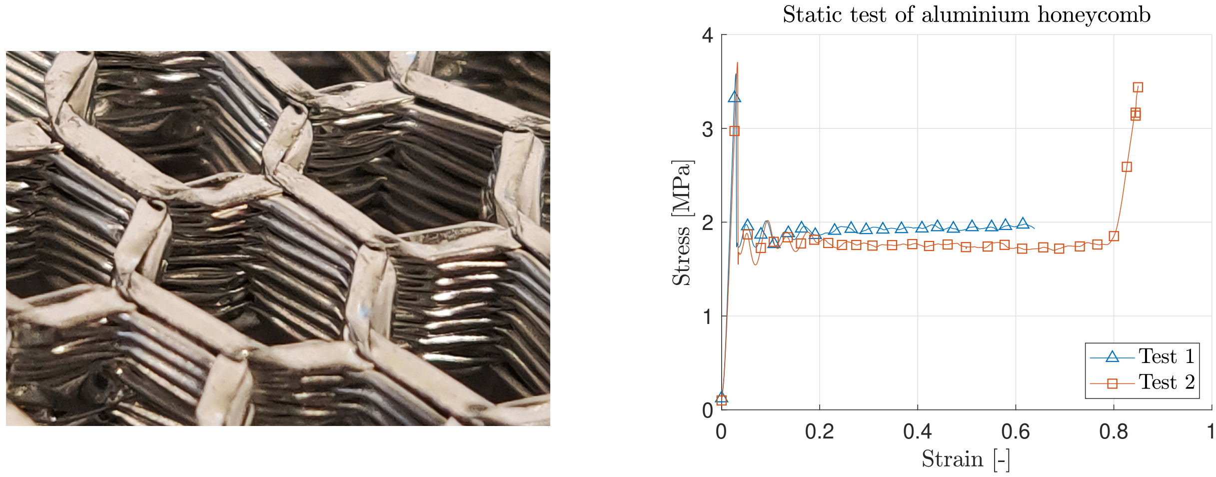

Figure 2.1: From previous project [Simonsen et al., 2019] *Left*: Deformation of hexagonal aluminium honeycomb. *Right*: Stress-strain curve of hexagonal honeycomb. As mentioned in the preface, the number of sample points between markers on graphs with multiple curves are given as $i\#$, here $i\# = 100$

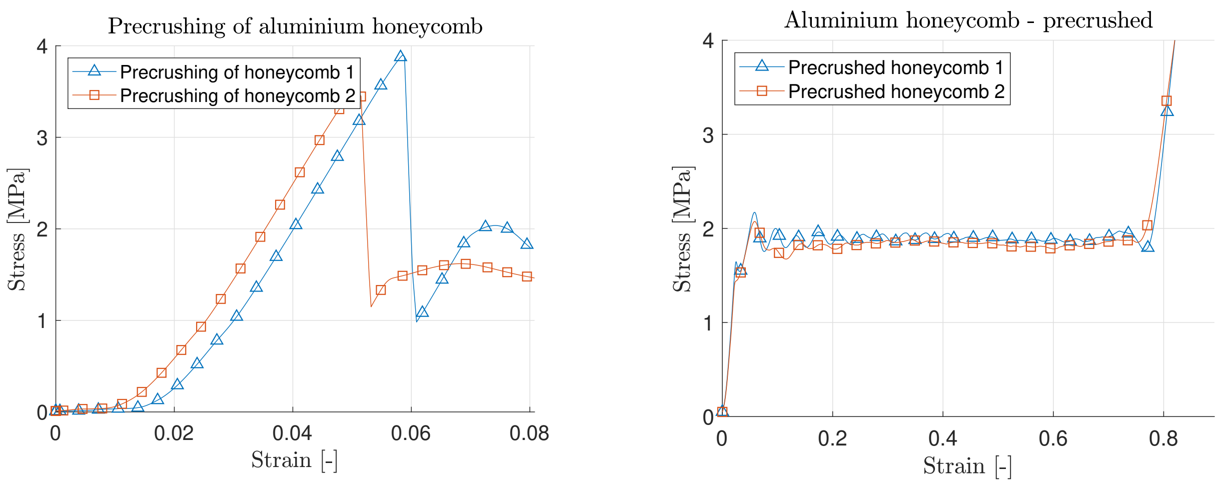

Figure 2.2: *Left*: Precrushning of aluminium honeycomb, unloaded at 1.6 mm. *Right*: Stress-strain curve for aluminium honeycomb after precrushing. For *left* $i\# = 10$ and for *right* $i\# = 100$.

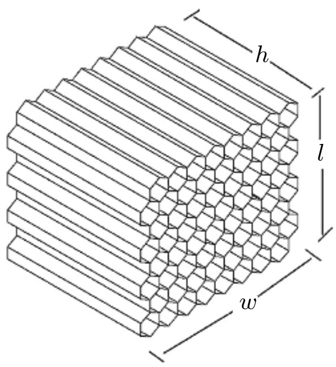

Figure 2.3: Outer dimensions of honeycomb. The nominal area used for calculating the stresses is $A = w\,l$ [Khan et al., 2011].

[Xu et al., 2012] has examined the influence of strain rate on hexagonal honeycombs in regards of mean stress and densification strain. It is shown that the mean stress and densification strain increases with increasing strain rates. The effect is larger with higher thickness to length ratio of the cell. The influence of strain rate is plotted on Figure 2.4.

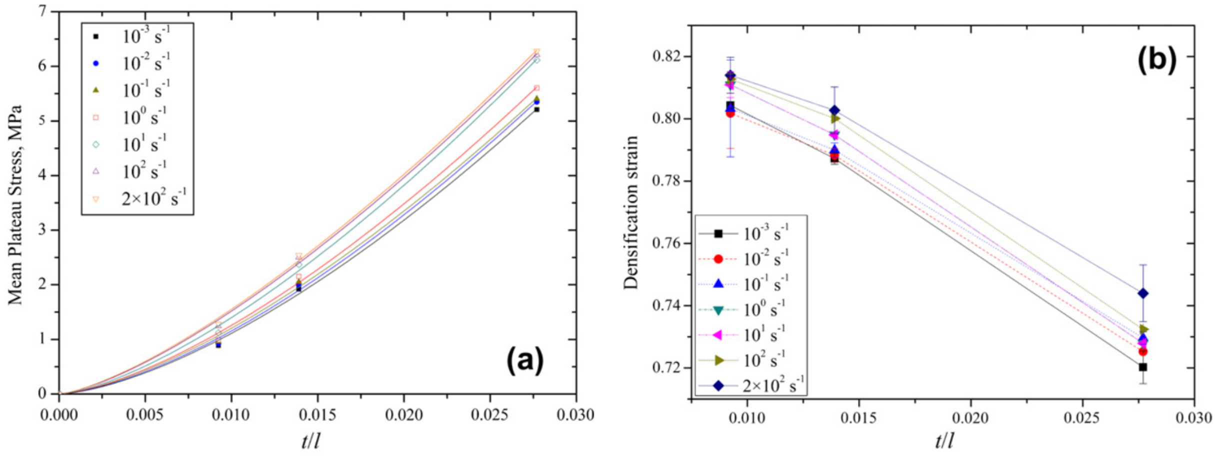

Figure 2.4: Strain rate influence on *left*: Mean stress *right*: Densification strain. Height of test samples are 50 mm. The tests are performed on an Instron 8800 high rate testing system, where the test specimens are glued on to the lower platen, which is moved towards the fixed upper platen. [Xu et al., 2012].

The material of the tested honeycomb is aluminium 5052, which is commonly used for metallic honeycombs, and the aluminium type used for the experiments shown on Figure 2.1 and 2.2. Dynamic tests are conducted as well, and the results from these are presented in section 3.2.

2.2 Cardboard honeycomb

In addition to the metallic honeycomb, experiments on cardboard honeycomb are conducted. The tested honeycomb is shown on Figure 2.5, together with the stress-strain curve.

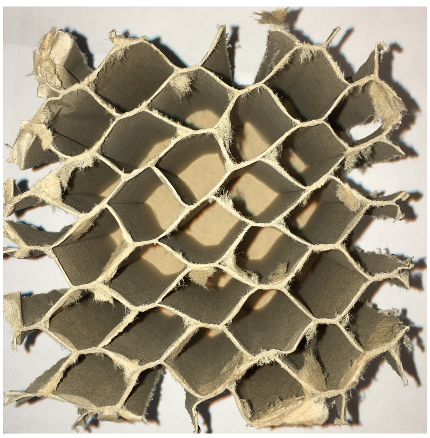

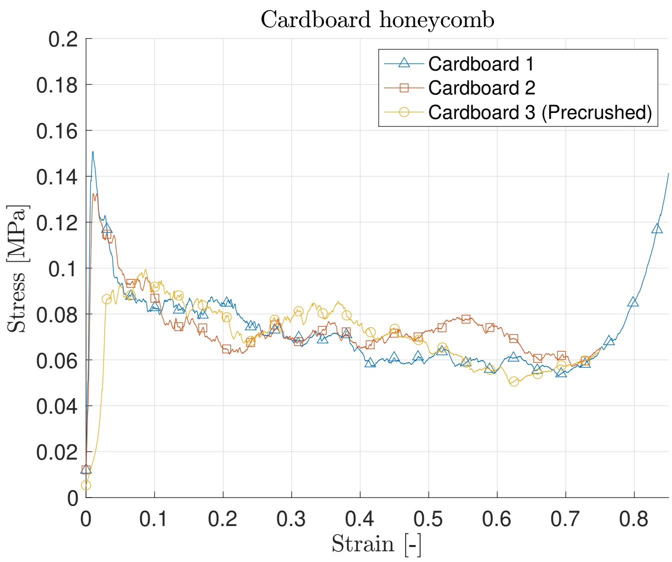

Figure 2.5: *Left*: Top view of tested cardboard honeycomb. *Right*: Stress-strain curve for cardboard honeycomb. $i\# = 400$.

The behaviour is similar to that of metallic honeycomb, expect the fact that the mean stress decreases along the displacement. The effect of precrushing is obvious, since the peak stress is eliminated. The tested honeycomb is stabilised by a thin layer of cardboard at the top and bottom which is glued to the honeycomb. The top layer is removed on Figure 2.5, but not for the experiments. As can be seen on Figure 2.5 the cells are dissimilar and the deformation of the cardboard is rather brittle compared to the metallic. This is seen on Figure 2.6, where the cardboard honeycomb tends to buckle globally and more random, than seen for the aluminium honeycombs.

Figure 2.6: Cardboard honeycomb after testing. The structure shows global buckling together with randomness in the buckling.

2.3 Balsa wood

Balsa wood shows good energy absorption properties, together with high strength and stiffness, why it is commonly used as core material in sandwich structures. The microstructure of balsa wood is similar to a honeycomb structure, as seen on the right of Figure 2.7. Figure 2.7 also shows the stress-strain curve for the tested balsa wood, which is alike that for a precrushed aluminium honeycomb. The stress-strain curves are made for balsa wood loaded axial and radial to the fibres. The difference in strength, relative to load direction, is observed on Figure 2.7.

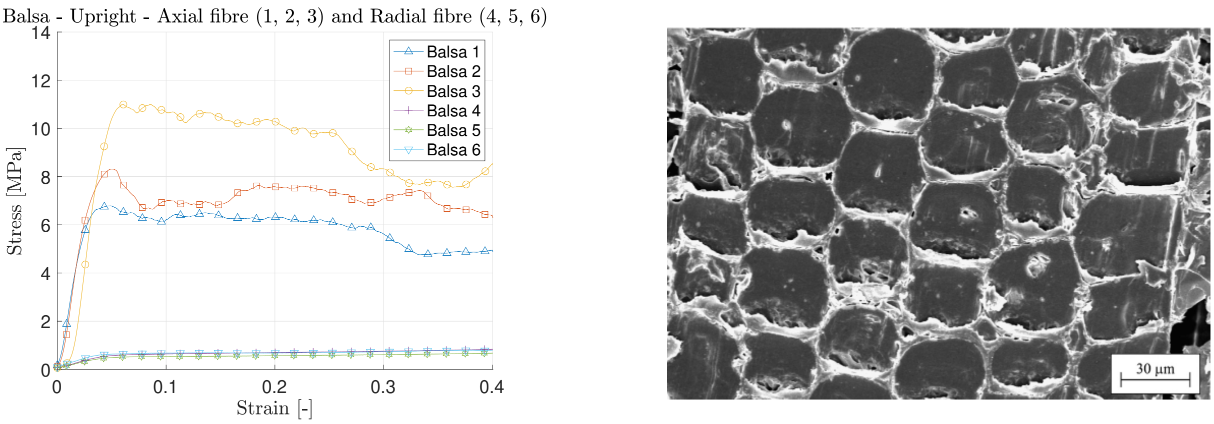

Figure 2.7: *Left*: Stress-strain curves for balsa wood. Balsa 1, 2 and 3 are loaded axial to the fibres while Balsa 4, 5 and 6 are loaded radial to the fibres. $i\# = 100$. *Right*: Micro structure of balsa wood [Silva and Kyriakides, 2007].

Even though balsa is stronger when loaded axially to the fibres, the mean stress when loaded radial is about 1/10 of the axial, which is significantly more than for honeycomb loaded in-plane found by [Khan et al., 2011]. Also, when loaded radial, balsa will not fracture, but show extensive plastic deformation.

Figure 2.7 shows a large deviation of the measurements of the axial loaded balsa wood. Since balsa wood is a natural material, the properties of the balsa samples might vary a bit, which can explain some of the deviation [Overgaard, 2014]. However, this should not have that large influence since the samples are from the same balsa board. The more likely explanation is due to the dimensions of the balsa samples. The samples are quite small in the crushing area, compared to the height, meaning they tend to fail/buckle, as seen on Figure 2.8. Due to the randomness of the failure/buckling, the curves show different results. Opposite aluminium honeycomb, where the energy absorption is governed by plastic deformation, balsa wood, when loaded axial, tends to fail, as seen on Figure 2.8.

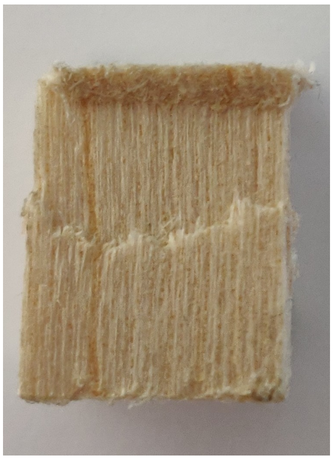

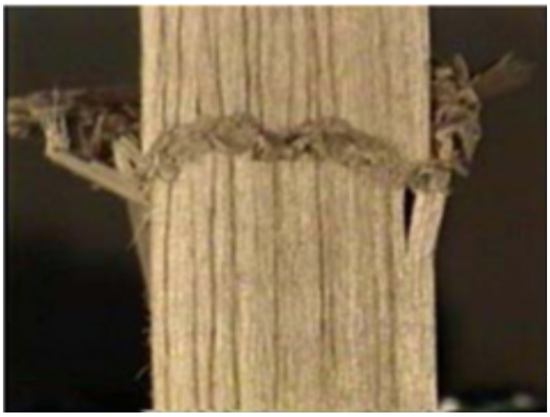

Figure 2.8: *Left*: Failure of tested balsa wood samples. *Right*: Failure of balsa under axial loading [Silva and Kyriakides, 2007].

The strain rate response of balsa wood has been investigated by [Tagarielli et al., 2007], who conclude that balsa wood is mildly sensitive to strain rate effects.

2.4 Foam

Foams are cellular materials that fills a three-dimensional space with cells and can be made from many different materials such as polymers, metals, and ceramics. The mechanical properties depend on the solid material from which the foam is made, the relative density, the shape of the cells and on the cell structure. Depending on these different parameters, a foam can have excellent properties for energy absorption, as shown on the right of Figure 2.9. On the left of Figure 2.9 it is seen, that the stress-strain curve has a linear elastic response followed by a stress plateau, initiated by plastic yielding until it reaches the densification strain. This behaviour is similar to that of a precrushed metallic honeycomb, where the peak stress and the mean load is relatively close. For elastic-plastic and brittle foams, the energy is dissipated by plastic deformation, fracture or friction. One of the main advantages of foams, compared to honeycombs, balsa wood and fibre-reinforced polymers, is that they can have isotropic material behaviour.

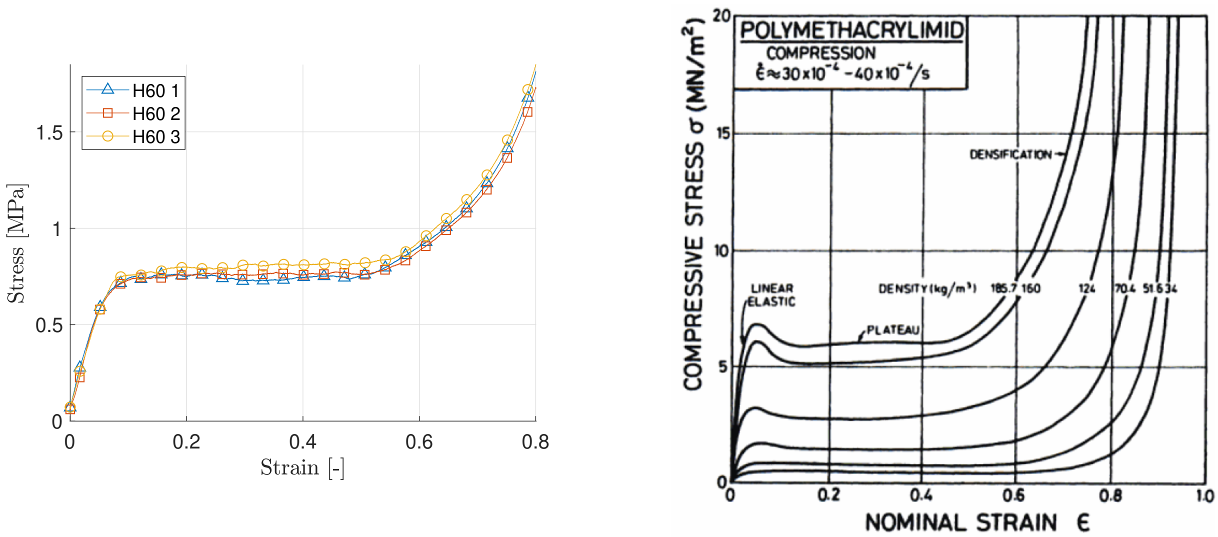

Figure 2.9: *Left*: Stress-strain curve for DIAB H60 foam. $i\# = 100$. *Right*: Stress-strain curves for polymethacrylimid. By increasing the relative density, Young's modulus and plateau is increased and decreases the densification strain [Gibson and Ashby, 1997].

2.4.1 Standard impact attenuator

The current impact attenuator, is a standard formula student model as mentioned in section 1.1. This impact attenuator is made in an Impaxx 700 foam, which is a closed-cell styrenic foam, that is developed specifically for energy absorption. This is seen in Figure 2.10, where the stress-strain curve for the Impaxx series 700, 500 and 300 are shown. From these stress-strain curves, it is seen that the Impaxx foam shows an almost ideal behaviour for an impact absorber, a constant stress plateau with a high densification strain of approximately 70∼75%. From Figure 2.10, it is also seen that the foam is slightly effected by the strain rate, however, the effect is small and negligible.

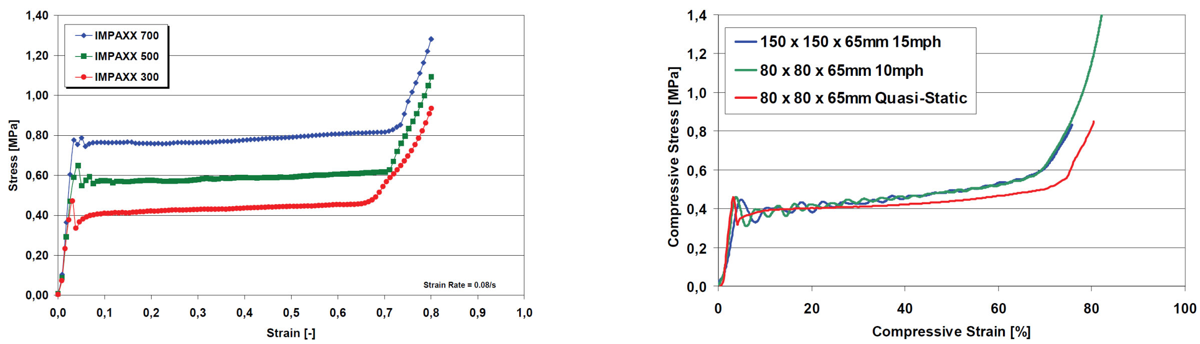

Figure 2.10: *Left*: Stress-strain curve for Impaxx 300, 500 and 700 foam. *Right*: Stress-strain curves for Impaxx foam with various impact velocities. [Slik et al., 2020].

2.5 Fibre-reinforced polymers

Fibre-reinforced polymers are widely used in lightweight structures due to their high specific stiffness, strength, and possibility of having directional properties. Furthermore, they can also be designed such they have high specific energy absorption, thus, fibre-reinforced composites are used in lightweight energy-absorbing structures e.g. the frontal crash structure of Formula 1 cars, see Figure 2.11, which are made of fibre-reinforced sandwich structures.

Figure 2.11: High speed image sequence of front impact crash test [Heimbs et al., 2009].

Energy-absorbing structures made with brittle fibre reinforced composites are designed to fail by fracture after an initial elastic response. In Figure 2.12, a typical force-displacement curve for progressive crushing of a composite tube is shown, along with a schematic representation of the deformation progress. As it is seen, the curve shows some of the characteristics of the ideal force-displacement curve, though, a profound peak force occurs.

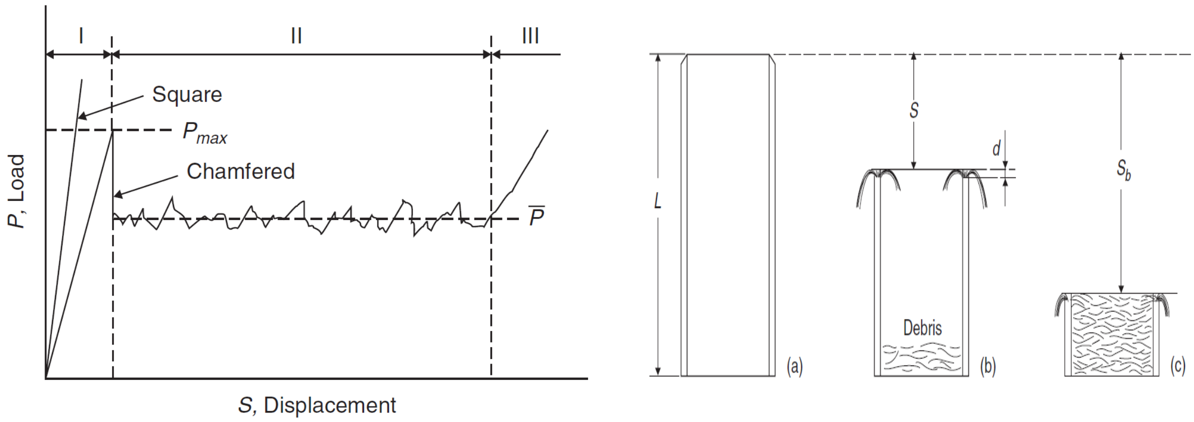

Figure 2.12: *Left*: Typical force-displacement curve for progressive crushing divided into three stages as aluminium honeycombs. *Right*: Deformation progress. [Lu and Yu, 2003b].

However as stated in [Hull, 1991], there are five variables affecting the energy absorption which cannot be treated independently:

- Microfracture processes at the crush zone
- Forces acting at the crush zone
- Microstructural variables associated with the composite material
- Shape and dimensions of the component
- Testing variables such as temperature and crush speed

Thus, making it difficult to design an impact attenuator in a composite material. Further, the amount laboratory work for manufacturing test samples for experimental verification is immensely increased.

2.6 Selecting material

With the possible materials described, the material for the impact attenuator can be determined. The tested materials are plotted on Figure 2.13, where the density and densification strain is plotted vs the mean stress.

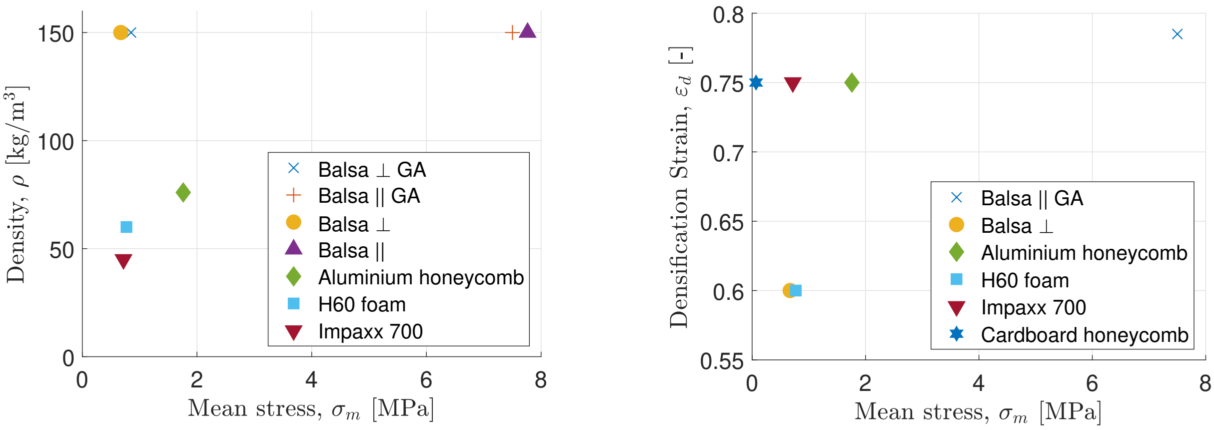

Figure 2.13: Comparison of the tested materials in regards of mean stress, density and densification strain. Values for balsa named GA are from [Gibson and Ashby, 1997]. *Left*: Density vs mean stress. *Right*: Densification Strain vs mean stress.

For further comparison, the energy absorption to density is calculated for the tested materials.

$$W_\rho = \frac{\text{Energy / Volume}}{\text{Density}} = \frac{\sigma_m \, \varepsilon_d}{\rho} \tag{2.1}$$

Where σ_m is the mean stress, ε_d the densification strain, and ρ the density. The results of equation 2.1 is given in Table 2.1. Here it is shown that aluminium honeycomb shows greater properties compared to the foams DIAB H60 and Impaxx 700. On the other hand, balsa wood is able of absorbing more than twice the energy as the aluminium honeycomb. But, due to the minimum dimensions of the impact attenuator, the balsa wood will result in a mean load of:

$$200\text{mm} \cdot 100\text{mm} \cdot 7.5\text{MPa} = 150\text{kN} \tag{2.2}$$

which is far above the allowable.

		Aluminium honeycomb	**Balsa || GA**	**DIAB H60**	**Impaxx 700**	**Cardboard honeycomb**
σ_m	[MPa]	1.76	7.50	0.77	0.70	0.07
ε_d	[−]	0.75	0.79	0.60	0.75	0.75
ρ	[kg/m^3]	76.00	150.00	60.00	45.00	21.25
W_ρ	[kJ/kg]	17.37	39.25	7.70	11.67	2.45

Table 2.1: Ratio between energy absorption and density for the tested materials.

As this is a project with a learning objective, fibre-reinforced polymers are discarded due to the immensely increased amount of laboratory work needed to verify a model. Balsa wood is discarded due to the high mean load achieved when using the minimum dimensions of the impact attenuator. Based on the poor energy absorption properties of cardboard honeycomb, as seen in Table 2.1, this is sorted out.

This leaves the remaining candidates; aluminium honeycombs and foams. An advantage of foams compared to the aluminium honeycomb is the possibility of isotropic behaviour of the structure. However, the requirement for the impact attenuator is defined for a frontal crash, thus, the advantages of possible isotropic behaviour of foam is irrelevant. Also, as it is seen in Table 2.1, aluminium honeycombs has better energy absorption than Impaxx 700. Further, the deformation behaviour of the aluminium honeycomb are closer related to the deformation behaviour, which is modelled in [Simonsen et al., 2019], which enables the project group to continue the work done in [Simonsen et al., 2019] in a more directly manner. Thus, it is chosen to design an aluminium honeycomb impact attenuator.

3 — Experiments

As a part of the design process, more experiments are conducted on aluminium honeycombs. This is done to study the strain rate dependency such a model can be developed on a better basis.

This chapter contains the description and results of the experiment conducted in this project. In [Simonsen et al., 2019] quasi-static experiments were performed on aluminium honeycombs. In appendix A, the quasi-static test set-up and results of the aluminium honeycombs from [Simonsen et al., 2019] are described. Thus, to study the strain rate dependency, the focus in this project is on dynamic testing.

The objective of this dynamic experiment is to see if the impact velocity, has a significant influence on the deformation and stress plateau of the aluminium honeycomb when comparing to quasi-static tests. These dynamic tests are performed with an impact velocity of approximately 7 m/s, since the formula student rules, requires that the impact attenuator is tested at an impact velocity of 7 m/s, as described in section 1.2.

3.1 Dynamic test

The dynamic experiments are initialised with a small number of tests, to check the set-up as well as the data processing. From the processed data, it is determined whether further tests are needed based on the agreement between the mean stress of the dynamic tests and the mean stress from the data sheet of the honeycomb used.

3.1.1 Experiment set-up

There are several ways to test the honeycomb structure subjected to impact loads. In this project, it is chosen to do a drop test, with the set-up shown on Figure 3.1, consisting of an impactor (a), a guide tube (b), a calibration scale (c), a high-speed-camera (d), an impact block (e), and a rubber mat (f). The maximum height from the steel block to the bottom of the honeycomb test sample is approximately 4 meters.

The test is performed by dropping an impactor from a certain height, such it reaches a velocity of approximately 7 m/s before impact. The honeycomb is attached to the impactor with a strip of double-sided tape, thus, ensuring the entire honeycomb is crushed at impact. A high-speed camera is used to record the deformation through a 250 mm gap between the guide tube and the impact block. Afterwards, the recording is analysed in the video analysis tool, Tracker.

The impact block is a 30 mm thick steel block, placed on a concrete floor, with a rubber mat placed in between, such the floor is not damaged. The rubber mat, impact block and impactor store some of the energy from the impact, however, the amount is assumed negligible compared to the energy absorption of the honeycomb. Therefore, during the analysis, it is assumed that the energy absorption is only from the honeycomb.

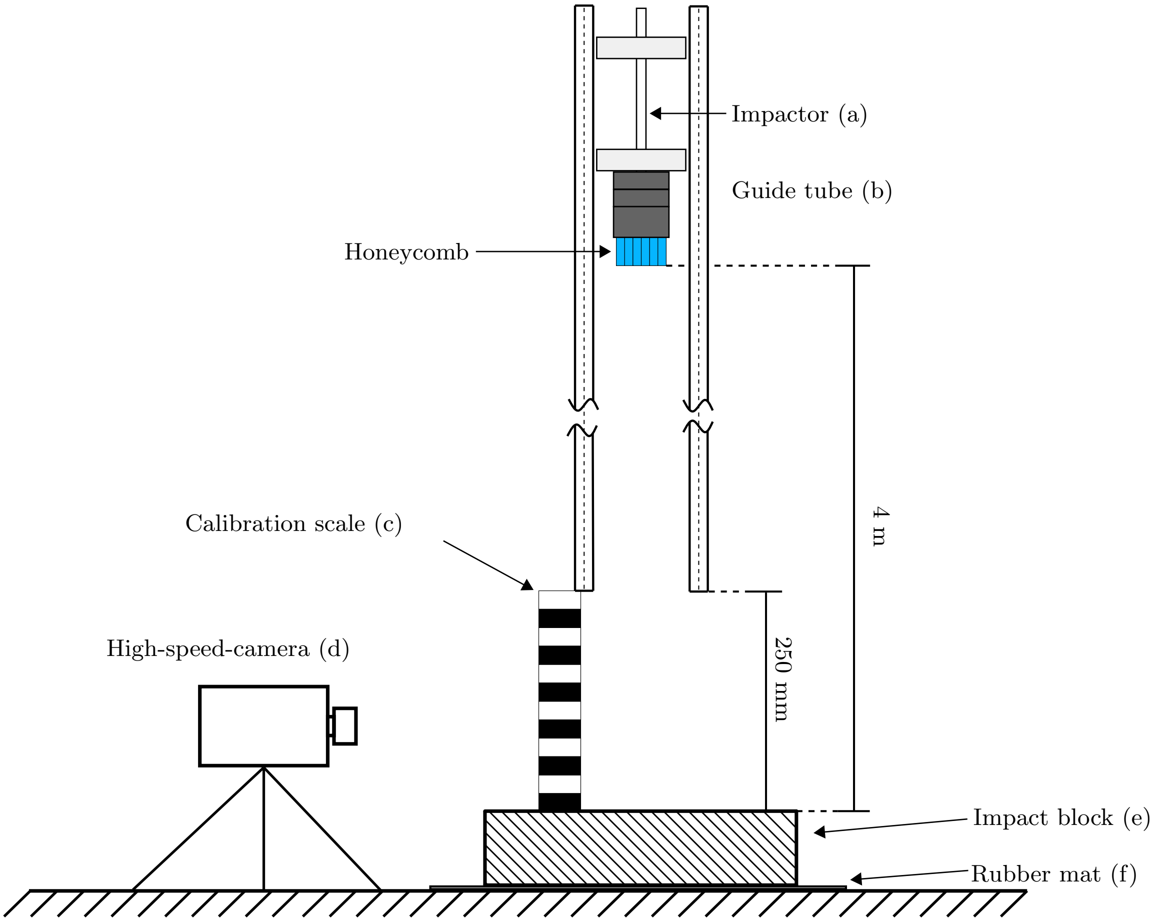

Figure 3.1: Test set-up of the dynamic experiments.

Honeycomb test samples

The honeycomb test samples used in these test, see Figure 3.2, are made of aluminium 5052 with a cell size of 3.2 mm and a wall thickness of 0.035 mm. This aluminium honeycomb has a peak stress of $\sigma_p = 3.72\,\text{MPa}$, a mean stress of $\sigma_m = 1.76\,\text{MPa}$ [Easycomposites], and the densification strain is found to be approximately $\varepsilon_d = 80\%$. The test samples have a height of 20 mm and a length and width of approximately $42.5\,\text{mm} \pm 2.5\,\text{mm}$, where the maximum dimension is determined by the impactor, as seen in Figure 3.3. The tolerance of $\pm 2.5\,\text{mm}$ gives a significant variation in the nominal area, which also affect the crushing force on the aluminium honeycombs. Therefore, it is expected to see a variety in the crushing force between 2.82 kN and 3.56 kN, in these initialising tests.

$$\begin{aligned}(40.0\,\text{mm} \cdot 40.0\,\text{mm}) \cdot 1.76\,\text{MPa} &\approx 2.82\,\text{kN} \\ (42.5\,\text{mm} \cdot 42.5\,\text{mm}) \cdot 1.76\,\text{MPa} &\approx 3.18\,\text{kN} \\ (45.0\,\text{mm} \cdot 45.0\,\text{mm}) \cdot 1.76\,\text{MPa} &\approx 3.56\,\text{kN}\end{aligned} \tag{3.1}$$

A factor, which needs consideration when determining the nominal area of the test samples, is the free cell walls illustrated with red in Figure 3.3. The free cell walls are those who do not complete a cell. Therefore, they do not require as much work to deform because of the free edges. Due to the small cell size of 3.2 mm and the relatively large tolerance of ±2.5 mm, in these initial tests, it is assumed to be an insignificant loss in energy absorption compared to the entire test sample. Furthermore, the purpose of these initial tests is to check the test set-up and data processing. Therefore a small difference in the nominal area does not effect the purpose of these tests.

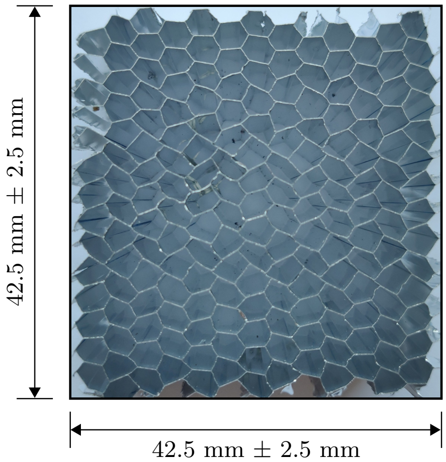

Figure 3.2: Nominal area, A, of honeycomb test sample used in the initial dynamic test, with given dimension.

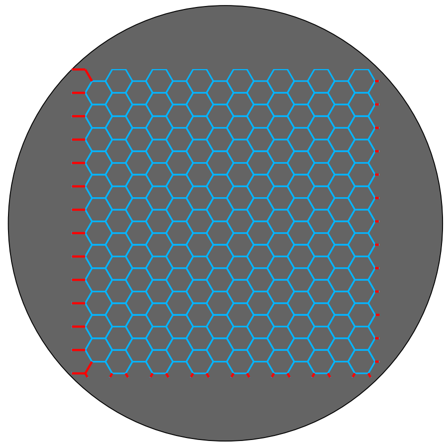

Figure 3.3: Honeycomb test sample (red and blue) attached to the impactor (grey). The red indicates the free cell walls.

Impact velocity and energy estimation

The impact velocity of the impactor is estimated by:

$$v_f^2 - v_i^2 = 2ad \tag{3.2}$$

Where v_f is the final velocity, v_i is the initial velocity, a is acceleration and d is distance travelled. In these tests, the impactor is dropped from rest, making the initial velocity zero and the acceleration $-9.82\mathrm{m/s^2}$ i.e. the gravitational acceleration. The maximum travel distance is four meters, as illustrated in Figure 3.1, giving an estimated impact velocity of -8.86 m/s, where effects such as drag and friction between the impactor and tube are neglected. The actual velocity and deceleration of the impactor are determined by analysing the image series in Tracker.

An estimation of the mass required to deform the test sample to densification needs to be determined. This is done by using the impact velocity, v, the densification strain, ε_d, the mean stress, σ_m, the height, h, and the nominal area, A. Firstly, the densification displacement is calculated:

$$\delta_d = \varepsilon_d\, h = 16\,\mathrm{mm} \tag{3.3}$$

Secondly, the work needed for the deformation is calculated

$$W = \sigma_m\, A\, \delta_d \approx 51\,\mathrm{J} \tag{3.4}$$

Thirdly, the work needed is equated the kinetic energy of the impactor, from which the mass can be found:

$$W = E = \frac{1}{2}mv^2 \Rightarrow m \approx 1.3\,\mathrm{kg} \tag{3.5}$$

It is decided to make the impactor have an interchangeable mass such different experiments can be conducted. This is done by making the impactor consist of a threaded rod at which steel blocks can be attached to add mass. At the end of the rod, a steel block with a blind hole is mounted, ensuring a planar surface. Thereby making it possible to vary the mass of the impactor between each test, see Figure 3.4. Furthermore, two blocks made in POM is mounted at the top and bottom to guide the impactor throughout the guide tube.

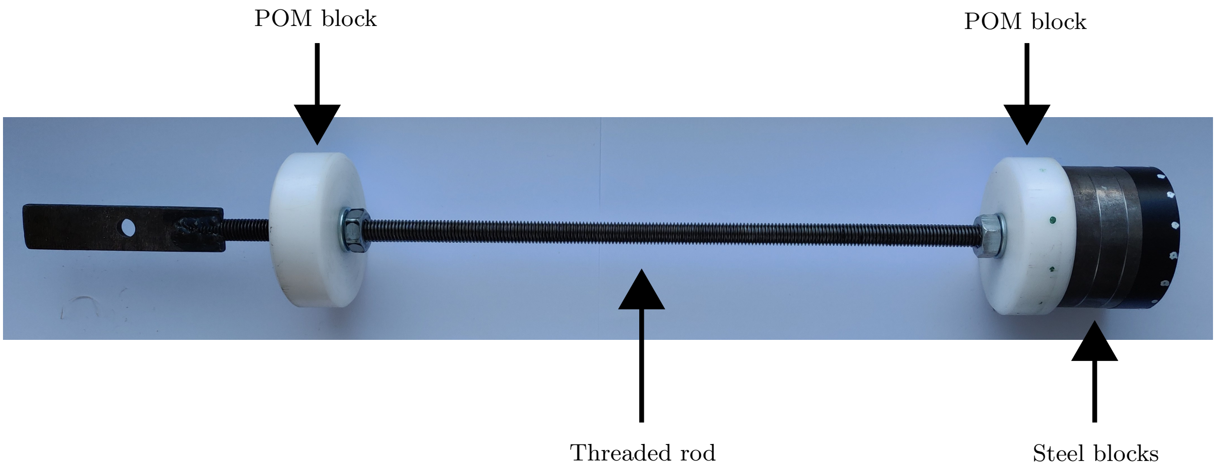

Figure 3.4: Impactor used in the drop test, consisting of a threaded rod, two guide blocks in POM, two weight blocks and the end block with a blind hole.

Thus, the impactor's mass is at minimum $m_{min} = 0.92\,\text{kg}$, including the rod, the POM blocks, the nuts and washers, and the end block. The mass of the weight blocks are approximately 0.22 kg, the masses are measured individually, and each block is numbered. With all the weight blocks, the impactor's mass is $m_{max} = 4.24\,\text{kg}$, which means the impactor can have a kinetic energy of

$$E = \frac{1}{2} m_{max}\, v^2 = 166.41\,\text{J} \tag{3.6}$$

3.1.2 Camera settings

To record the deformation of the honeycomb, which happens over a very limited time, the high-speed camera Photron FASTCAM SA5 model 775K-M1 is used. This camera can take 5,400 fps with a resolution of 1,024 × 1,024 pixels, where higher frame rates reduce the resolution. For these initial tests, 5,400, 10,000 and 20,000 fps videos are recorded, to find what is necessary. The resolution at 10,000 fps and 20,000 fps is 768×640 pixels and 640×368 pixels, respectively.

At these high frame rates, it is necessary to consider the required increase in exposure. As the number of frames per second increases, the amount of light needed to achieve the same exposure also increases. In addition to the frame rate, adjustment of the shutter speed and the aperture also affects the lighting. The shutter speed determines the length of time that the lens is exposed to light, and the aperture determines how much light passes through the lens, i.e. faster shutter speed gives a more instantaneous picture, and smaller aperture gives better in depth focus. The effect of the shutter speed and aperture is illustrated in Figure 3.5, along with the required light.

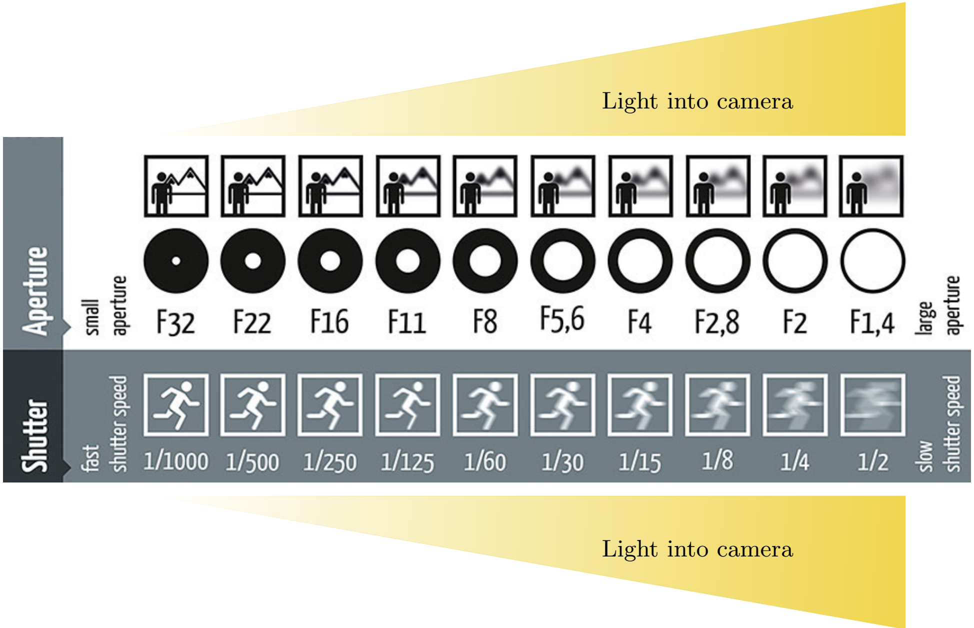

Figure 3.5: Influence of shutter speed and aperture on the picture quality. Modified from [deMilked, 2015].

From the figure, it is seen that fast shutter speed and a small aperture comes with the consequence of less light into the camera. Since it is desired to observe the deformation it is important to have an instantaneous picture rather than a smeared picture — fast shutter speed is needed. Since the calibration zone, honeycomb, and the impactor are rather flat and approximately the same distance from the camera, good in depth focus is not need — large aperture can be used. For these tests, the shutter speed is either 1/20,000 s or 1/25,000 s, since these are the fastest where enough light is accessible to distinguish between the background and the calibration zone clearly, with the chosen frame rate. With these considerations, an effort is put in to lighten the test set-up, from all angles, as seen in Figure 3.6.

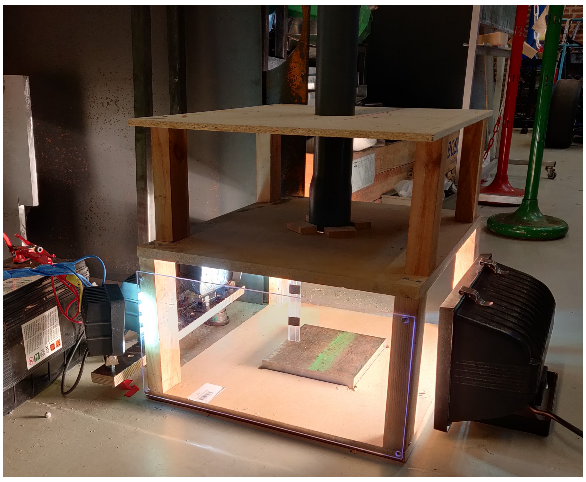

Figure 3.6: Picture of the light set-up for the dynamic experiments.

The reason for increasing the frame rate and shutter speed is to investigate whether it is possible to capture the peak load with this test set-up. In addition to capturing the peak load, the frame rate should be high enough to get reliable and usable data.

3.2 Data treatment

As described in section 3.1, to deform the honeycomb test sample 80%, with an impact speed of -8.86 m/s, a mass of 1.30 kg is required. This mass does not directly comply with one of the variable masses of the impactor. Therefore the nearest achievable mass is chosen, which is 1.36 kg.

Seven initial tests are carried out, three at 5,400 fps and two tests at 10,000 fps and 20,000 fps. By visual inspection of the test samples after the tests, it is seen that the deformation of the aluminium honeycomb is dominated by folding mechanisms, see Figure 3.7. This deformation behaviour is the same as seen from the quasi-static test performed in [Simonsen et al., 2019] and in section 2.1 of the precrushed honeycombs. However, some of the test samples do not have a uniform deformation, as seen in Figure 3.7, which leads to different position measurement of the targets in the video analysis of a test sample. Therefore, the mean value of the tracked targets position is taken as the deformation of the honeycombs.

Figure 3.7: *Left:* Folding mechanisms of honeycomb. *Right:* Non-uniform deformation of one of the test samples.

These tests are analysed in Tracker, where the position data is collected and used to determine the velocity and acceleration using a Central Difference scheme, more details about the data treatment in Tracker can be found in appendix B. As a consequence of using numerical differentiation of the position, the data, especially for acceleration, is scattered. The derived velocity and acceleration, from the position data of one tracked target in a 5,400 fps test and a 20,000 fps test, is seen in Figure 3.9 - 3.10.

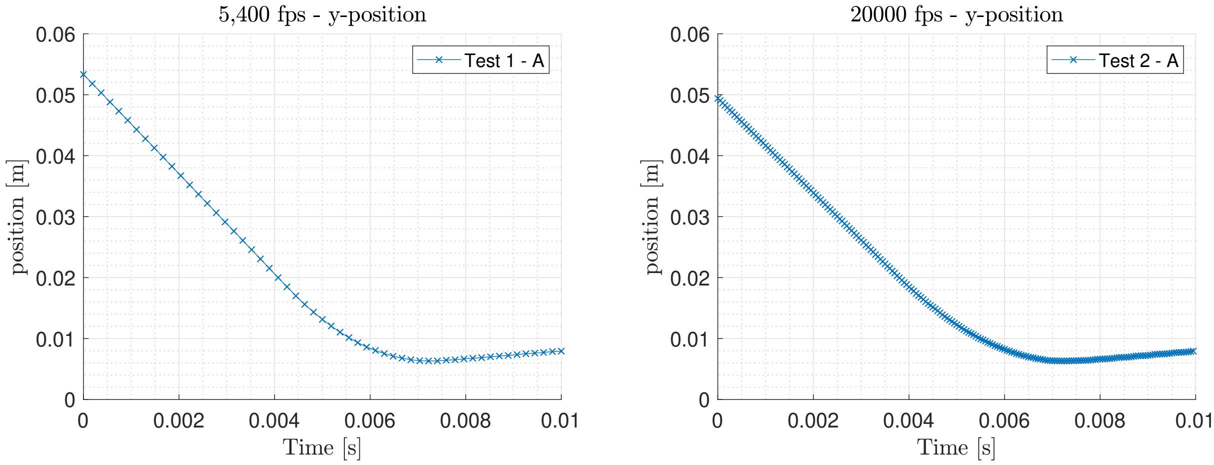

Figure 3.8: Comparison between the y-position of a tracked target for test 1 at 5,400 fps and a tracked target for test 1 at 20,000 fps.

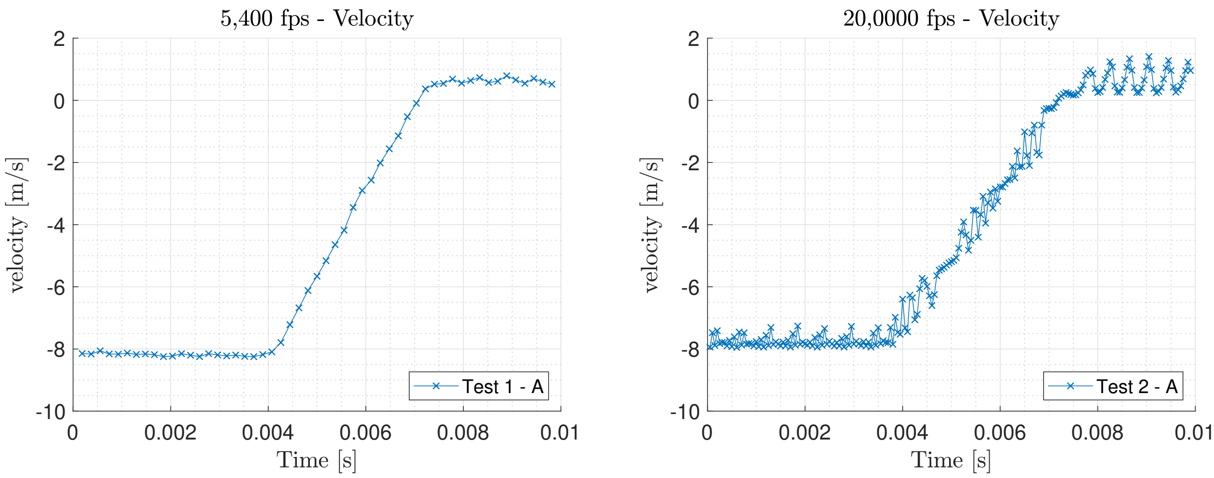

Figure 3.9: Comparison between the y-velocity of a tracked target for test 1 at 5,400 fps and a tracked target for test 1 at 20,000 fps.

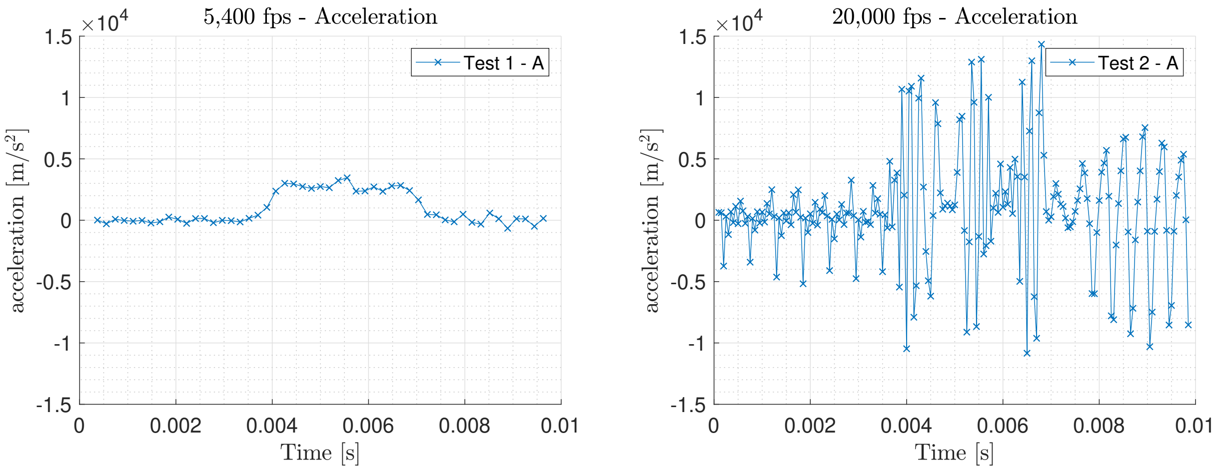

Figure 3.10: Comparison between the y-acceleration of a tracked target for test 1 at 5,400 fps and a tracked target for test 1 at 20,000 fps.

From these figures, it is seen how a relative smooth position measurement, can have fluctuations when using numerical differentiation to obtain velocity and acceleration. One reason for these fluctuations is the consistency of selecting the exact pixel at which the target is located. If the selected target is off by a couple of pixels, fluctuations in the velocity and acceleration will occur. Due to the resolution of the camera, the free cell walls, and small cell size of the honeycomb, it is not possible to visually confirm from the videos, whether the fluctuations occur due to tracking errors or a physical response of the aluminium honeycomb. However, for the same amplitude in fluctuation on the position more data points will generate larger amplitudes in fluctuations due to the numerical differentiation. This is probably the reason for the large fluctuation when using 20,000 fps.

In Figure 3.11, a close-up of the honeycomb test sample, from test 2 at 20,000 fps, during impact is seen, where the deformation begins at the bottom of the honeycomb. From analysing the videos, it is seen that it is arbitrary whether the deformation of the honeycomb starts in the top or the bottom. However, other than visually confirm the impact point and the beginning of the deformation, it is not possible to correlate peaks and valleys of the velocity curve with the initialisation of a new fold in the honeycomb.

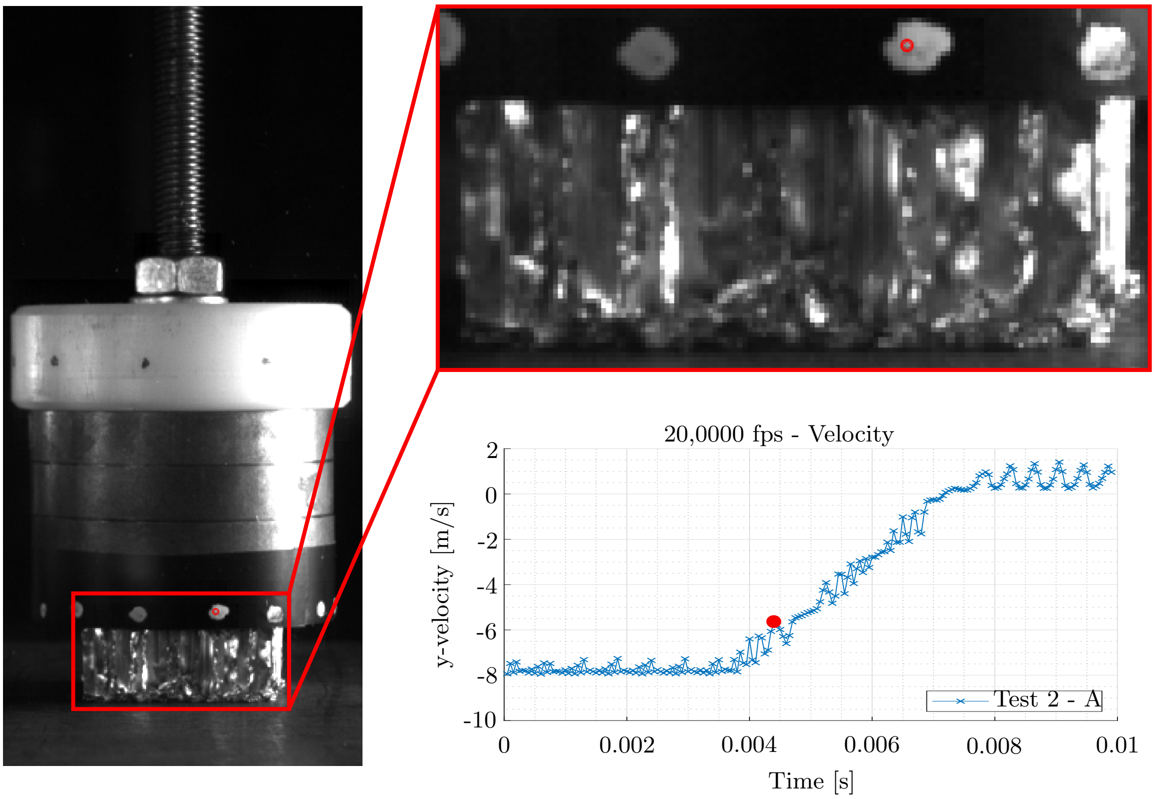

Figure 3.11: Close-up of the honeycomb test sample during impact, with the marked sample point (red) on the velocity curve.

With these results and observations, it is concluded that the derived accelerations cannot be used to determine the peak load of the honeycombs. A study of how to enable the capture of the peak load is conducted. As it is seen from the quasi static experiments in section 2.1 it is seen that the peak occur at a strain of approximately $\varepsilon_p = 0.05$, i.e. the displacement at the peak is

$$\delta_p = \varepsilon_p \, h = 1\,\text{mm} \tag{3.7}$$

Assuming the impact velocity is constant during the elastic straining, with the velocity,

$v = 8.86\,\text{m/s}$, the duration from impact to peak will be

$$t_p = \frac{\delta_p}{v} = 1.25\text{E-}6\,\text{s} \tag{3.8}$$

In the quasi static experiments 150 data points are used from impact to the mean load. Thus, assuming the same amount of data points is needed, frame rate needed would be:

$$FPS = \frac{150}{t_p} = 1.2\text{E}6\,\text{s}^{-1} \tag{3.9}$$

There is a few reasons why this probably will not work. Firstly, the camera, used in this set-up, cannot achieve a frame rate of $1.2\text{E}6\,\text{s}^{-1}$. Secondly, the numerical differentiation of all this data points will surely return false fluctuations. However, since the peak load of precrushed aluminium honeycombs is assumed to be insignificant, as for the static tests, described in section 2.1. It is also determined that further investigation on the peak load is unnecessary because the impact attenuator is designed with precrushed honeycombs.

Besides the peak load, it is still possible to determine the impact velocity, absorbed energy and the mean load of the honeycombs from the video analysis, based on the mean acceleration and deformation. First, the test data is divided into three zones, the free-fall zone, the impact zone and the rebound zone see Figure 3.12, by analysing the video and the velocity curves.

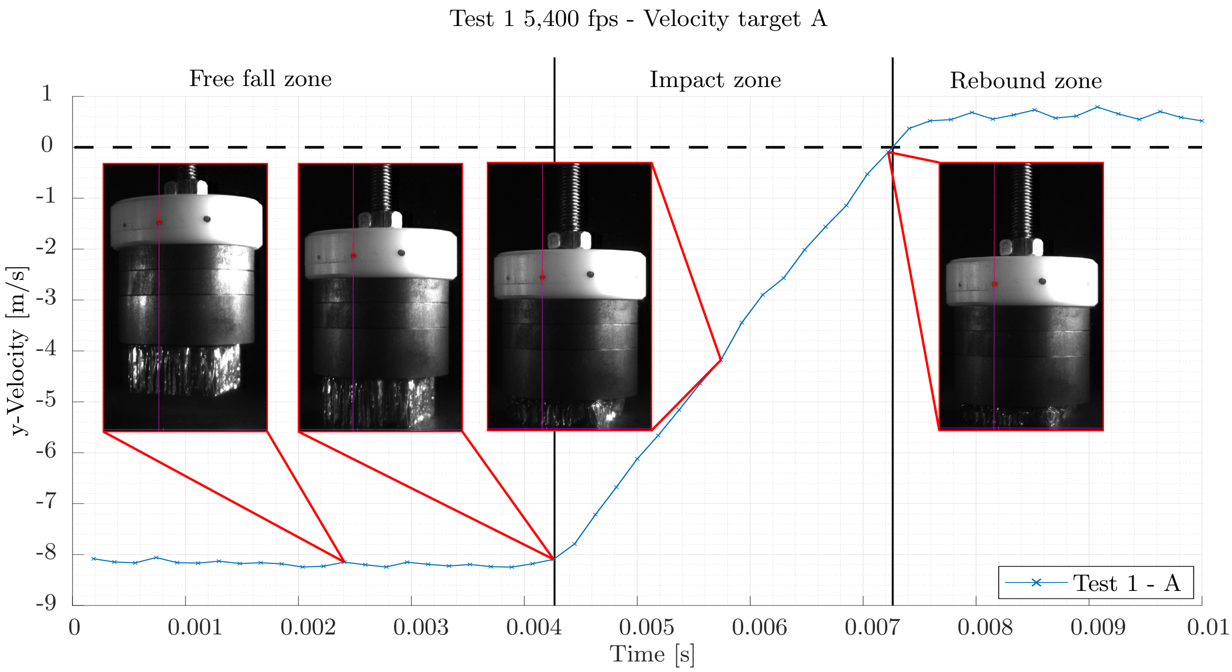

Figure 3.12: Velocity of the tracked target A for the first test conducted at 5,400 fps, divided into three zones, the free fall zone, impact zone and the rebound zone, where images corresponding to the data points are inserted for visualisation, with the tracked object marked with a red dot and the y-axis of the coordinate system is purple.

With this division, the point of impact is established, from which the impact velocity is determined. The impact velocities of each test are given in Table 3.1. From Table 3.1, it is seen that the impact velocities vary between -7.75 m/s and -8.40 m/s, which is lower than the estimated velocity, properly caused by friction between the guide tube and the impactor, drag, and a variation in drop height. This variation in impact velocity affects the kinetic energy of the impactor and thereby the deformation. The rebound is thought to mainly be caused by the elastic energy stored in the impactor during impact where it is seen that the rebound zone of the tests made with 20,000 fps, shows a periodic response of the tracked object. One explanation for this response could be that it is the eigenfrequency of the impactor that is captured at 20,0000 fps but not captured with 5,400 fps or 10,000 fps. However, since the main objective of this experiment is to verify how a dynamic impact affects the mean stress of the honeycomb, only the impact zone is of importance — the rebound response is of no interest in this experiment.

To analyse the impact zone, first, the average velocity of each test is determined based on the derived velocities of the tracked targets. With the averaged velocity, linear regression is made between the data points in the impact zone, see Figure 3.13. The linear regressions of each test are evaluated using the coefficient of determination R^2. As seen in Table 3.1, the lowest value of the coefficient of determination is 0.9745, which expectedly is from the test conducted with 20,000 fps. Based on the R^2 values, it is determined that all the linear fits appropriately describes the velocity response of the impactor during impact. By differentiation of the linear regression, the mean acceleration of the tests is obtained, see Table 3.1. With the known acceleration and mass of the impactor, the mean load is calculated using Newton's second law of motion.

$$F = a\,m = P_m \tag{3.10}$$

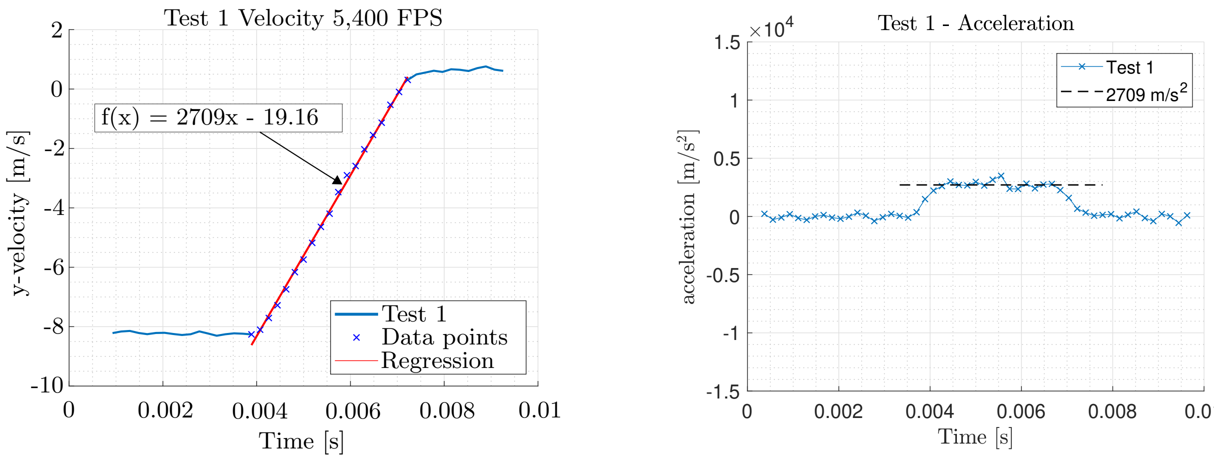

Figure 3.13: *Left:* Averaged velocity of test 1 at 5,400 fps, with the linear regression and marked data points used in the regression. *Right:* Acceleration derived from the averaged velocity, where the mean acceleration during impact, derived from the regression, is implemented.

Frame rate [fps]	**Test** [-]	$\mathbf{v_{impact}}$ [m/s]	$\mathbf{R^2}$ [-]	$\mathbf{a_{mean}}$ [m/s^2]	$\mathbf{P_m}$ [kN]	ε_d [%]	**Energy** [J]
5,400	1	-8.26	0.9979	2709	3.68	68.70	50.59
	2	-8.12	0.9985	2718	3.69	69.84	51.60
	3	-7.99	0.9988	2296	3.12	78.66	49.09
10,000	1	-8.40	0.9985	2310	3.14	72.72	45.66
	2	-8.25	0.9987	2280	3.10	80.05	49.61
20,000	1	-7.98	0.9745	2332	3.17	67.38	42.71
	2	-7.82	0.9832	2169	2.95	75.26	44.37

Table 3.1: Results and data obtained from the analysis of the seven tests.

From Table 3.1, it is seen that besides test 1 and 2 at 5,400 fps, the test samples are within the expected interval (2,816 N - 3,564 N) from equation 3.1. Test 1 and 2 at 5,400 fps, is 3.9% and 4.3% above the expected maximum mean load, respectively. One explanation for this increase in the mean load is that the nominal area of these two test samples is larger than the given maximum dimensions — 45 mm × 45 mm. Another explanation is that the mean stress of the honeycomb could be higher than that provided by the data sheet (1.76 MPa). From the quasi-static tests in section 2.1, it is seen that the mean stresses of the precrushed aluminium honeycomb are 1.89 MPa and 1.82 MPa, where the quasi-static tests in Appendix A have mean stresses of 1.91 MPa and 1.76 MPa. This indicates that the mean stress of each sample is varying, which could be caused by the number of free cell walls and how perfect the cells are. Therefore it is inconclusive from these initial test, how large an effect the impact load has on the mean stress of the aluminium honeycomb. However, considering the varying mean stress in the quasi-static test and possibly larger area, an increase of 4.3% in the mean load is not significant.

Besides the mean load applied to the honeycomb, the strain of each test is also determined, see Figure 3.14 and Table 3.1. From this, it is seen that the densification strain varies between 67.38% - 80.05%, where the quasi static experiments shows approximately 80%.

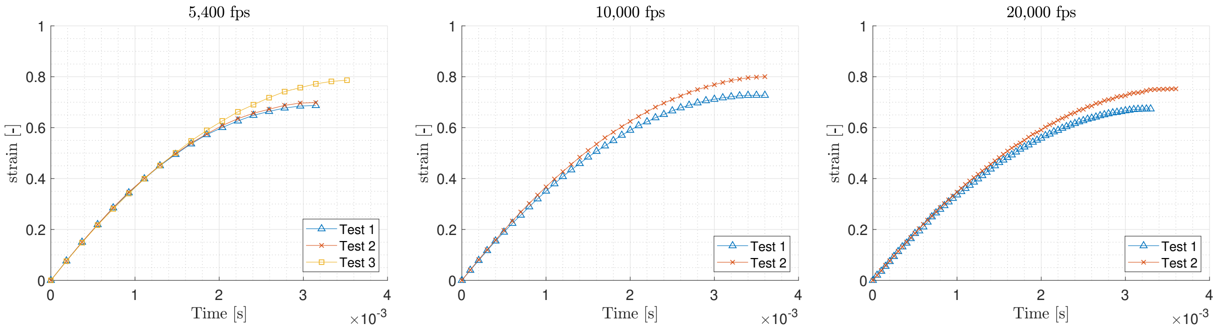

Figure 3.14: Strain-time curve for: *Left*: 5,400 fps. *Middle*: 10,000 fps *Right:* 20,000 fps.

Since the purpose of these tests is to check the test set-up and data processing, it is concluded that the test set-up and data processing is a viable solution to obtaining the mean load during impact loading. Based on the regression fit of the velocity during the impact the results are satisfying.

Further testing with varying impact velocity, mass of the impactor, nominal area and height of the honeycombs is wanted to be done. Especially it is desired to perform tests of honeycomb samples, with precise and known nominal areas, such it is possible to determine a mean stress of each sample and compare it to the mean stress of the data sheet. However, due to COVID-19 and the lockdown, further testing is not possible. Therefore, based on the knowledge gained in section 2.1 and these seven tests, it is concluded that dynamic impact loads up to -8.40 m/s, does not have a significant effect on the aluminium honeycombs and therefore can be neglected.

3.2.1 Summary

From these tests it is concluded that there is no reason to use more than 5,400 fps, to determine the mean load applied to the honeycomb, with the current test set-up. This is due to the uncertainties of tracking the markers on the impactor in Tracker, where more data points lead to large fluctuations when numerical derivation is used to derive the velocity and acceleration. In addition to that did the tests captured with 5,400 fps, show great agreement with the expected energy absorption. Based on these fluctuations it is concluded that, with the current test set-up, it is impossible to determine the peak load of the honeycomb. With these tests, it is also concluded that impact velocities up to 8.40 m/s has a negligible effect on the mean load.

As mentioned at the beginning of the chapter, the conducted tests are intended as initial tests, where the experience is applied to new tests. Unfortunately, due to the current circumstances, further testing is not a possibility. Fortunately, the results are better than nothing and applicable.

4 — Model

In this chapter, a FEM model able to simulate the deformation and mean stress of aluminium honeycombs is developed in LS-DYNA. The purpose of the model is to have a basis from which an optimised design of the impact attenuator can be obtained. Therefore, it is necessary to simulate the deformation behaviour and mean load of the aluminium honeycombs accurately why a study of the boundary conditions and contact formulations in LS-DYNA is made. This model is a continuation of the model developed in [Simonsen et al., 2019]. Therefore a basis regarding the use of the commercial code LS-DYNA and explicit time integration in finite element analyses is obtained before this project and summarised in section 4.1.

4.1 Summary of chapter 3 in [Simonsen et al., 2019]

In chapter 3 of [Simonsen et al., 2019] the development of a FEM model able to simulate the deformation and mean stress of an aluminium square tube is described. Since the deformation behaviour of the aluminium square tube is based on folding mechanisms similar to the honeycomb, it is an excellent basis for modelling the deformation of the aluminium honeycomb. In the development of the model in [Simonsen et al., 2019], it was found that the commercial code LS-DYNA is suitable for solving highly non-linear problems by using explicit time integration. Due to the non-linearities of this problem; geometric non-linearity, i.e. large deformation occurs, material non-linearity, i.e. plasticity in this case, and the non-linearity of contacts, both contact between an impactor and the honeycomb model as well as the self-contact of the honeycomb cell walls during deformation, it is decided to continue using LS-DYNA in this project as well.

4.1.1 Explicit time integration

LS-DYNA uses explicit time integration which excels in dealing with non-linearities. This is because, in the explicit time integration, the equation of motion is solved for nodal acceleration in each iteration.

$$[M]\{a\} + [D]\{v\} + [K]\{x\} = \{F\} \Rightarrow \{a\} = [M]^{-1}(\{F\} - [D]\{v\} - [K]\{x\}) \tag{4.1}$$

Where $[M]$ is the lumped mass matrix, $\{a\}$ nodal accelerations, $[D]$ the damping matrix, $\{v\}$ nodal velocities, $[K]$ the stiffness matrix, $\{x\}$ nodal displacements, and $\{F\}$ nodal forces. The explicit time integration excels because the system of equations is decoupled. This is due to $[M]$ is a diagonal matrix, which means that $[M]^{-1}$ is trivial:

$$[M] = \begin{bmatrix} m_1 & & & 0 \\ & m_2 & & \\ & & \ddots & \\ 0 & & & m_n \end{bmatrix} \Rightarrow [M]^{-1} = \begin{bmatrix} \frac{1}{m_1} & & & 0 \\ & \frac{1}{m_2} & & \\ & & \ddots & \\ 0 & & & \frac{1}{m_n} \end{bmatrix} \tag{4.2}$$

Thereby no time is spent on factorisation. From the acceleration, the velocities are calculated with the time-step, and the displacements are calculated from the velocities. The entire process is illustrated in Figure 4.1.

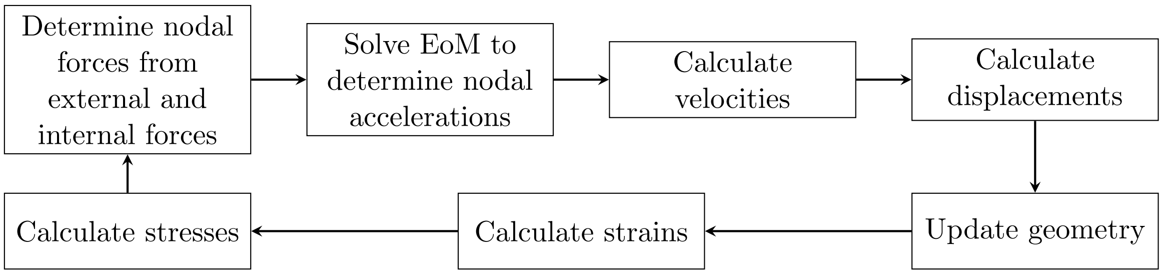

Figure 4.1: Explicit time integration work flow. EoM is short for equation of motion.

The time-step size, Δt, is limited by the highest eigenfrequency of the system, ω_{max}, to ensure numerical stability.

$$\Delta t \leq \frac{2}{\omega_{max}} \tag{4.3}$$

Though the maximum time-step size is typically approximated using the Courant condition:

$$\Delta t \leq \frac{L_{e,min}}{c}, \qquad \text{where} \qquad c = \sqrt{\frac{E\,(1-\nu)}{(1+\nu)\,(1-2\nu)\,\rho}} \tag{4.4}$$

Where $L_{e,min}$ is the smallest element length in the system, E Young's modulus, ν Poisson's ratio, and ρ the density.

4.1.2 Elements

In [Simonsen et al., 2019], the Belytschko-Tsay shell element formulation is used to model the aluminium square tube. This decision was based on a trade-off between computational time and accuracy of the model. Therefore a study regarding the element length, L_e, and thickness of a plate, t, was conducted on the Belytschko-Tsay shell element formulation. From the study, it was found that for:

$$\frac{L_e}{t} = 2.5 \tag{4.5}$$

An error of approximately 10% compared to an analytical model is to be expected. Despite the error of 10%, the shell element formulation was chosen compared to solid elements, where it was concluded that the model appropriately simulated the deformation and mean load of the aluminium square tube. However, due to the dimensions of the square tube, the element size was relatively large, and refinement resulted in errors. Therefore, it was discussed whether solid elements should be used.

2D cellular structures typically have a plate-like structure out-of-plane, i.e. small wall thickness compared to the other dimensions. The critical time step size would be significantly reduced if solid elements are to be used compared to shell elements since stresses can propagate through the thickness of the element Further, bending is part of the deformation, thus, according to

[Endelt, 2018] and [ANSYS, 2015], three to four elements are needed through the thickness, the reduced element length is illustrated in Figure 4.2.

For example, if the honeycomb used in the experiments is to be modelled, the smallest element length would be:

$$L_e = \frac{0.035\text{mm}}{3} \approx 0.012\text{mm} \tag{4.6}$$

Which for a typical aluminium $\left(E = 70\,\text{GPa},\ \nu = 0.33\,rho = 2.8\,\text{ton/m}^3\right)$ would give a critical time step of

$$\Delta t = 1.92\text{E-9}\,\text{s} \tag{4.7}$$

Similarly for shell elements, with

$$L_e/t = 2.5 \tag{4.8}$$

the critical time step is:

$$L_e = 0.0875\,\text{mm} \Rightarrow \Delta t = 14.38\text{E-9}\,\text{s} \tag{4.9}$$

Which is

$$\frac{14.38\text{E-9}\,\text{s}}{1.97\text{E-9}\,\text{s}} = 7.5 \tag{4.10}$$

times larger for the shell element, i.e. the simulation with the solids would need 7.5 times as many iterations in a simulation. Furthermore, three times as many elements would be needed if the solid elements have the same element length on the other directions as the shells. Which would cause the solid elements to have a aspect ratio of 7.5 as well, which is tending to be too large, i.e. more elements would be needed, and for every time one extra element is added in the cell wall plane another two is added in the thickness. Thus, the amount of elements can rather quickly become enormous.

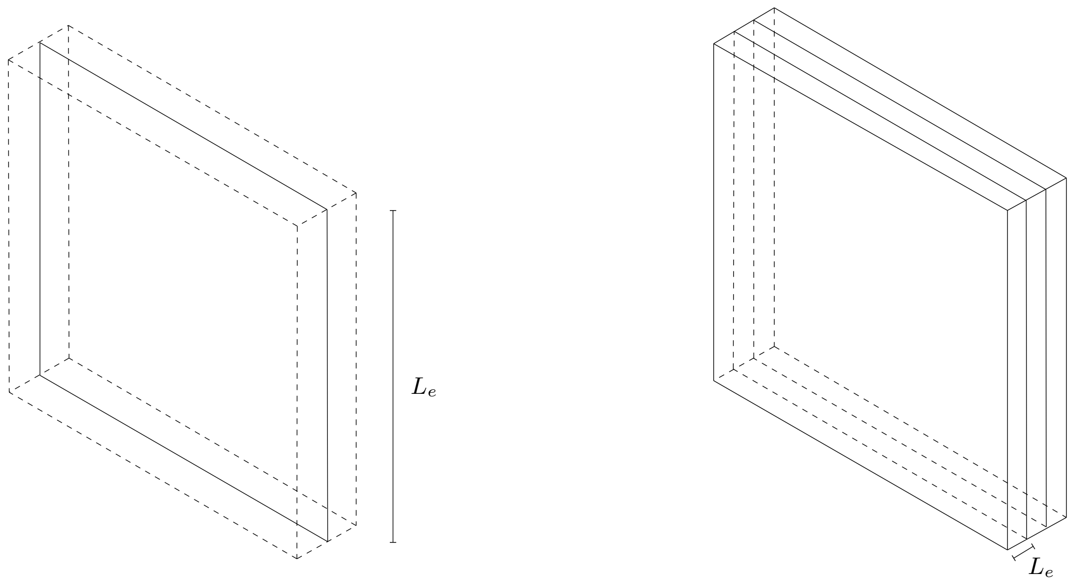

Figure 4.2: Illustration of shortest element length, L_e, in shells and solids. *Left:* Shell element. Dashed lines represent the volume that the shell element represents. *Right:* Solid elements represent the same volume as the shell to the left. Three elements are added through the thickness.

Thus, it is decided to continue using the Belytschko-Tsay shell element formulation in the modelling of the honeycomb.

4.1.3 Material model

In [Simonsen et al., 2019], *MAT_POWER_LAW___PLASTICITY, also called Material Type 18 in LS-DYNA was used to model the deformation of an aluminium square tube, which is an isotropic plasticity model with rate effects which uses a power-law hardening rule. Since the model simulated quasi-static loading, strain rate effects were not considered. In this project, an impact loading is simulated. However, as described in section 3.2, the strain rate effect on a aluminium honeycomb is found to be insignificant for rates at the level needed in this project. Therefore, Material Type 18 is also used in this project, while strain rate effects are considered negligible.

The power-law hardening rule in LS-DYNA uses Hooke's law until an yield strain criterion is reached after which a power-law is used:

$$\sigma = \begin{cases} E\varepsilon & \text{for } \varepsilon < \varepsilon_y \\ k\varepsilon^n & \text{for } \varepsilon \geq \varepsilon_y \end{cases} \tag{4.11}$$

Where σ is the stress, E is the Young's modulus, ε is the strain, ε_y is the yield strain, k is the strength coefficient, and n is the strain hardening exponent. The yield strain is determined by:

$$\varepsilon_y = \left(\frac{E}{k}\right)^{\left(\frac{1}{n-1}\right)} \tag{4.12}$$

In [Simonsen et al., 2019], the material parameters used in the power-law model were based on [Varmint Al, 2019], who provides material models for different aluminium alloys. [Varmint Al, 2019]'s "5052-o sheet" material model will be used for developing the model.

4.1.4 Model controls

In [Simonsen et al., 2019] it was investigated how much mass scaling could be applied to increase the time-step size and thereby decrease the computational time. In [Simonsen et al., 2019], quasi-static loading, i.e. low-velocity impact is considered, why scaling the mass should not change the response of the system significantly. However, as the velocity is increased, inertia forces become a larger part of the system response, i.e. scaling the mass while increasing the impact velocity can be problematic. Therefore, it needs to be determined how much mass scaling to apply to the simulation of the honeycomb.

Furthermore, a study of the through-thickness integration method and the number of integration points through-thickness were also made. In this study, it was found that the Lobatto Quadrature method with nine integration points through the thickness was suitable to model the aluminium square tube. The Lobatto Quadrature places an integration point on both outer surfaces of the shell, and one integration point is placed on the mid-surface as well when an uneven number of integration points is used. Nine points were chosen because this is the maximum uneven number of integration points which can be chosen for Lobatto Quadrature. Whenever more than ten points are chosen, LS-DYNA uses a trapezoidal rule, which is not recommended due to accuracy problems. Based on this, it is chosen to use the same method, with the same amount of integration points through the thickness.

4.1.5 Summery

Based on the knowledge obtained from the previous project, it is decided to model the aluminium honeycomb in LS-DYNA with explicit time integration. The shell elements cannot have a length to thickness ratio smaller than 2.5, while a nine-point Lobatto Quadrature rule is used in the integration points through the thickness and material model 18 in LS-DYNA is used without strain rate effect. The problem ought to be suited for mass scaling. However, in the initial models, no mass scaling is applied in the simulation.

4.2 Preliminary consideration

Some considerations are done before setting up the model. Firstly, the behaviour of the stress-strain curve for an aluminium honeycomb is considered. Secondly, the manufacturing method is considered. Finally, the deformation modes due to the manufacturing method are analysed, such it can be incorporated in the model.

4.2.1 Expected behaviour of stress-strain curve

As described in section 2.1 and seen in Figure 4.3, the stress-strain curve for an aluminium honeycomb is initiated by a large peak load, followed by a load plateau, i.e. the mean load, and ultimately densifies. Since the stress stabilises around a mean stress, there is no need to simulate the entire deformation of the honeycomb to obtain the mean stress of the model. Thereby the computational time is reduced due to the smaller model and termination time. However, by only simulating a small part of the deformation, it is not possible to determine the densification strain. Therefore it is decided only to model a 10 mm high honeycomb, from which representative stresses can be computed. Furthermore, due to the manufacturing method and idealisation of the honeycomb, the honeycomb model can be simplified, which reduces the computational time further.

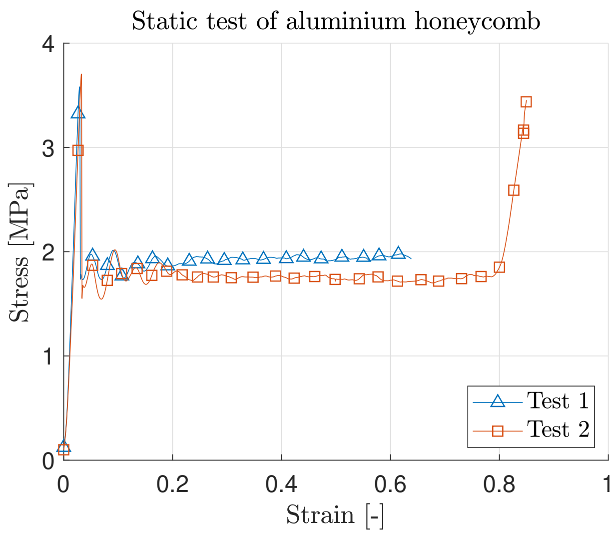

Figure 4.3: Stress-strain curve for aluminium honeycomb repeated from Figure 2.1.

4.2.2 Manufacturing

The manufacturing of commercially available honeycombs is typically done using adhesive bonds, where [Bitzer, 1997] estimates that 95% of honeycombs are manufactured using adhesive bonds. [Bitzer, 1997] introduces two methods of manufacturing honeycombs from sheet material with adhesive bonding: The expansion process and the corrugation process. [Bitzer, 1997] states that:

"Almost all of the adhesive-bonded cores are made by the more efficient expansion process."
[Bitzer, 1997]

The honeycomb used in the quasi-static tests and the dynamic tests were manufactured with the expansion process. Thus, only the expansion process is considered. The process is illustrated in Figure 4.4.

1. Foil material on a roll
2. Adhesive lines are printed and the foil is cut into sheets
3. The sheets are stacked into the HOBE (Honeycomb before expansion) block
4. The HOBE block are cut into HOBE slices with a desired thickness
5. Expand the HOBE slice to a honeycomb panel
6. Final product

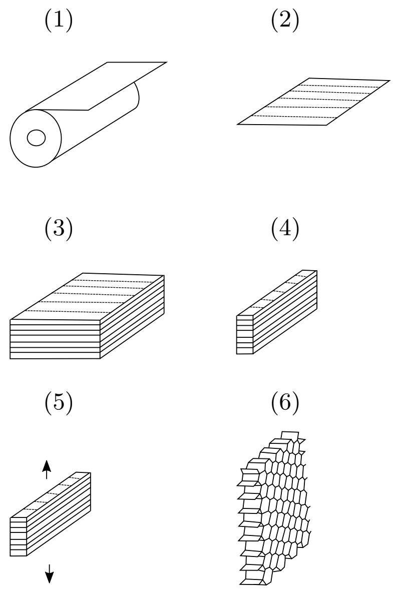

Figure 4.4: Honeycomb manufacturing using the expansion process. Edited from [Bitzer, 1997].

Due to the adhesive bond between the sheets, some sides in the honeycomb have two walls and a layer of adhesive, illustrated in Figure 4.5. Therefore it is investigated whether it is necessary to take the adhesive bond into account and how to handle this in a simulation.

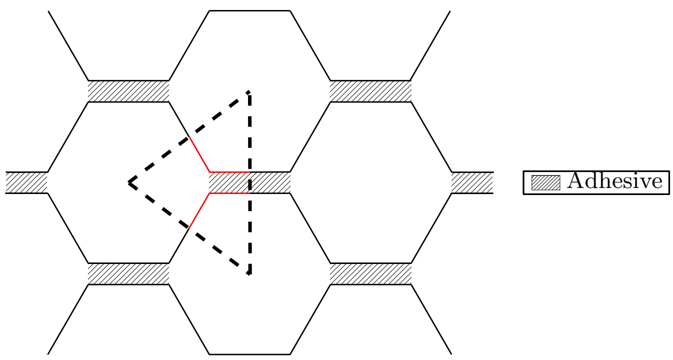

Figure 4.5: Adhesive layer between cells walls. Thickness of adhesive layers is exaggerated. Based on the symmetry of the honeycomb structure, it can be made of "Y" sections, marked with red in the dashed triangle.

4.2.3 Deformation modes

[Wierzbicki, 1983] has investigated the deformation mechanisms of metallic honeycombs where the adhesive bond is taken into account. Due to the symmetry of the hexagonal honeycomb, it is only needed to consider one "Y" section, see Figure 4.5, which has a height equal to that of a local buckling wave, i.e. one fold. Based on this "Y" section, also called a joint, it is distinguished between a firm joint (e.g. a welded joint) and a bonded joint, where a firm joint deforms as illustrated on the left of Figure 4.6 and a bonded joint deforms as on the right of Figure 4.6. The deformation of the firm joint requires considerable in-plane deformations, whereas for the bonded joint, the two plates are partially torn off and thus requires less work to deform. The reasoning in [Wierzbicki, 1983]'s analysis is based on the strength of the adhesive bond which is smaller than the strength of the metallic cells, i.e. it requires less work to break the bond than to plastically deform the metallic cells.

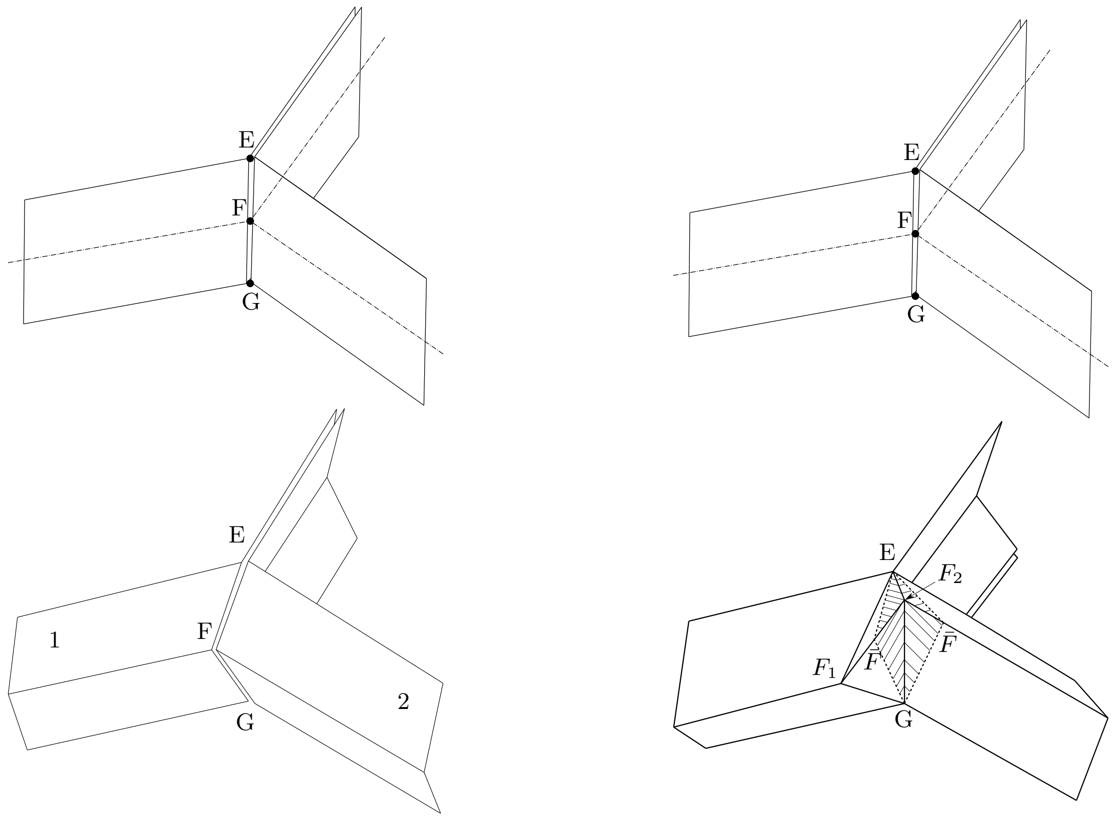

Figure 4.6: Joint, marked with dashed triangle on Figure 4.5, before and after deformation. *Left:* Firm joint where the cell walls remains coincident at points E, G, and F. *Right:* Bonded joint where the cell walls remains coincident at points E and G. However at point F the cell walls splits such F becomes F_1 and F_2. The marked areas constructed with $\bar{F}$ are four identical triangles which represents the area where the adhesive bond is broken. Modified from [Wierzbicki, 1983].

[Wierzbicki, 1983] finds good correlation between his theory of breakage of the adhesive bond and experiments. Since the deformation mechanism is dependent on the adhesive bond, which is used in commercial honeycombs, a solution to this should be developed.

4.3 Model set-up

For the model set-up, the boundary conditions and the eccentricity is discussed. Further, LS-DYNA and LS-PrePost are introduced.

4.3.1 Boundary conditions

As seen from Figure 4.5, the model can be simplified to a single joint, i.e. a "Y" section, based on the symmetry of the honeycomb structure. This simplification reduces the number of elements needed to model the structure and thereby minimises the computational time. The "Y" section, is modelled between two rigid bodies, where one rigid body is fixed, acting as the ground, while the other moves at a constant velocity, acting as the impactor, see Figure 4.7.

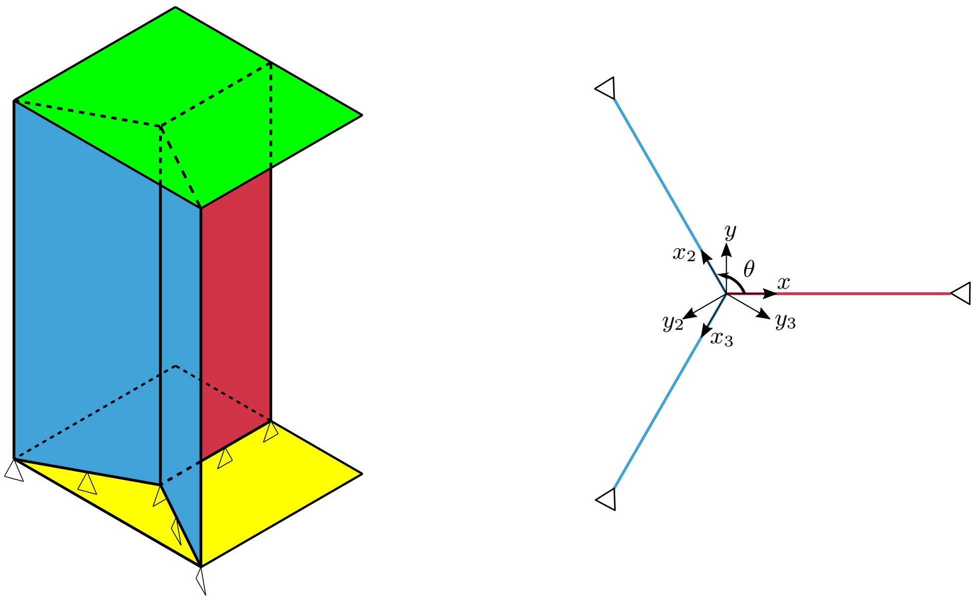

Figure 4.7: Joint with boundary conditions. $x - y$ is the global Cartesian coordinate system, $x_2 - y_2$, and $x_3 - y_3$ are two local coordinate systems rotated by θ and 2θ, respectively. θ is the angle between the cell walls. As the honeycomb is constructed of regular hexagons $\theta = 120°$.

The boundary conditions for the model are split into two categories; the first category is the more general one where all nodes on the bottom of joint are constraint in all translational directions, the second category is the symmetry conditions. The symmetry conditions are applied to the end of each wall which is facing away from the joint centre, as seen on Figure 4.7.

The symmetry conditions are applied to simulate adjacent cell walls, i.e. the conditions must be such the walls cannot expand or contract along their length and only rotate around their length direction. E.g. the wall which lies along the x-axis in the global Cartesian coordinates, as seen in Figure 4.7, are constraint from translation in the x-direction and rotation around y-axis and z-axis. However, the boundary conditions for the other two walls cannot be applied in the global Cartesian coordinates, as the walls are not parallel to either of the axes. Thus, two local Cartesian coordinate systems are introduced by rotating the global coordinate system.

4.3.2 Eccentricity

The eccentricity would typically be applied as a force on the top nodes to deflect the system a bit. However, the symmetry conditions make it troublesome to apply an eccentricity as they constrain the honeycomb to deform as a bending beam. The eccentricity can also be applied as variations in material parameters. However, this feature is only implemented in a few material models in LS-DYNA, and not in the power-law plasticity model. Though, the necessity of the eccentricity is questionable, as plastic buckling is induced without an applied eccentricity. This can happen because LS-DYNA is not perfect, it makes rounding errors, and as stress waves bounces back and forth these rounding errors will result in an imperfect simulation, which will conveniently trigger a buckling mode. Thus, no eccentricity is applied in the model.

4.3.3 Model structure in MATLAB, LS-PrePost, and LS-DYNA

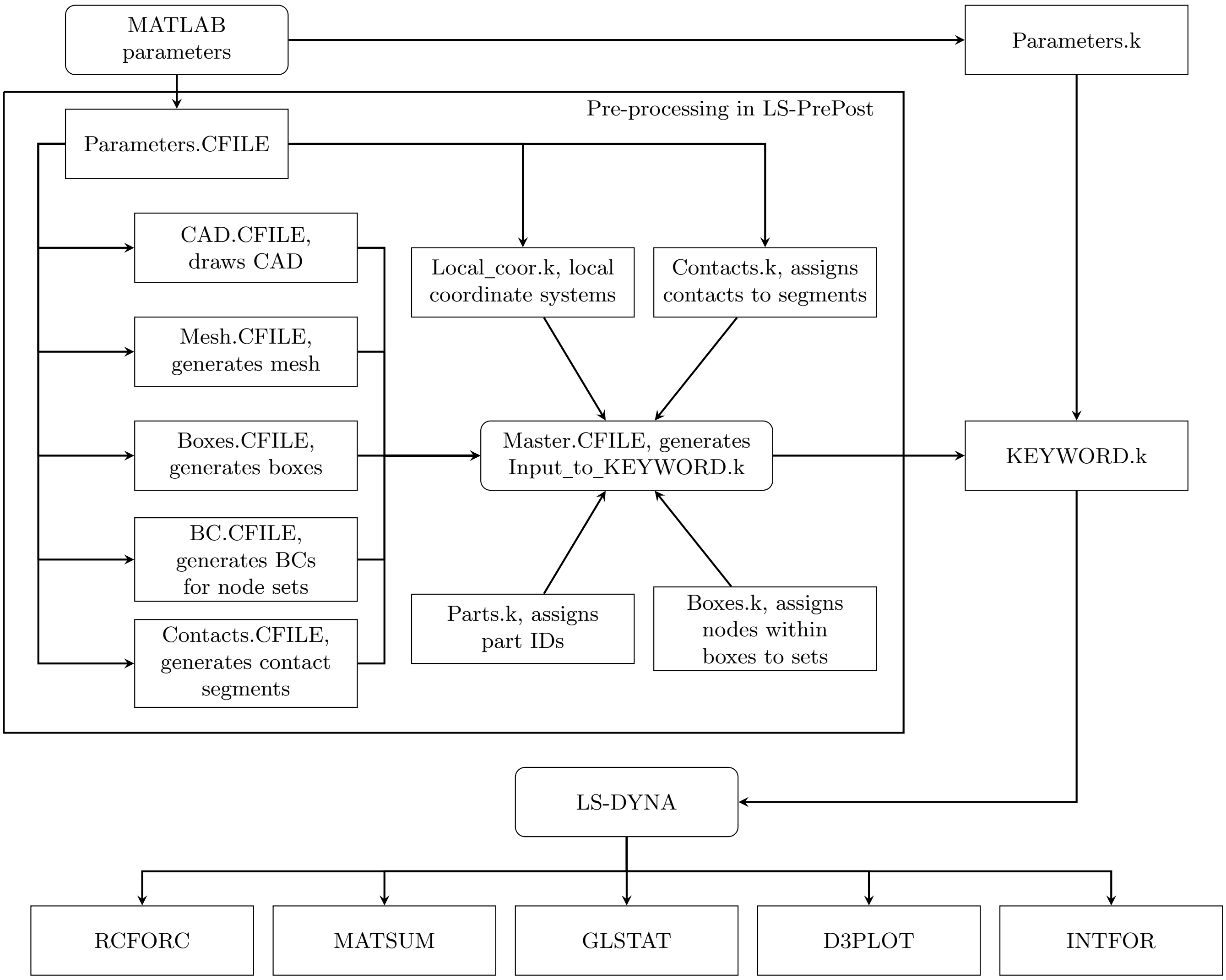

Figure 4.8: Model Structure. A box in a keyword is a selection method. Here it is used to select nodes, such a set of nodes can be defined. Segments are surfaces which are in contact. RCFORC, MATSUM, GLSTAT, D3PLOT, and INFOR are result files containing different information.

The model is structured such all varying parameters in the model are defined in a MATLAB script. This are parameters regarding: Geometry, mesh, material, contacts, boundary conditions, dump rate to result files, impactor velocity, and termination time. The model structure is seen in Figure 4.8. The model is build using two different types of files: Command files (.CFILE) and keyword files (.k). More can be read about command files and keyword files in appendix C.

With these considerations regarding the model, the first initiating simulation of the joint can be made. However, as mentioned in section 4.2.3, it is desired to study the deformation mechanism and the effect of the adhesive bond. Therefore the first simulation is made with the simplest assumption, from which more advanced formulations of the "Y" section can be added.

4.4 Deformation without adhesive bond

As described in section 4.3, only a "Y" section is necessary to model, due to the symmetry of a perfect honeycomb structure. When modelling the "Y" section, boundary conditions are applied as described in section 4.3. The material parameters are based on aluminium alloy 5052 -o sheet from [Varmint Al, 2019]. This choice is made because the tested honeycomb in chapter 3 is made of the same alloy [Easycomposites, 2020].

With the different parameters determined, two models are made; one is simplified to consist of one part, with one wall twice as thick as the other two walls. The other model is made with separation between the two cell walls without a bond between the two.

4.4.1 Double-wall thickness

The most straightforward approach to deal with the two walls is to "not deal with it" by modelling the two walls as one wall with double thickness, as illustrated in Figure 4.9.

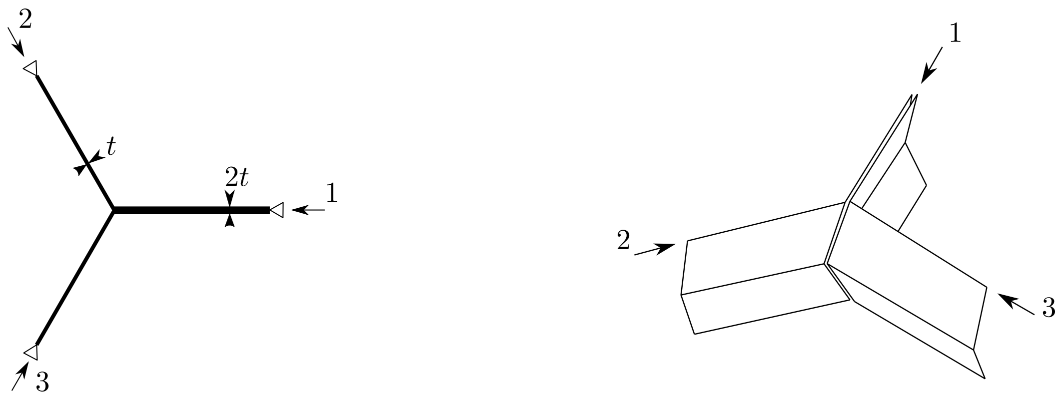

Figure 4.9: The two walls bonded with an adhesive modelled as one wall with double thickness. Arrows and numbering denote orientation of view on Figure 4.11.

With this simplification, the model cannot simulate the partial separation of the bonded walls, as shown on the right of Figure 4.6. Instead, the "Y" section is modelled as a firm joint. Consequently, the deformation mode is expected to be as on the right of Figure 4.9. This deformation mode should require more work to deform the honeycomb structure, than a model with a adhesive bond and the real structure. However, due to the simplicity of the model, it is easy to simulate and from thereon apply more advanced formulations.

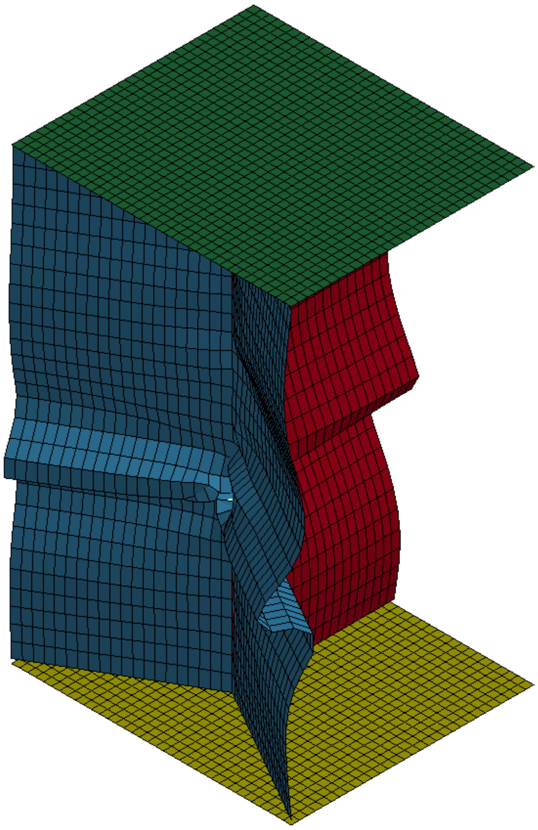

Figure 4.10: 3D view of simulation with double wall thickness. Green is the impactor, Red is the wall with double thickness, blue is the walls with normal thickness and yellow is the ground. Wall 1 and 3 deform in the same direction and wall 2 deform oppositely.

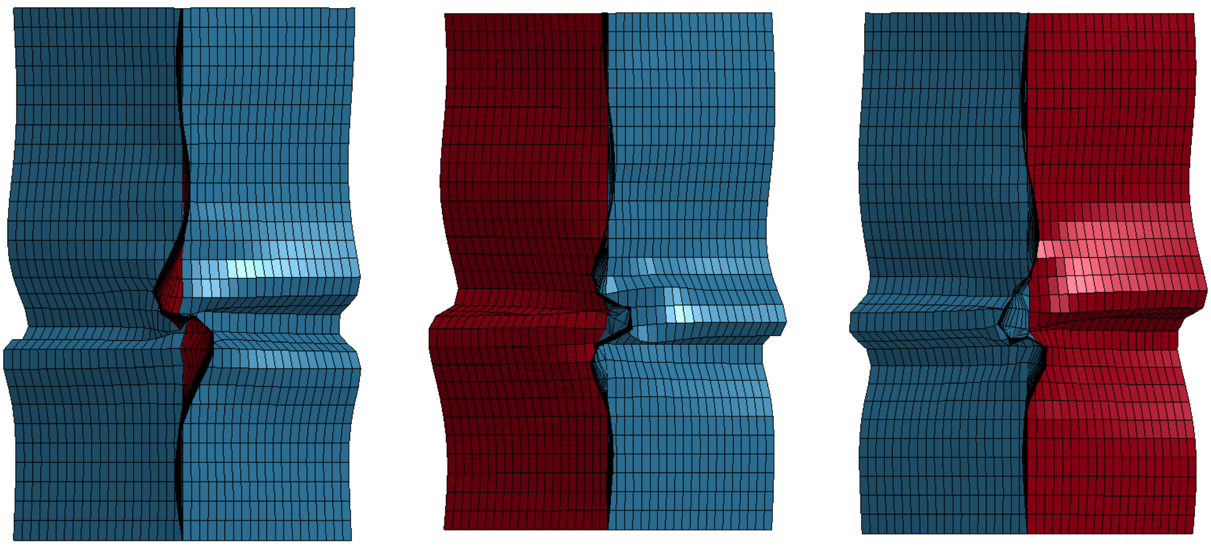

Figure 4.11: Edge view with orientation 1, 2, and 3 from Figure 4.9. Red is the wall with double thickness. Wall 1 and 3 deform in the same direction and wall 2 deform oppositely.

From the simulation in Figure 4.10 and 4.11, it is seen that the deformation of the "Y" section is similar to the firm joint in Figure 4.9, where the two single thickness walls deform in the same direction, and the double thickness wall deforms to one of the sides. Since this model behaves as expected, it is decided to continue with the implementation of a more advanced model, such it is possible to simulate the adhesive bond.

4.4.2 Two walls no bond

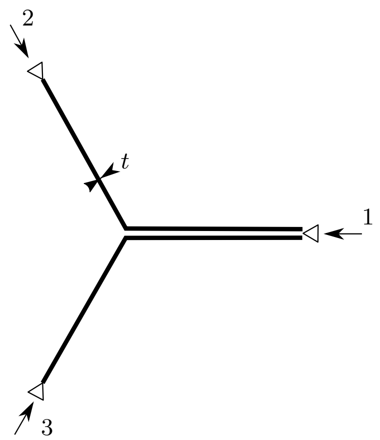

Figure 4.12: The two walls bonded with an adhesive modelled as two walls with no adhesive bond between. Arrows and numbering denote orientation of view on Figure 4.14.

Next advance is to model the two walls but with no bond in between. This means the two walls are free to separate but have contact when colliding. This is illustrated on Figure 4.12. However as seen on Figure 4.13 and 4.14, the deformation is quite unlike that of the right of Figure 4.6.

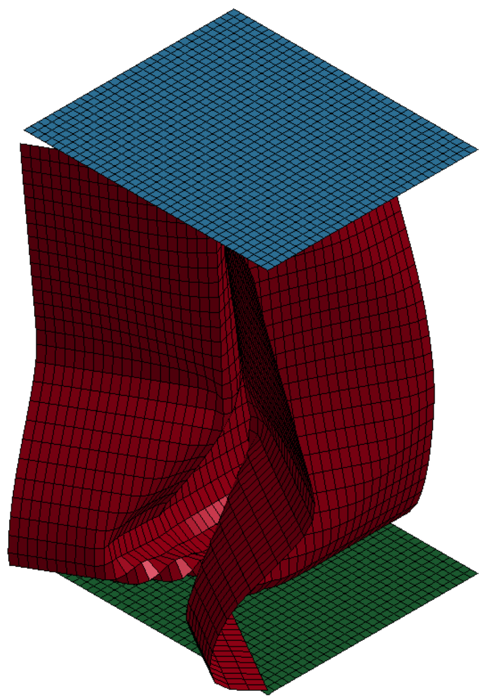

Figure 4.13: 3D view of simulation with two walls and no bond. The two walls split as the impactor hits the honeycomb.

Figure 4.14: View with orientation 1, 2, and 3 from Figure 4.12.

Figure 4.13 and 4.14 shows that the walls separate along the entire height from the very beginning of the deformation. Thus, further advancing the model is necessary.

4.5 Deformation with adhesive bond as contact

In LS-DYNA there are several contact formulations which can simulate an adhesive bond between two surfaces and several attempts are made using different contact formulations. However, all attempts failed using the model of the "Y". Two types of failure are observed; numerical instability or no effect of the adhesive at all. After several failed attempts using the model of the joint, a simpler model is constructed to test the contact formulations.

The simplified model consists of two plates on top of each other, where the top plate is peeled off, while the bottom plate is fixed. The plates in this simplified model has a length of 1 m, a width of 0.1 m and a thickness of 0.005 m. The boundary conditions for the model is shown in Figure 4.15 along with the dimensions of the plates. It is chosen to use solid elements to test the contact formulations as they are more general in their behaviour, and no simplification through the thickness is needed as it would with shell elements. However, when an appropriate contact formulation is found, it is tested using shell elements before applying it to the joint model.

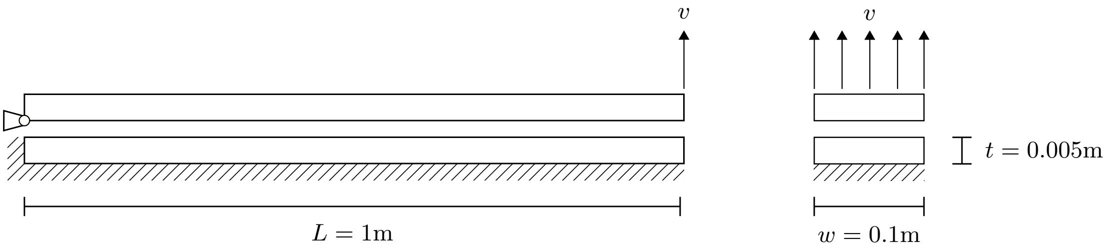

Figure 4.15: Boundary conditions for the two plates. The lower plate is fully constrained in one end and along the bottom. The top plate is constrained in translations in one corner and in the opposite corner a velocity is applied the top nodes. The plates are separated on this figure to show there are two plates. However, as it is seen on Figure 4.17, the plates are adjacent.

4.5.1 Contact formulations in LS-DYNA

Several different contact formulations are investigated to model the adhesive bond between the two plates of the simplified model. The different options and the basics of the keyword is seen in appendix D. However, it has been found that the keyword
*CONTACT_AUTOMATIC_SURFACE_TO_SURFACE_TIEBREAK, with OPTION = 5 is the most suitable to model the adhesive bond between the plates. For OPTION = 5 there is two yield criteria; one for tension and one for compression. The criteria are

$$f\left(\sigma_n, \sigma_s\right) = \frac{\sqrt{\sigma_n^2 + 3|\sigma_s|^2}}{NFLS} \leq 1 \tag{4.13}$$

for tension and

$$f\left(\sigma_s\right) = \frac{\sqrt{3|\sigma_s|^2}}{NFLS} \leq 1 \tag{4.14}$$

for compression. Where $NFLS$, is the yield strength, σ_n, and σ_s is the normal tension and shear stress between the two segments in contact, respectively. When the criterion is reached the stress strain relation becomes perfectly plastic. The interface stiffness is calculated on the element level as:

$$k_i = \frac{SF\ K_i\ A_i^2}{V_i}\ SF_{dmg} \tag{4.15}$$

for solid elements and as:

$$k_i = \frac{SF\ K_i\ A_i}{max(shell\ diagonal)}\ SF_{dmg} \tag{4.16}$$

for shell elements. Where SF is a scale factor, K_i is the bulk modulus of the element, A_i is the area of the element surface in contact, V_i is the element volume, and $max(shell\, digonal)$ is the longest diagonal in the shell. SF_{dmg} is a scale factor from a damage model. The damage model must be defined such it in some fashion, decent from unity to zero at a critical gap. Initially, it is chosen to model SF_{dmg} as a linear function of the gap opening:

$$SF_{dmg}\left(Gap\right) = -\frac{1}{Gap_{crit}}\ Gap + 1 \tag{4.17}$$

Where Gap is the size of the gap opening and Gap_{crit} is the critical gap opening. The simplest model of SF_{dmg} would be to keep it constant until a critical gap. However, it is chosen to use a linear function to make the failure less brittle but still fairly simple.

4.5.2 Simplified model

The simplified model is set up using the material and model parameters in Table 4.1 for the adherents where the plates have a length of 1 m, a width of 0.1 m and a thickness of 0.005 m. In this model the plasticity and hardening is not of interest, thus, a simple linear elastic material model is used.

Variable		Value	Unit
Material Parameters			
Young's Modulus	E	68.00	GPa
Poisson's ratio	ν	0.33	-
Bulk modulus	K	66.67	GPa
Density	ρ	2.80	ton/m^3
Adhesive Parameters			
Yield strength	$NFLS$	3.00	MPa
Critical gap	Gap_{crit}	1.00	mm
Stiffness scale factor	SF	0.10	-

Table 4.1: Model parameters.

These plates are each divided into ten elements along the length, i.e. $nelem = 10$, and one element in both the width and thickness, see Figure 4.17. Thus, following equation 4.15, the interface stiffness of the model is:

$$A_i = w\,\frac{L}{nelem} = 0.01\,\mathrm{m}^2 \qquad \text{and} \qquad V_i = A_i\,t = 50\text{E-}6\,\mathrm{m}^3 \tag{4.18}$$

$$k_i\,(Gap) = 13.33\text{E}9\,\mathrm{N/m}\,SF_{dmg}\,(Gap) \qquad \text{where} \qquad SF_{dmg}\,(Gap) = -\frac{1}{1\,\mathrm{mm}}Gap + 1 \tag{4.19}$$

The interface stiffness is plotted vs the gap opening on Figure 4.16.

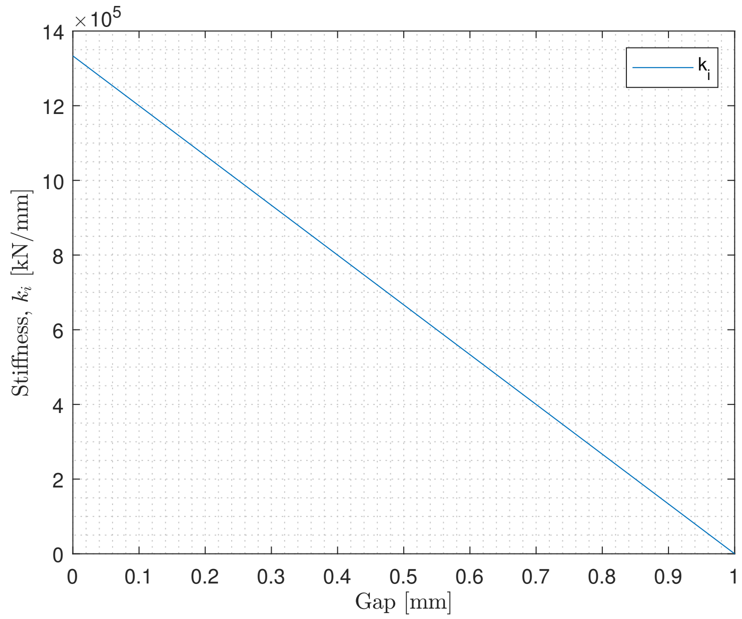

Figure 4.16: Stiffness vs gap.

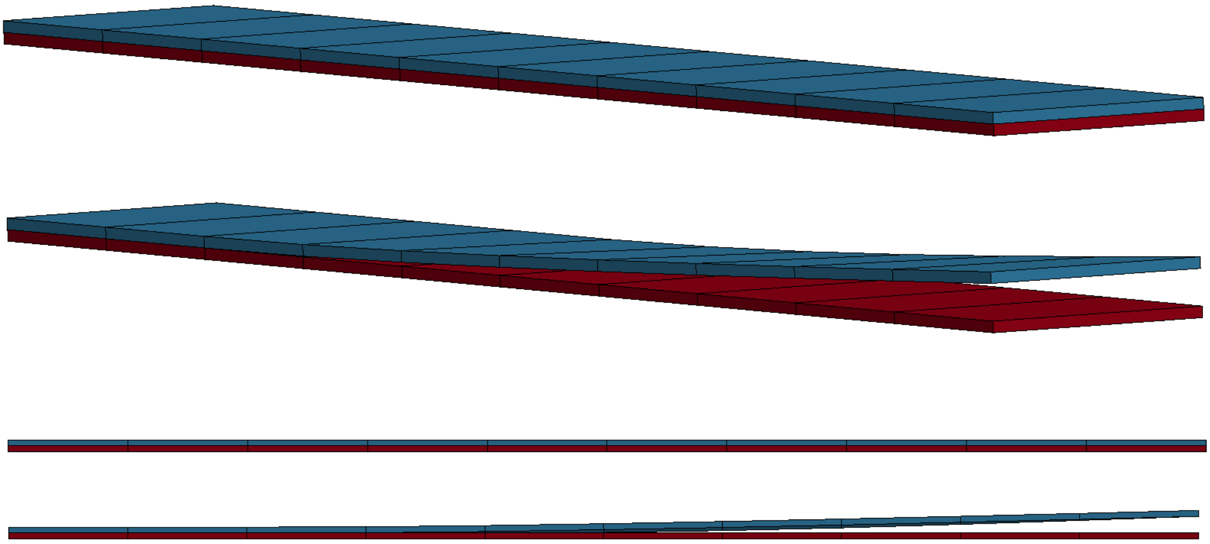

Figure 4.17: Simple model of two plates with solid elements. Red and blue elements are adjacent but do not share nodes i.e. contacting nodes are coincident but not merged.

In Figure 4.17, the elements of the simplified model are shown before and after deformation, where it is seen that the apparent deformation works as it should. However, when the yield criterion from equation 4.13 is examined for the outermost element, it is seen that the yield criterion is within the permissible range, i.e. $f(\sigma_n) \leq 1$, and therefore no debonding should occur, see Figure 4.18.

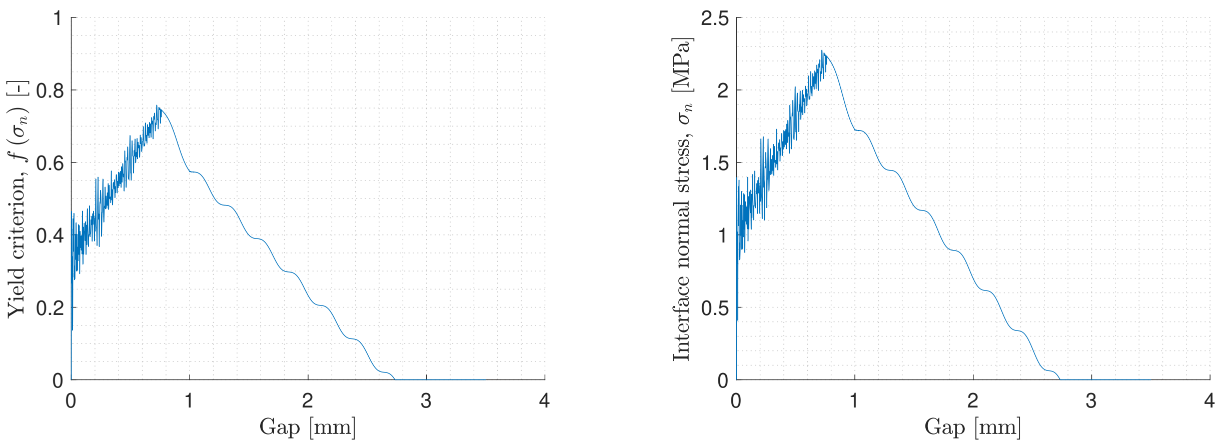

Figure 4.18: *Left:* $f(\sigma_n)$ vs gap opening. *Right:* Zoom of first 1 mm of σ_y vs gap opening. The gap opening is defined as the top element displacement in the normal direction.

Furthermore, from Figure 4.18, it is seen that the interface stresses become zero at a gap of approximately 2.8 mm. However, the interface stiffness (k_i) should be zero at a 1 mm gap according to equation 4.19, i.e. the stresses should also be zero at a gap of 1 mm. From the interface stresses in Figure 4.18, it is also seen that there is noise on the stresses. Based on these results, it is decided to investigate why debonding occurs, when the yield criterion is not reached. The yield criterion is investigated by simplifying the model to two solid elements stacked on top of each other, as shown in Figure 4.19.

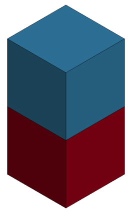

Figure 4.19: Two element model.

4.5.3 Simplified model 2

In this model, the bottom four nodes of the red element are constrained from any displacement, while a displacement with constant velocity is applied to the top four nodes of the blue element, see Figure 4.19. The two elements are cubes with side lengths of 1 m, which means that the area of the element surface contact (A_i) and the element volume (V_i) becomes $1\,\mathrm{m}^2$ and $1\,\mathrm{m}^3$, respectively. By using the same material and adhesive parameters as for the two plates, i.e. the parameters in Table 4.1, the interface stiffness should be:

$$k_i\,(Gap) = 6.67\mathrm{E}9\,\mathrm{N/m}\,SF_{dmg}\,(Gap) \qquad \text{where} \qquad SF_{dmg}\,(Gap) = \frac{1}{1\,\mathrm{mm}}Gap + 1 \tag{4.20}$$

However, when analysing the interface stress and yield criterion for this simulation, it is seen that the interface stiffness (k_i), does not fit with this function. From Figure 4.20, it is seen that the normal stress (σ_n) reaches peak stress of 2.66 MPa at a gap opening of 0.1142 mm. With these results, it is possible to determine the stiffness by using a backward difference at the peak stress:

$$k_i \approx \frac{(2.66\,\mathrm{MPa} - 2.64\,\mathrm{MPa})\,1\,\mathrm{m}^2}{0.1142\,\mathrm{mm} - 0.1129\,\mathrm{mm}} \approx 16.48\mathrm{E}9\,\mathrm{N/m} \tag{4.21}$$

Where the interface stiffness should be 5.92E9 N/m according to equation 4.20.

$$k_i(0.1141\,\mathrm{mm}) \approx 5.92\mathrm{E}9\,\mathrm{N/m} \tag{4.22}$$

This means that the stiffness is actually 2.78 times larger than the anticipated stiffness.

$$\frac{16.48\mathrm{E}9\,\mathrm{N/m}}{5.92\mathrm{E}9\,\mathrm{N/m}} \approx 2.78 \tag{4.23}$$

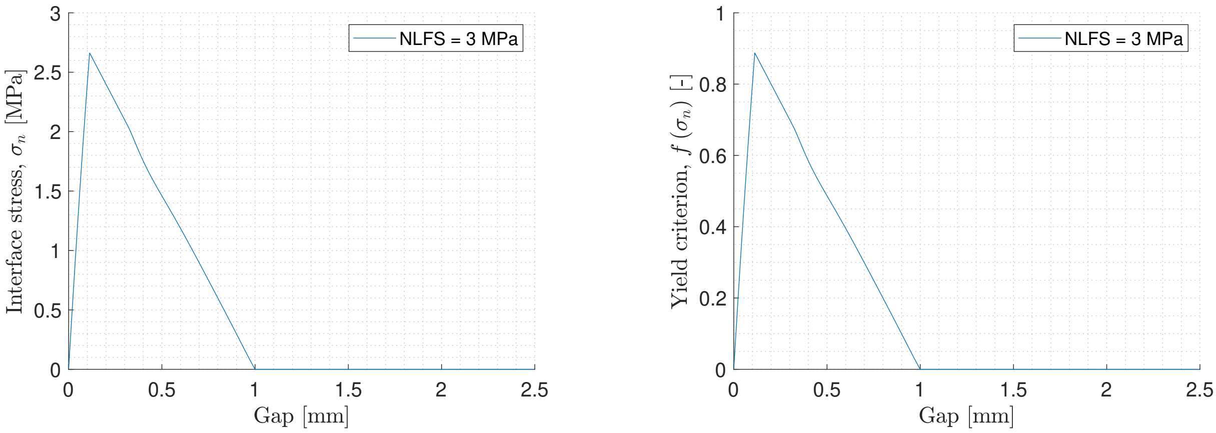

Figure 4.20: *Left:* Stress vs gap opening in the two element model. *Right:* $f\,(\sigma_n)$ vs gap opening in the two element model.

This difference in the interface stiffness is problematic because it renders the prediction of the stiffness impossible. Furthermore, several simulations with different values for the yield strength ($NFLS$) has been made, see Figure 4.21.

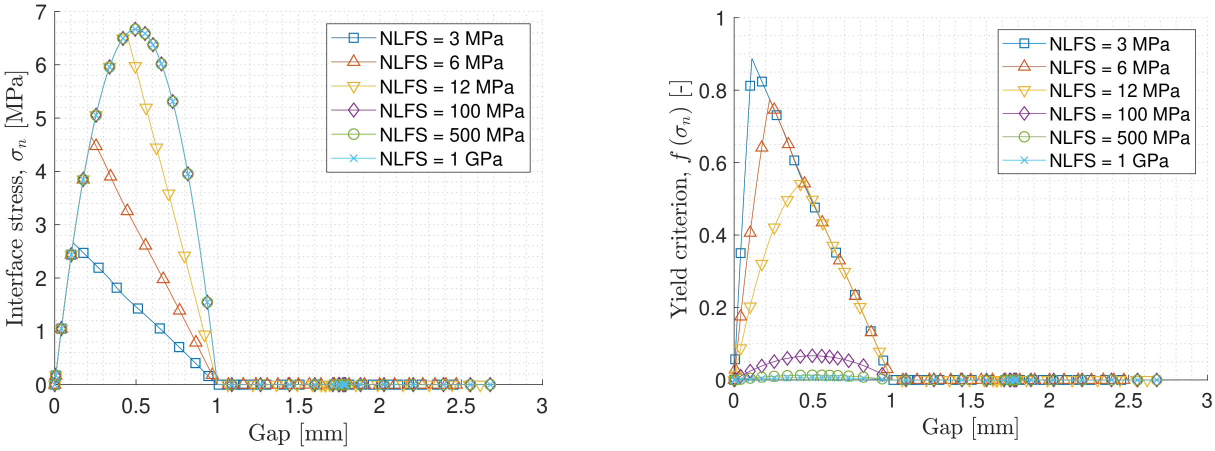

Figure 4.21: *Left:* σ_n vs gap opening for different values of $NFLS$. *Right:* σ_y vs gap opening for different values of $NFLS$. In both *left* and *right* $i\# = 50$.

The left of Figure 4.21 shows that the stress is a quadratic function of the gap. This is because the stiffness is a linear function of the gap:

$$\sigma_n\left(Gap\right) = \frac{k_i\left(Gap\right)\ Gap}{A_i} = \frac{\frac{SF\ K_i\ A_i^2}{V_i}\left(-\frac{1}{Gap_{crit}}\ Gap + 1\right)\ Gap}{A_i}$$
$$= \frac{SF\ K_i\ A_i}{V_i}\left(-\frac{1}{Gap_{crit}}\ Gap^2 + Gap\right) \tag{4.24}$$

The right of Figure 4.21, shows that it is not only the interface stiffness which is scaled with SF_{dmg} but also $NFLS$. Thus, the yield criterion in equation 4.13 is not true and it should be:

$$f\left(\sigma_n,\sigma_s\right) = \frac{\sqrt{\sigma_n^2 + 3\ \left|\sigma_s\right|^2}}{NFLS\ SF_{dmg}} \leq 1 \Rightarrow \frac{\sqrt{\sigma_n^2 + 3\ \left|\sigma_s\right|^2}}{NFLS} \leq SF_{dmg} \tag{4.25}$$

When yielding occur, i.e. $f\left(\sigma_n,\sigma_s\right) \geq SF_{dmg}$, the interface stresses are determined from the plastic yield stress scaled with SF_{dmg}, due to the perfect plasticity.

$$\sigma_n = NFLS\ SF_{dmg} \tag{4.26}$$

In this model $\sigma_s \approx 0$ and therefore not plotted.

However, the discrepancy between the expected interface stiffness and the actual interface stiffness in the model is of concern. This is investigated by implementing the calculation of the interface stress as a function of the gap in MATLAB. In the implementation, equation 4.15, 4.24 and 4.25 are used, to determine the interface stiffness, stress and yield criterion, from which the gap is increased from zero incrementally at a fixed step size. The implementation of the functions and criterion is illustrated in Figure 4.22.

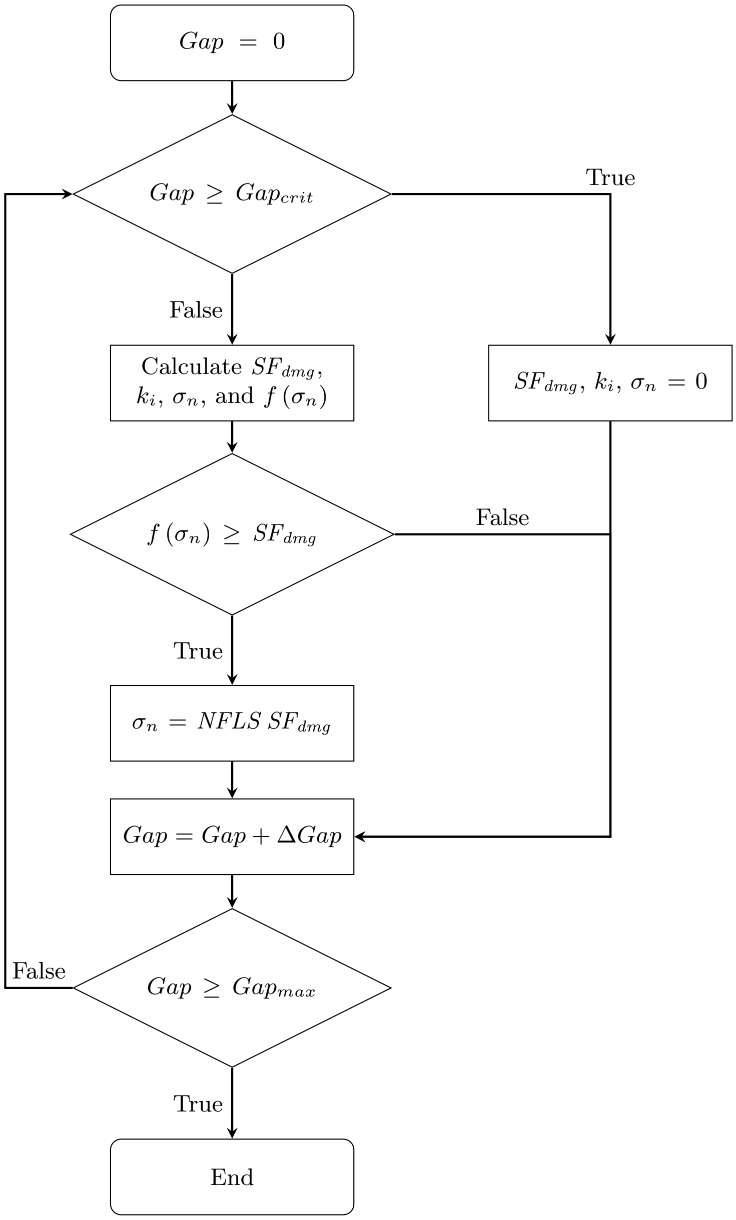

Figure 4.22: Flowchart of MATLAB simulation.

In the MATLAB script, the same material and model parameters are used, while the plastic yield stress (NFLS) is set to the six values used in the model. The result of these calculations is seen in Figure 4.23. Here it is seen that the shape of the curves is similar to those of Figure 4.21. However, the interface stresses are smaller, and the yield criterion is only reached for $NFLS = 3\text{MPa}$.

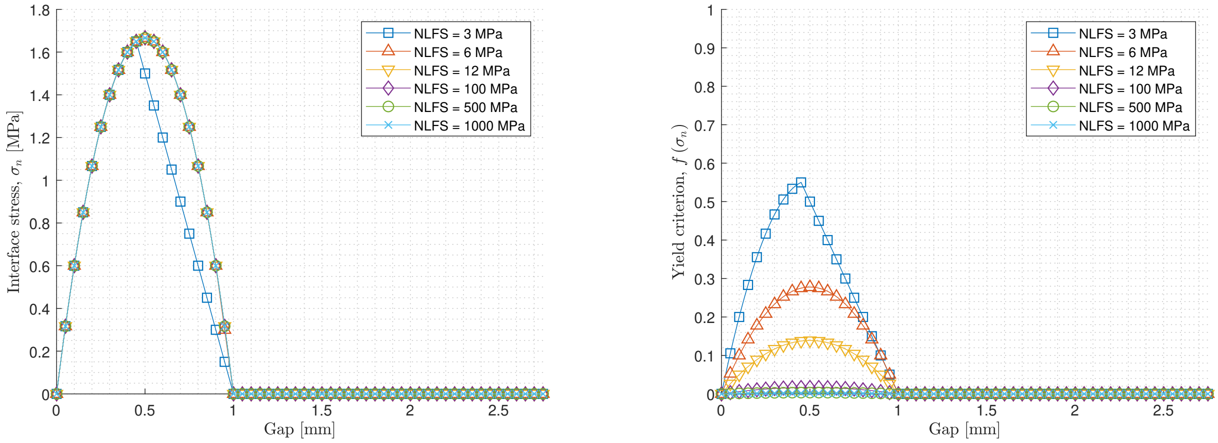

Figure 4.23: *Left:* σ_n vs gap opening for different values of *NFLS*. *Right:* σ_y vs gap opening for different values of *NFLS*. In both *left* and *right* $i\# = 500$

Therefore, it is attempted to see if the difference is caused directly by the difference in interface stiffness from equation 4.23. This difference is implemented by scaling the scale factor, SF by 2.78, such:

$$SF = 0.278 \tag{4.27}$$

The results of this are seen in Figure 4.24.

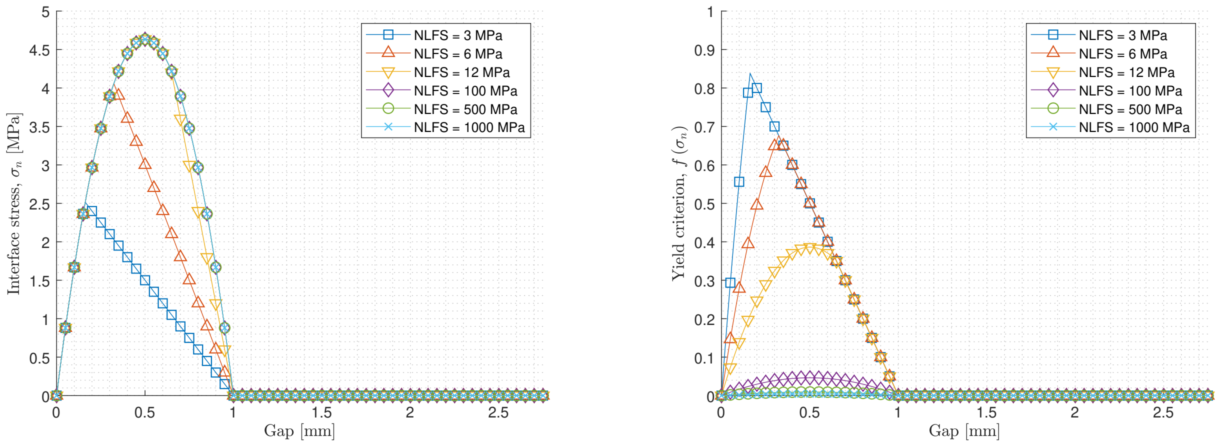

Figure 4.24: MATLAB simulation with $SF = 0.278$. *Left:*$f(\sigma_n)$ vs gap opening for different values of *NFLS*. *Right:* σ_y vs gap opening for different values of *NFLS*. In both *left* and *right* $i\# = 500$

By scaling the scale factor, it is seen that the results are closer to the results from the LS-DYNA simulation but is not identical. Further investigations of the scale factor have shown that for a scale factor of 0.4, i.e.:

$$SF = 0.4 \tag{4.28}$$

The results of the LS-DYNA simulation and the MATLAB script are practically coincident, as it is shown in Figure 4.25

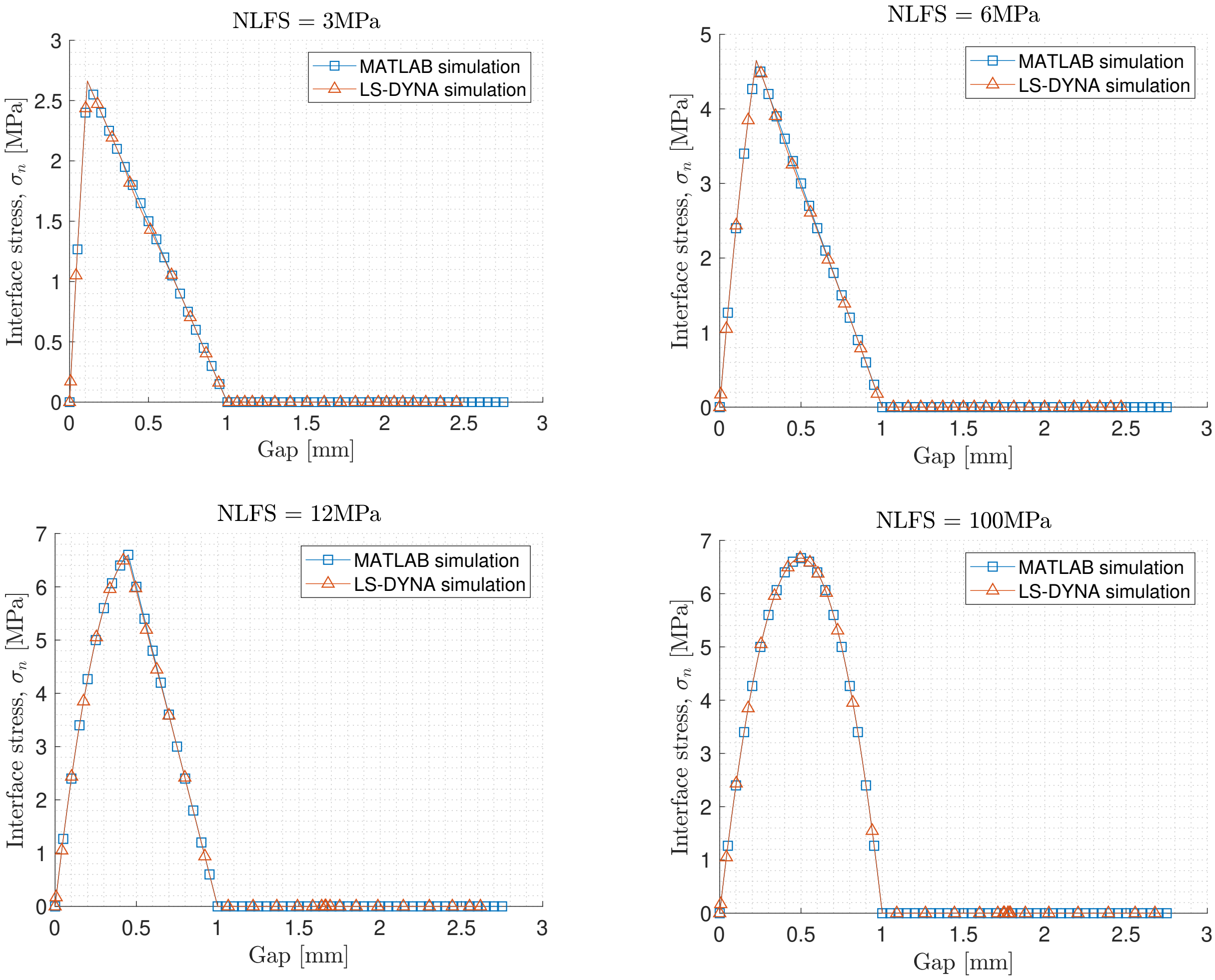

Figure 4.25: σ_n vs gap opening for different values of *NFLS* for MATLAB simulations and LS-DYNA simulation where the scale factor *SF* is scaled by 4 in the MATLAB simulation. For MATLAB simulations $i\# = 500$, and for LS-DYNA simulations $i\# = 50$.

The fact that the results practically are the same when multiplying the scale factor by four and thereby also the stiffness by four is suspicious. However, nothing in the LS-DYNA keyword file indicates that the stiffness is multiplied by four. Similarly, nothing in the MATLAB script divides the stiffness by four.

After further investigations, it is found that the interface stiffness works on a nodal level which complies with the stiffness being four times bigger than expected — the segment in contact is the surface of one element side which is spanned by four nodes. Thus, the segment interface stress is equal to the sum of "stresses" in the nodes of which the segment is spanned by, i.e. the segment interface stress for the two-element model is:

$$\sigma_n = \frac{n_{nodes}\, k_i\, Gap}{A_i} = \frac{4 \cdot 6.67\,\mathrm{N/m}\left(-\dfrac{1}{1\,\mathrm{mm}}\,Gap^2 + Gap\right)}{1\,\mathrm{m}^2} \tag{4.29}$$

With the two-element model, it is also found that the critical gap works as intended, but the critical gap also works on a nodal level. Thus, the problem in Figure 4.18 is not the contact formulation but the displayed data, where the interface stress vs gap opening of the solid plate model is shown in Figure 4.26 for two nodes in the outermost element.

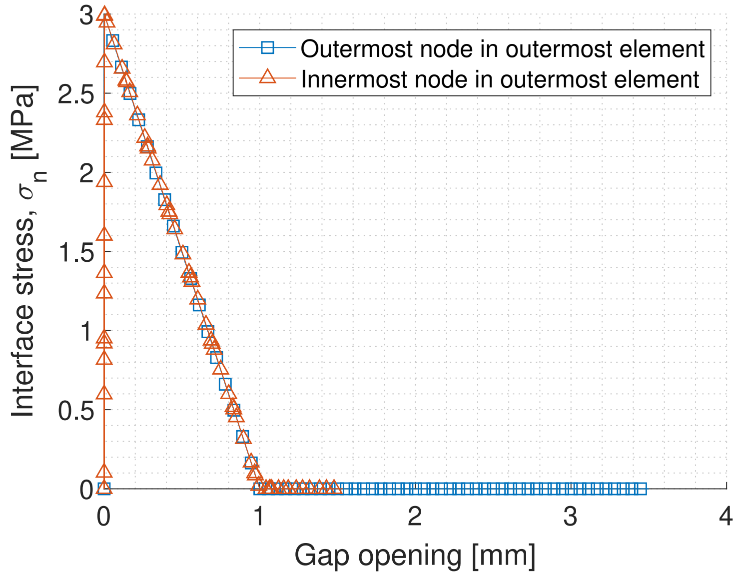

Figure 4.26: Stress vs gap opening in the two plate model. $i\# = 75$

On Figure 4.26 the stress seems to go to the yield stress immediately, this is because the stiffness is rather large compared to the yield stress.

There is still the problem with the noise in the data of Figure 4.18. However, these oscillations are to be expected when the adherents are flexible. Further, with only one element in the width of the adherents, the delamination is an "all or nothing" relation, i.e. adding a few more elements in the width of the plates would probably fix most of the noise problems. Finally, no damping is included in the simulation. Thus, when a vibration begins, there is nothing that stops it again, which is tested with the shell elements.

With the problems of the solid model addressed, the contact formulation is applied to the plate model, modelled with the Belytschko-Tsay shell element formulation.

4.5.4 Shells

The two plate model, with the Belytschko-Tsay shell element formulation, is modelled with the same parameters and dimensions as that of the two plate model with the solid element formulation. Figure 4.27 shows the model with the shell element formulation before and after deformation.

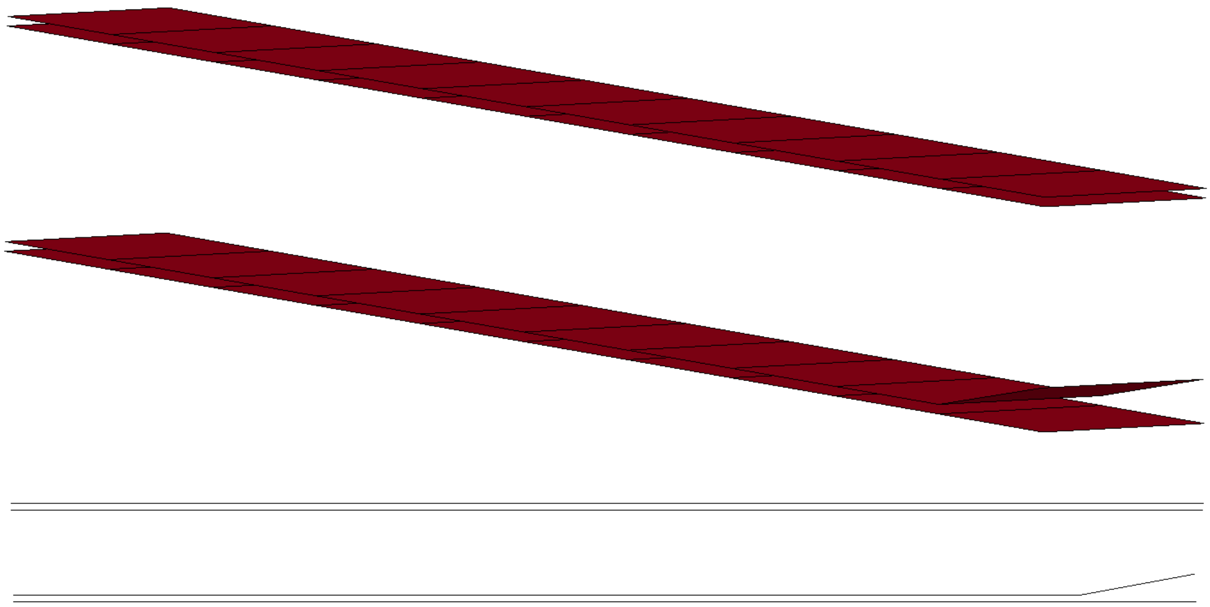

Figure 4.27: Simple model of two plates with shell elements. Shells form a mid-plane, thus, the thickness of the shells are coincident.

Figure 4.27 shows quite a different deformation than the same model with solid elements — the solid element deform as a whole along the length, whereas the shells deform elementwise. This deformation is probably due to two things; the shell element formulation is softer than the solid element formulation, and the adhesive bond is defined between the mid-points of the geometry rather than the top and bottom. However, as seen in Figure 4.28, the instability of the "all or nothing" relation becomes significant in shells. In Figure 4.28, it is seen that the adhesive contact formulation makes the simulation unstable as soon as it breaks in the innermost nodes of the outermost element.

Figure 4.28: Two plates at time 0.039 s and and time 0.05 s.

Both the deformation and stability problem is solved by refining the mesh in the model, see

Figure 4.29. Here it is seen that applying more elements stabilises the simulation, and the deformation becomes like that of the solids.

Figure 4.29: Two plates before simulation and at time 0.1 s.

With the adhesive contact formulation examined and properly understood, it is implemented in the model of the joint.

4.5.5 Two walls with an adhesive bond

The adhesive contact formulation is implemented in the model of the joint, as illustrated in Figure 4.30, with the material and model parameters tabulated in Table 4.2.

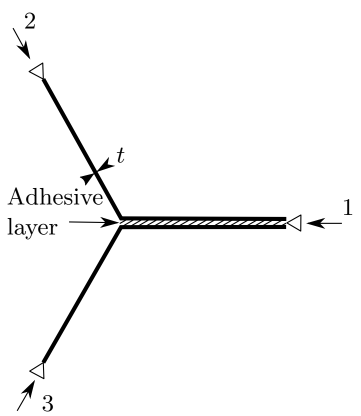

Figure 4.30: The two walls bonded with an adhesive where the adhesive is modelled as a contact. Numbered arrows denote orientation of view on Figure 4.33.

Variable		Value	Unit
Model parameters			
Mass scale	ms	1	-
Integration points	nip	9	-
Impact velocity	v	8	m/s
Material Parameters			
Young's Modulus	E	70.32	GPa
Strength coefficient	k	350.00	MPa
Hardening exponent	n	0.25	-
Poisson's ratio	ν	0.33	-
Bulk modulus	K	68.94	GPa
Adhesive Parameters			
Yield strength	$NFLS$	30.00	MPa
Critical gap	Gap_{crit}	0.01	mm
Stiffness scale factor	SF	0.10	-

Table 4.2: Model parameters.

As described, the interface stiffness is calculated on a nodal level. Therefore, the interface stiffness of the adhesive contact formulation between two segments is dependent on element size and the number of nodes. As an example, the stiffness is calculated for an area with two different discretisations, as shown in Figure 4.31.

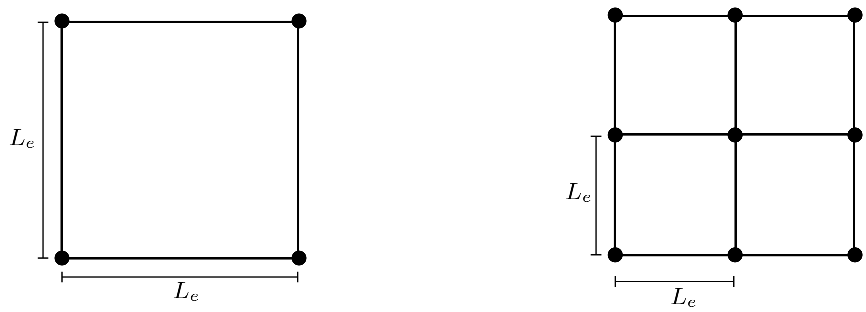

Figure 4.31: Two areas of equal size discretised into one and four elements, respectively. For the single element, four nodes are needed, and for the four elements nine nodes are needed.

In this example, two areas of equal size are discretised into one and four elements, where four and nine nodes are used, respectively. Following equation 4.16 the initial contact stiffness of each node:

$$k_{i,1} = \frac{SF\ K\ L_e^2}{\sqrt{2\ L_e^2}} = 4.87\text{E}6\,\text{N/m} \quad \text{and} \quad k_{i,4} = \frac{SF\ K\ L_e^2}{\sqrt{2\ L_e^2}} = 2.44\text{E}6\,\text{N/m} \tag{4.30}$$

Where $L_e = 1\,\text{mm}$ and 0.5 mm, respectively. The contact stiffness for the two segments (i.e. the full area) are the sum of the stiffness from each node in the segment.

$$k_s = \sum_{i=1}^{n_{nodes}} k_i \tag{4.31}$$

Thus, the segment stiffness for the one element and four element model is respectively:

$$k_{s,1} = 19.50\text{E}6\,\text{N/m} \quad \text{and} \quad k_{s,4} = 21.94\text{E}6\,\text{N/m} \tag{4.32}$$

It does not seem like a big difference; however, if increased to 16 elements, the segment stiffness is significantly increased:

$$k_{s,16} = 30.47\text{E6N/m} \tag{4.33}$$

Furthermore, the adhesive contact formulation also breaks at the nodes, which means that the segment stiffness decays as nodes are released. This decrease in segment stiffness is essential when considering peel effects as [Wierzbicki, 1983] determines to be the deformation mode. However, with these considerations, the stiffness as a whole is difficult to determine. Though, if the deformation mode described in [Wierzbicki, 1983] is modelled, with this contact formulation and model parameters, it is decided to continue and refine the model.

It is suspected that the strength and stiffness of the adhesive are quite insignificant in the amount of work needed to perform the deformation — i.e. the purpose of the adhesive is to guide the honeycomb walls into a particular deformation mode. Therefore, it is decided to make five different simulations, with different adhesive parameters of the plastic yield stress ($NFLS$), the critical gap (Gap_{crit}) and the stiffness scale factor (SF), see Table 4.3. The resulting force required to deform the joint with the five different adhesive samples is seen in Figure 4.32.

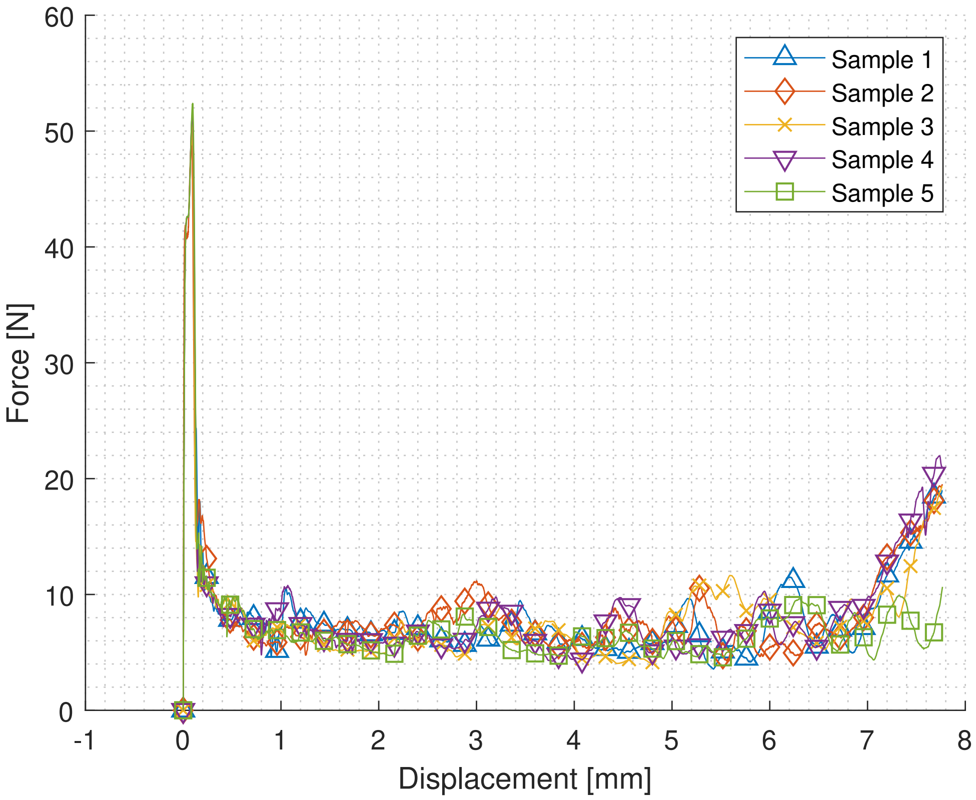

Figure 4.32: Force-displacement curve of simulations with different adhesive parameters. The parameters are tabulated in Table 4.3. The cell size in these simulations is larger than the cell size used in chapter 5, i.e. P_m is not comparable. $i\# = 300$

Variable		Value					Unit
		Sample 1	Sample 2	Sample 3	Sample 4	Sample 5	
Yield strength	$NFLS$	**30.00**	30.00	30.00	50.00	10.00	MPa
Critical gap	Gap_{crit}	**0.10**	0.10	0.01	0.01	0.01	mm
Stiffness scale factor	SF	**0.10**	0.20	0.10	0.10	0.10	-
Mean load	P_m	**6.74**	6.97	6.79	6.65	6.21	N

Table 4.3: Adhesive parameters and mean load. Mean load is calculated from 1 mm to 7 mm displacement. It is found that Sample 1 gives the best results. [Yamashita and Gotoh, 2004] uses 30 MPa as the yield stress for an adhesive in a honeycomb.

From these five simulations, it is first observed that the force-displacement curve has the expected behaviour, i.e. first a high peak load, followed by a load plateau and densification. Furthermore, the suspicion that the strength and stiffness of the adhesive are insignificant is confirmed, since the five different simulations all have the same behaviour and approximately the same mean load, see Figure 4.32 and Table 4.3. The deformation of the five simulations further proves this suspicion, since they are almost the same. In Figure 4.34, the deformation of sample 1 is shown from the three directions given in Figure 4.30.

Figure 4.33: Edge view with orientation 1, 2, and 3 from Figure 4.30. Red and blue is the wall with double thickness. Wall 1 and 3 deform in the same direction and wall 2 deform oppositely.

By inspecting the deformation of the joint, it is seen how the folding begins and how new folds are initiated. From this, it is clear that the adhesive contact partially breaks during every fold. This partial break of the adhesive is consistent with the deformation described in [Wierzbicki, 1983] and is illustrated in Figure 4.34, 4.35 and 4.36.

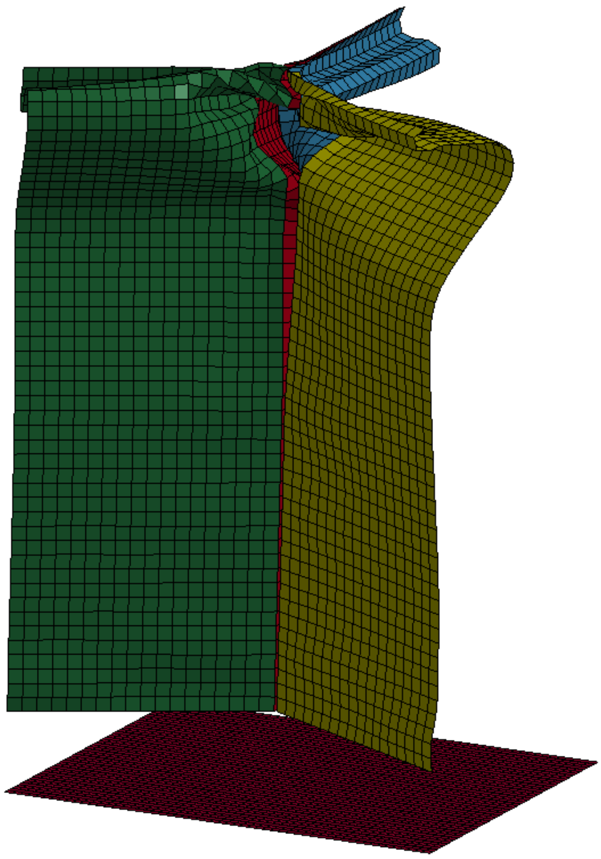

Figure 4.34: 3D view of the deformation, with adhesive contact.

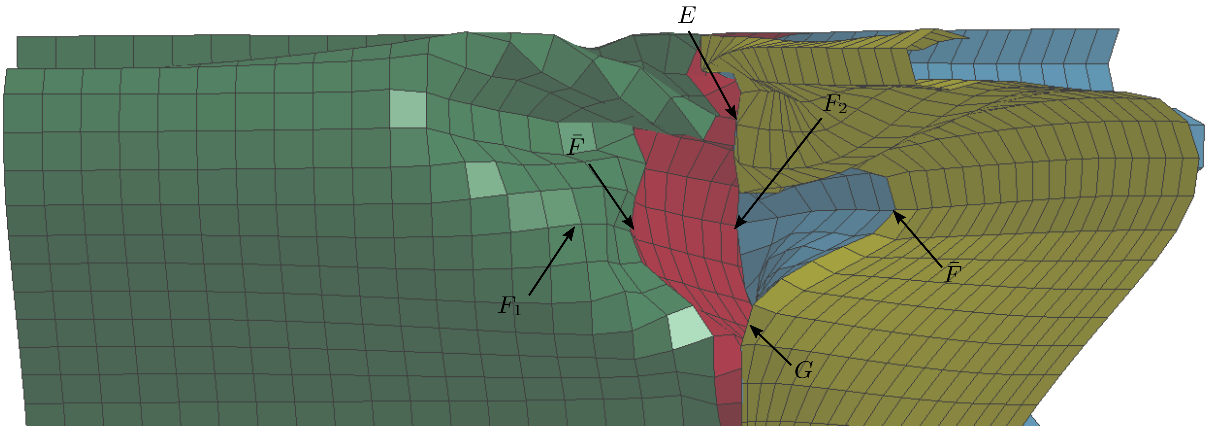

Figure 4.35: Zoom of the deformation. It is seen that the deformation is similar to that of Figure 4.36

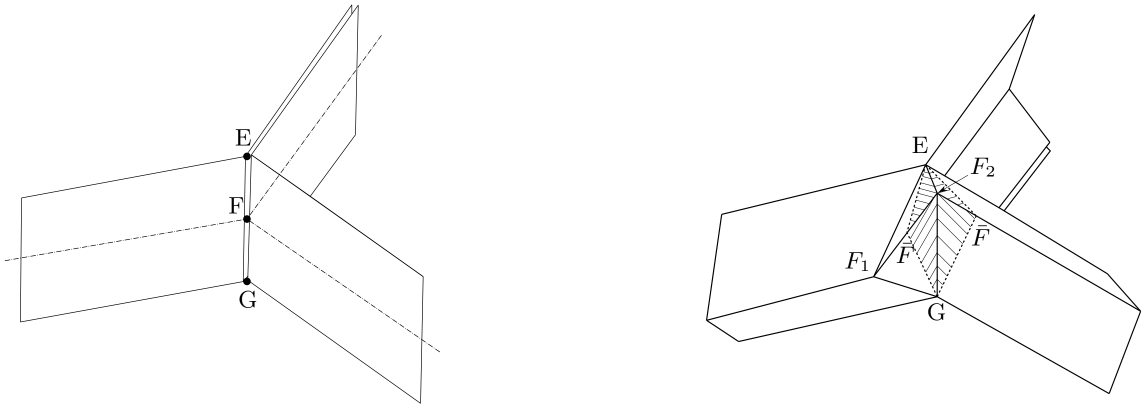

Figure 4.36: Deformation of honeycomb with adhesive between walls suggested by [Wierzbicki, 1983]. Repeated from Figure 4.6

With the model, able to simulate the deformation mode described in [Wierzbicki, 1983], it is decided to continue with the adhesive parameters of sample 1 and refine the geometry and material parameters of the aluminium used in the model.

5 — Model refinement

In this chapter, the geometry and material parameters are refined for the honeycomb model. The refinement in geometry is made, such it resembles the honeycomb test samples used in the experiments, which involves refinement in regards to the cell size, wall thickness, and a rounding of corners. The definitions of the cell parameters are shown in Figure 5.1.

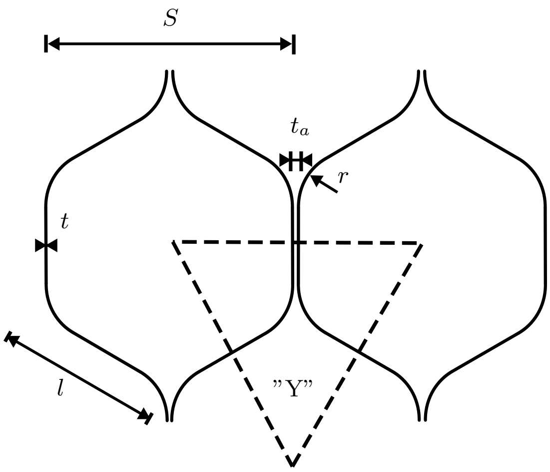

Figure 5.1: Definition of cell parameters. S is the cell size, l is the wall length, and r is the rounding radius. The dashed triangle illustrates the area which is modelled.

This illustration of the honeycomb cells is an idealised representation of the geometry. In reality, the shape of the honeycomb cells is far more random, as seen in Figure 5.2.

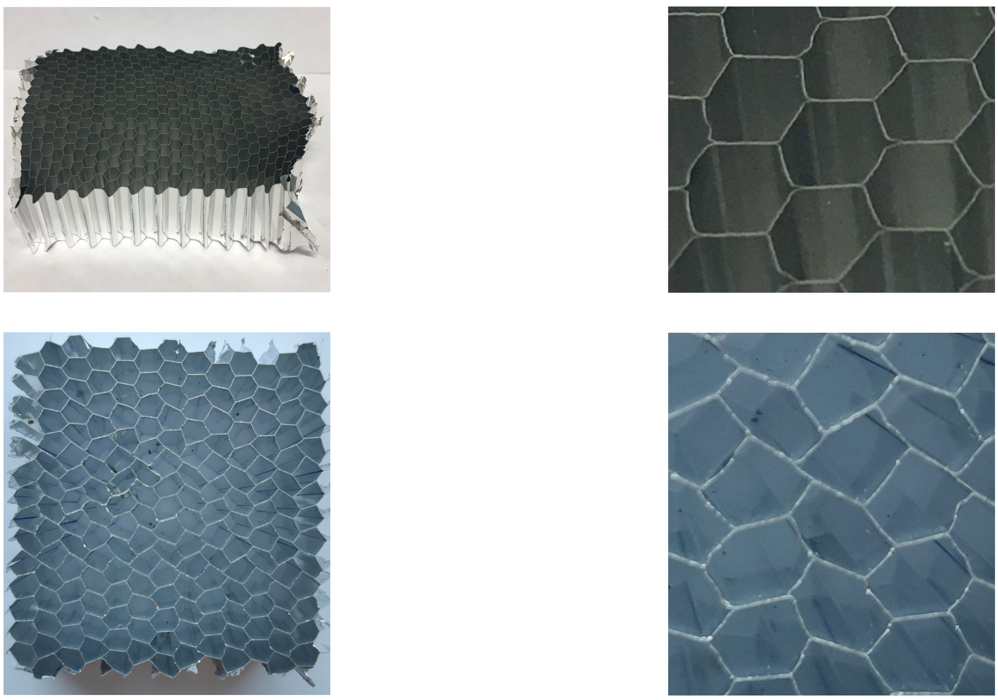

Figure 5.2: Two test samples cut from the same honeycomb.

5.1 Geometric imperfections

The reason for these imperfect cells is due to the manufacturing method of these honeycombs, described in section 4.2.2 and illustrated in Figure 5.3. Specifically, it is step 5 of the manufacturing process which needs consideration. Typically when buying honeycombs made with the expansion process, the supplier delivers HOBE slices due to cheaper logistics [Easycomposites, 2020]. The expansion of the honeycomb in step 6 is typically a coarse process, done by the customer, which leaves the cells distorted and uneven [Bitzer, 1997].

1. Foil material on a roll
2. Adhesive lines are printed and the foil is cut into sheets
3. The sheets are stacked into the HOBE (Honeycomb before expansion) block
4. The HOBE block are cut into HOBE slices with a desired thickness
5. Expand the HOBE slice to a honeycomb panel
6. Final product

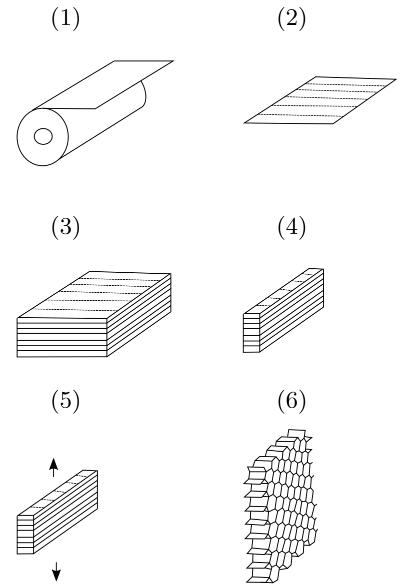

Figure 5.3: Honeycomb manufacturing using the expansion process. Edited from [Bitzer, 1997]. Repeated from Figure 4.4.

Thus, defining the geometry of the cells, such it fits on every cell is impossible, why an idealisation of the cells must be made. Therefore, a rounding radius is defined to resemble the somewhat organic shape of the actual honeycomb, seen in Figure 5.2. The model is shown in Figure 5.4 and has the parameters tabulated in Table 5.1.

Figure 5.4: Top view of model with and without thickness appearance.

Variable		Value	Unit
<u>Model parameters</u>			
Mass scale	ms	1	-
Integration points	nip	9	-
Impact velocity	v	8	m/s
<u>Aluminium Material Parameters</u>			
Young's Modulus	E	70.32	GPa
Strength coefficient	k	350.00	MPa
Hardening exponent	n	0.25	-
Poisson's ratio	ν	0.33	-
Bulk modulus	K	68.94	GPa
<u>Adhesive Parameters</u>			
Yield strength	$NFLS$	30.00	MPa
Critical gap	Gap_{crit}	0.1	mm
Stiffness scale factor	SF	0.10	-
<u>Geometric parameters</u>			
Cell size	S	3.200	mm
Rounding radius	r	0.200	mm
Wall thickness	t	0.035	mm
Adhesive thickness	t_a	0.001	mm

Table 5.1: Model parameters.

By implementing these geometric parameters in the model, the resulting force-displacement curve becomes the one seen in Figure 5.7, where the deformation associated with the peaks is also shown in Figure 5.7.

From picture 1 in Figure 5.7, it is seen that buckling initiates at both the top and bottom of the "Y" section, where wrinkles are seen at both ends before an actual fold/buckling mode occur. The initiation point of the buckling is not of concern since it is determined by rounding errors, which serve as imperfections in the model, thus, allowing the buckling to be initiated, as mentioned in section 4.3.2. In reality, the initiation of the buckling is determined by imperfections in the material, geometry, loading direction, etc. which is idealised in the model. These imperfections are also what causes the buckling to, sometimes, be initiated at both sides of the honeycomb, see Figure 5.5.

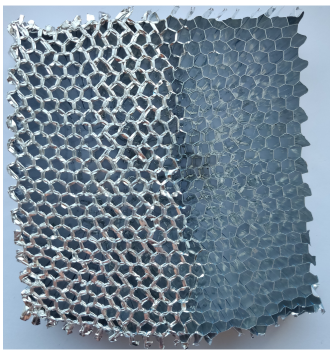

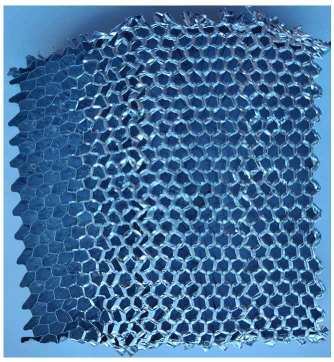

Figure 5.5: Buckling initiated on different sides of honeycomb.

After the buckling is initiated, it is seen that for every peak in the force-displacement curve, a new fold/bucking mode is initiated. Furthermore, the magnitude of the peaks from the simulation is more profound than the peaks obtained in the force-displacement curve for the static experiments, seen in Figure 5.6. The reason for this is suspected to be caused by the initiation of the buckling, in the static experiments, is out of phase, i.e. buckling modes in the full honeycomb is not necessarily initiated simultaneously. Thus, the measurable force is on average flatter. Therefore, a model of several cells is developed to test this suspicion, which is described in section 5.2.

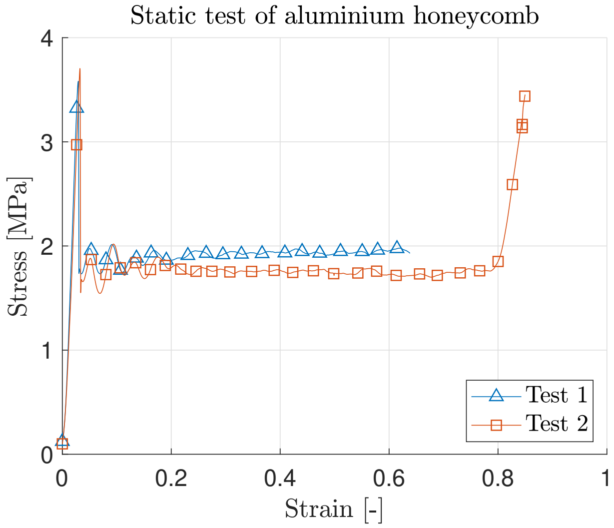

Figure 5.6: Stress-strain curve of hexagonal honeycomb from [Simonsen et al., 2019]. Repeated from Figure 2.1.

To compare the simulation with the experiments made in chapter 3, the mean load applied to the "Y" section is used. The mean load is determined from the force-displacement curve and is an integral measure of the work needed to deform the structure. Thus, information of the actual force-displacement curve is lost, i.e. it is a weak formulation. However, it is advantageous for comparison to reduce the information from an entire curve to a number. Though, a qualitative requirement must be defined for the deformation. In this project, the requirement is that the deformation follows the deformation described in [Wierzbicki, 1983].

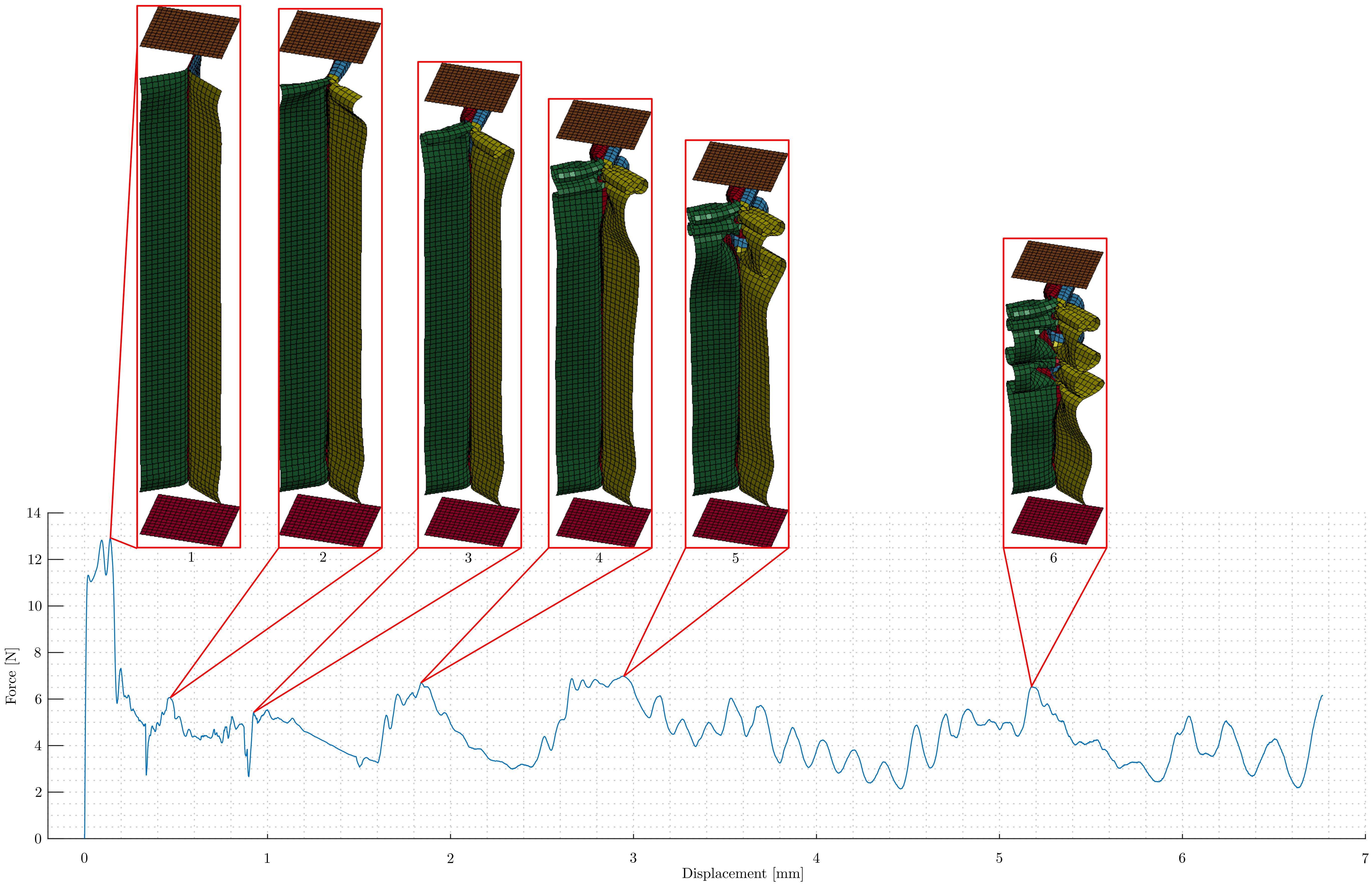

Figure 5.7: Force-displacement curve for the simulation made with the parameters in Table 4.2.

5.1.1 Results and scaling

Since precrushed honeycombs do not have a significant difference between peak and mean load, the peak load is not of interest, why only the mean load is used in the following. The mean load is calculated from a displacement of 0.175 mm to a displacement of 7 mm, which gives a mean load of $P_m = 4.48\,\text{N}$, for the force-displacement curve in Figure 5.7. However, to be able to compare this to the experimental data the model needs to be scaled appropriately.

The scaling of the model is done by determining how many "Y" sections are needed to fill a fixed nominal area. The number of "Y" sections needed is determined by making each "Y" section consist of a triangle, expanded by the centres of three neighbouring cells, see Figure 5.8. Thereby, only "Y" sections within the fixed nominal area are included in the scaling.

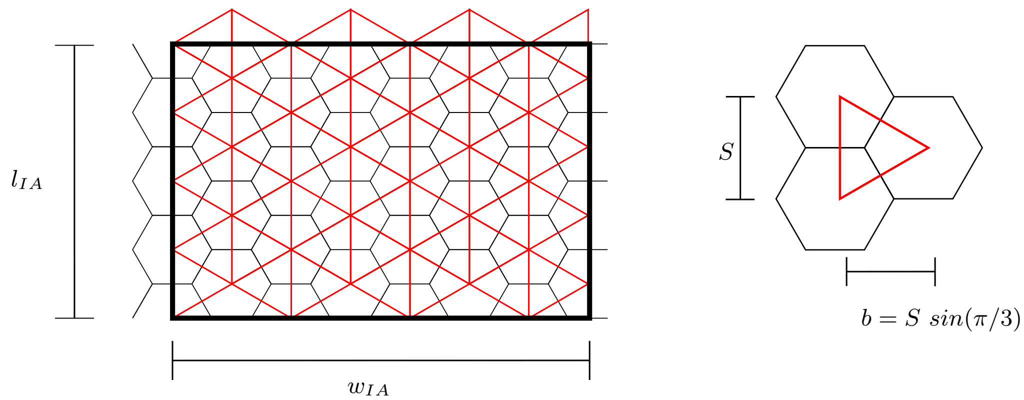

Figure 5.8: Determination of "Y" sections.

The determination of how many triangles can fit inside a fixed nominal area is carried out in the following way:

$$
\begin{aligned}
N_l &= \frac{l_{IA}}{S} \\
N_w &= \frac{w_{IA}}{b} \\
N_\Delta &= 2\,N_l\,N_w = \frac{4\ l_{IA}\ w_{IA}\ \sqrt{3}}{3\ S^2}
\end{aligned}
\tag{5.1}
$$

From equation 5.1, it is seen that the number of triangles in the fixed nominal area are dependant on the cell size (S) and the dimensions of the fixed nominal area (l_{IA} and w_{IA}). Furthermore, from Figure 5.8, it is seen that for every triangle in width, there are two triangles in length, which is also taken into account in equation 5.1. With the mean load of a "Y" section known along with the number of triangles needed to fill a fixed nominal area, the scaled mean load of the model can be determined by multiplying these. Thus, to compare the model with the dynamic experiments from chapter 3, the model results are scaled with:

$$S = 3.2\text{mm};\ l_{IA} = w_{IA} = 42.5\text{mm} \Rightarrow N_\Delta = 407.36 \tag{5.2}$$

Thus, the scaled mean load is:

$$P_{m\Delta} = P_m\,N_\Delta = 1.82\,\text{kN} \tag{5.3}$$

Comparing this mean load to the experimental mean loads, i.e. $\mathbf{P_m}$ obtained in chapter 3, and repeated in Table 5.2, it is seen that the simulated mean load is approximately 49.5% of the largest experimental mean load and 61.85% of the smallest experimental mean load:

$$\frac{1.82\,\text{kN}}{3.69\,\text{kN}} \approx 49.3\% \quad \text{and} \quad \frac{1.82\,\text{kN}}{2.95\,\text{kN}} \approx 61.7\% \tag{5.4}$$

Frame rate [fps]	**Test** [-]	$\mathbf{v_{impact}}$ [m/s]	$\mathbf{R^2}$ [-]	$\mathbf{a_{mean}}$ [m/s^2]	$\mathbf{P_m}$ [kN]	$\varepsilon_\mathbf{d}$ [%]	**Energy** [J]
5,400	1	-8.26	0.9979	2709	3.68	68.70	50.59
	2	-8.12	0.9985	2718	3.69	69.84	51.60
	3	-7.99	0.9988	2296	3.12	78.66	49.09
10,000	1	-8.40	0.9985	2310	3.14	72.72	45.66
	2	-8.25	0.9987	2280	3.10	80.05	49.61
20,000	1	-7.98	0.9745	2332	3.17	67.38	42.71
	2	-7.82	0.9832	2169	2.95	75.26	44.37

Table 5.2: Results and data obtained from the analysis of the seven tests. Repeated from Table 3.1.

However, as mentioned in chapter 3, the only knowledge of the bulk material is that it is the aluminium 5052 alloy. The material parameters in Table 4.2 are taken from [Varmint Al, 2019] as aluminium 5052-o. Though, many different material parameters can be found for aluminium 5052-o. Therefore it is decided to try different material properties, which have been documented for the aluminium 5052 alloys.

The aluminium 5052-o alloy from [Varmint Al, 2019], has a yield stress of 59.76 MPa. This yield stress is relatively low for an aluminium 5052 alloy, since [Varmint Al, 2019] provides material models for aluminium 5052 alloys, which has yield stresses ranging up to 250 MPa. Furthermore, [MatWeb, 2020] suggests that aluminium 5052-o has a yield stress of 89.6 MPa. Thus, the second material model, Mat model 2, is made using equation 5.5 and 5.6 to determine a fitting strength coefficient to obtain a yield stress of 89 MPa while keeping the same hardening exponent of $n = 0.25$.

$$\varepsilon_y = \frac{\sigma_y}{E} \approx 1.27\text{E-3} \tag{5.5}$$

$$\varepsilon_y = \left(\frac{E}{k}\right)^{\left(\frac{1}{n-1}\right)} \Rightarrow k \approx 472\text{MPa} \tag{5.6}$$

This material model also show insufficiently mean load, as it is seen in Table 5.4. Thus, another material model is tried.

Mat model 3, is made from a set of material parameters, found in [Min et al., 2011]. [Min et al., 2011] uses tensile tests of aluminium 5052 to determine material parameters for their model regarding prediction of Forming Limit Stress Diagrams. And the material parameters are: $\sigma_y = 82\,\text{MPa}, E = 75\,\text{GPa}$, $k = 424\,\text{MPa}$, $n = 0.28$. For Material Type 18 in LS-DYNA a yield stress can be specified. When specifying a yield strength a yield strain is calculated as:

$$\varepsilon_y = \left(\frac{\sigma_y}{k}\right)^{\left(\frac{1}{n}\right)} = 2.83\text{E-3} \tag{5.7}$$

This material model also show insufficiently mean load, as it is seen in Table 5.4. Thus, a final material model is tried.

Mat model 4 is found by examining the stress-strain curves of the previous material models. The stress-strain curves for the different material models are seen in Figure 5.9:

The strength coefficient, k, determines the strength of the material, i.e. an increase in k, increases the yield stress and the entire curve is shifted upwards along the stress coordinate. This increase is seen in the difference between the stress-strain curves for Mat model 1 and Mat model 2. The hardening exponent, n, determines the slope of the stress-strain curve after yielding, i.e. if $n = 0$ the material behaves elastic-perfect-plastic. This effect on the slope of the stress-strain curves after yielding is seen between the stress-strain curves for Mat model 2 and Mat model 4. Thus, by lowering n and increasing k, the work needed to deform the material increases, while also increasing the yield strain, as seen in equation 5.6.

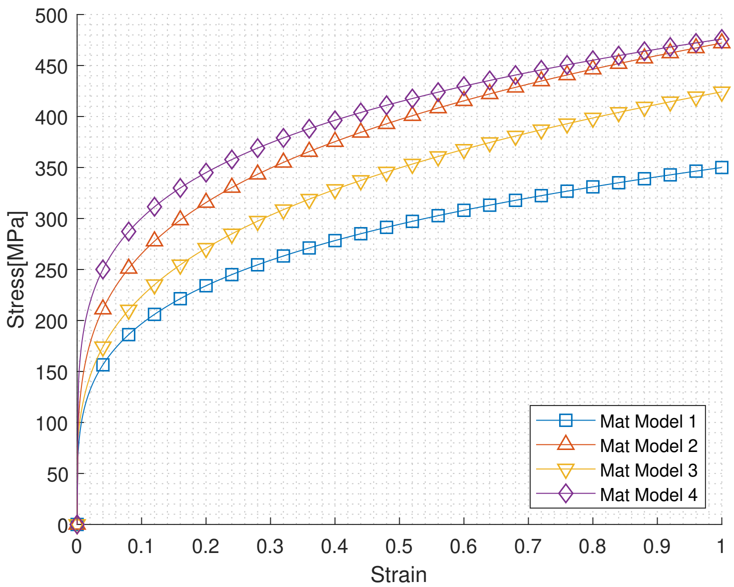

Figure 5.9: Stress-strain curves of material models.

Material model	σ_y [MPa]	E [GPa]	n [-]	k [MPa]	ν [-]	ε_y [-]
Mat model 1	59.76	70.32	0.25	350	0.33	8.50E-4
Mat model 2	89.00	70.32	0.25	472	0.33	1.27E-3
Mat model 3	82.00	75.00	0.28	424	0.33	2.83E-3
Mat model 4	**136.50**	**70.32**	**0.20**	**476**	**0.33**	**1.94E-3**

Table 5.3: Material models.

The results of the simulations made with these four different material models are seen in Table 5.4, where the mean load of each "Y" section is determined and scaled with the scaling factor given in equation 5.2. Furthermore, the deviation from the maximum and minimum experimental load, from Table 5.2, is also tabulated in Table 5.4, along with the deviation from the mean load determined with the crushing strength from the data sheet of the honeycomb, given in equation 5.8.

$$(42.5\text{mm} \cdot 42.5\text{mm}) \cdot 1.76\text{MPa} \approx 3.18\text{kN} \tag{5.8}$$

Material model	**Mat model 1**	**Mat model 2**	**Mat model 3**	**Mat model 4**
Scaled mean load	1.82 kN	2.56 kN	2.29 kN	2.91 kN
Dev. from max P_m	-50.7%	-30.6%	-37.9%	-21.1%
Dev. from min P_m	-38.3%	-13.2%	-22.4%	-1.4%
Dev. from data sheet	-42.8%	-19.5%	-28.0%	-8.5%

Table 5.4: Scaled mean load of the four different material models, where the deviation from the minimum and maximum mean loads obtained from the dynamic experiments is tabulated, as well as the deviation from the theoretical mean load.

With Mat model 4, the deviation is -1.4% for the minimum mean load obtained in the experiments and -21.1% for the maximum. However, as stated in chapter 3, there is an uncertainty regarding the precise dimensions of the test samples, which means that the dimensions of the test samples are not precisely 42.5 mm × 42.5 mm. Therefore, the maximum mean load in the experiments may be for a test sample with a larger nominal area and, while the minimum mean load is for a test sample with a smaller nominal area. With these uncertainties, it is determined to base the evaluation of the material models primarily on the mean load predicted with the data sheet. By using the data sheet, it is ensured that the nominal area used to determine the scaling factor and the predicted mean load is the same. The deviation between the scaled mean load from the simulation and the predicted mean load from the data sheet is -8.5%. Further fitting of the material parameters in the model could result in a better correlation between the simulation and data sheet. However, since the exact material parameters for the aluminium used in the honeycomb is unknown, it could also provide wrong material data.

Furthermore, as stated earlier, the basis for the comparison is a weak formulation. Thereby, a wrong material model in the simulation could provide a mean load which fits the mean load of the experiments perfectly, while having a force-displacement curve which does not resemble the honeycombs. Thus, the next step would be tensile testing of the bulk material to determine more accurate material parameters. However, given the circumstance with the lockdown, this is impossible — nor is it necessary, at least not before better experiments are conducted on the honeycomb.

The force-displacement curve for the simulation made with Mat model 4, is shown in Figure 5.10. From this force-displacement curve, the deformation still occurs as described in [Wierzbicki, 1983].

For these reasons, it is decided that the model with Mat model 4 appropriately simulates the deformation, force-displacement curve and mean load of a honeycomb made with aluminium 5052.

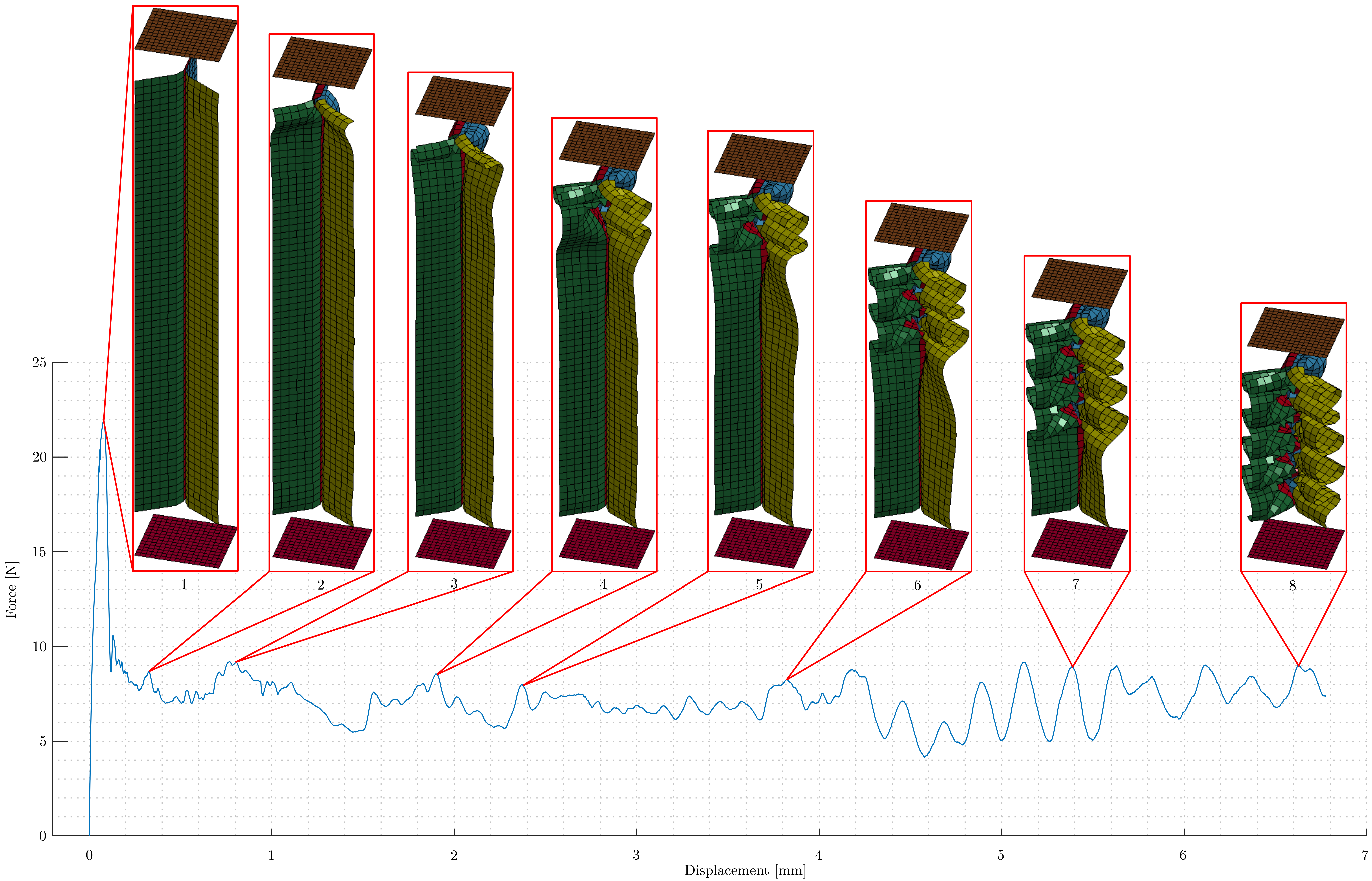

Figure 5.10: Force-displacement curve for the simulation made with Mat model 4.

5.1.2 Troubles of changing material parameters

When the material parameters were changed, during the implementation of the different material models, it caused the model to be unstable. The instability was most likely a contact instability, which caused zero-energy modes in most elements, as seen in Figure 5.11.

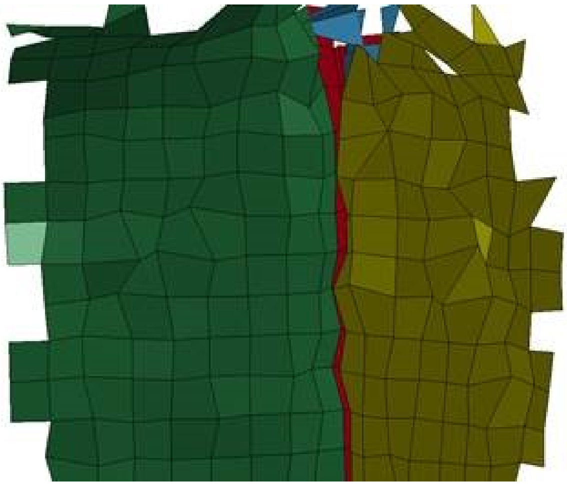

Figure 5.11: Zero energy modes model.

It was found that the problem occurred due to an element erosion option in the *MAT_POWER_LAW_PLASTICITY keyword. The erosion is based on a maximum plastic strain, i.e. if an element strain more than a limit value, it is deleted from the simulation. To ensure none of the elements was deleted in the simulation, this limit value was set to ten. Thereby none of the elements would be deleted unless there was a severe problem with the simulation. However, this option apparently caused instability in the simulation, and by removing the possibility of erosion entirely, i.e. setting the limit value to zero, the model became stable.

When examining the plastic strain in the model afterwards it was found that the plastic strain never comes near the limit of ten. In fact, the strain only exceeds one, as the densification begins.

5.2 Scalability

A larger model is developed with Mat model 4, to test the validity of the scaling of a simulation with one "Y" section. This larger model consists of seven full cells, as seen in Figure 5.12 i.e. 24 "Y" sections which means the mean load should be 24 times larger than the mean load of the simulation made with one "Y" section. Two models of seven cells have been developed — one without and one with symmetry conditions on the free cell walls. A comparison between the force-displacement curves of the two models is seen in Figure 5.13, while the force-displacement curve for the model without and with symmetry conditions are seen in Figure 5.14 and 5.15 respectively. When scaling the mean load for the two different models, equation 5.1 is divided by 24 such the scaling factor becomes:

$$N_\Delta = \frac{2\ N_l\ N_w}{24} = 16.97 \tag{5.9}$$

Which gives the mean load for the model without symmetry conditions to be $P_{m\Delta} = 2.76\,\mathrm{kN}$ and for the model with symmetry conditions to be $P_{m\Delta} = 2.78\,\mathrm{kN}$. Which means the scaled mean load is slightly smaller for the seven cell model compared to the "Y" section. Though, as it is seen in Figure 5.14, the structure collapses inwards to its centre as the deformation increases. This collapse is especially visible in picture 5 and 6 of Figure 5.14. Besides the structural collapse of the honeycomb, it is seen from these simulations, that the free cell walls do not have a significant influence on the mean load for the honeycomb with these dimensions, which is discussed in chapter 3.

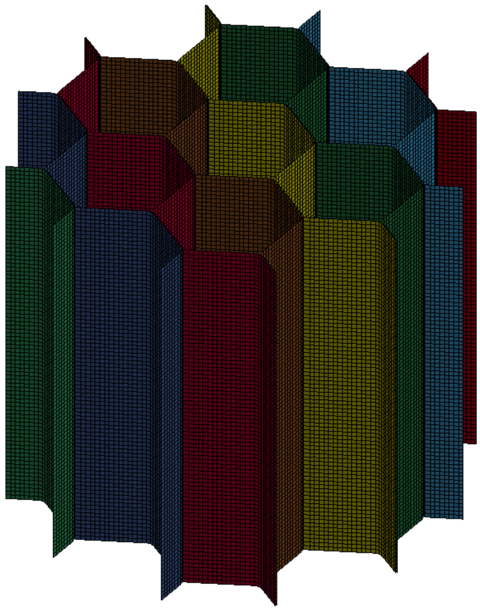

Figure 5.12: Model with seven cells. Each colour represents a sheet which is joint with an adhesive. The adhesive is modelled the same way as in section 4.5.

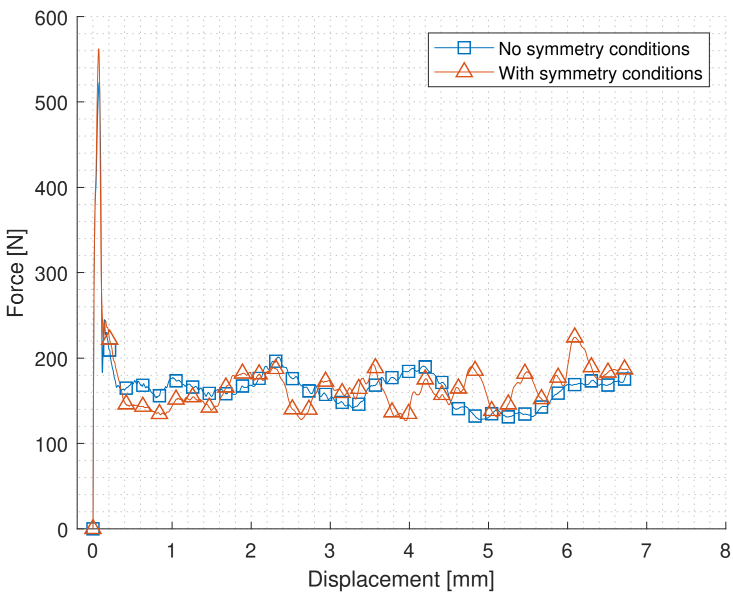

Figure 5.13: Force-displacement curves for the seven cell models

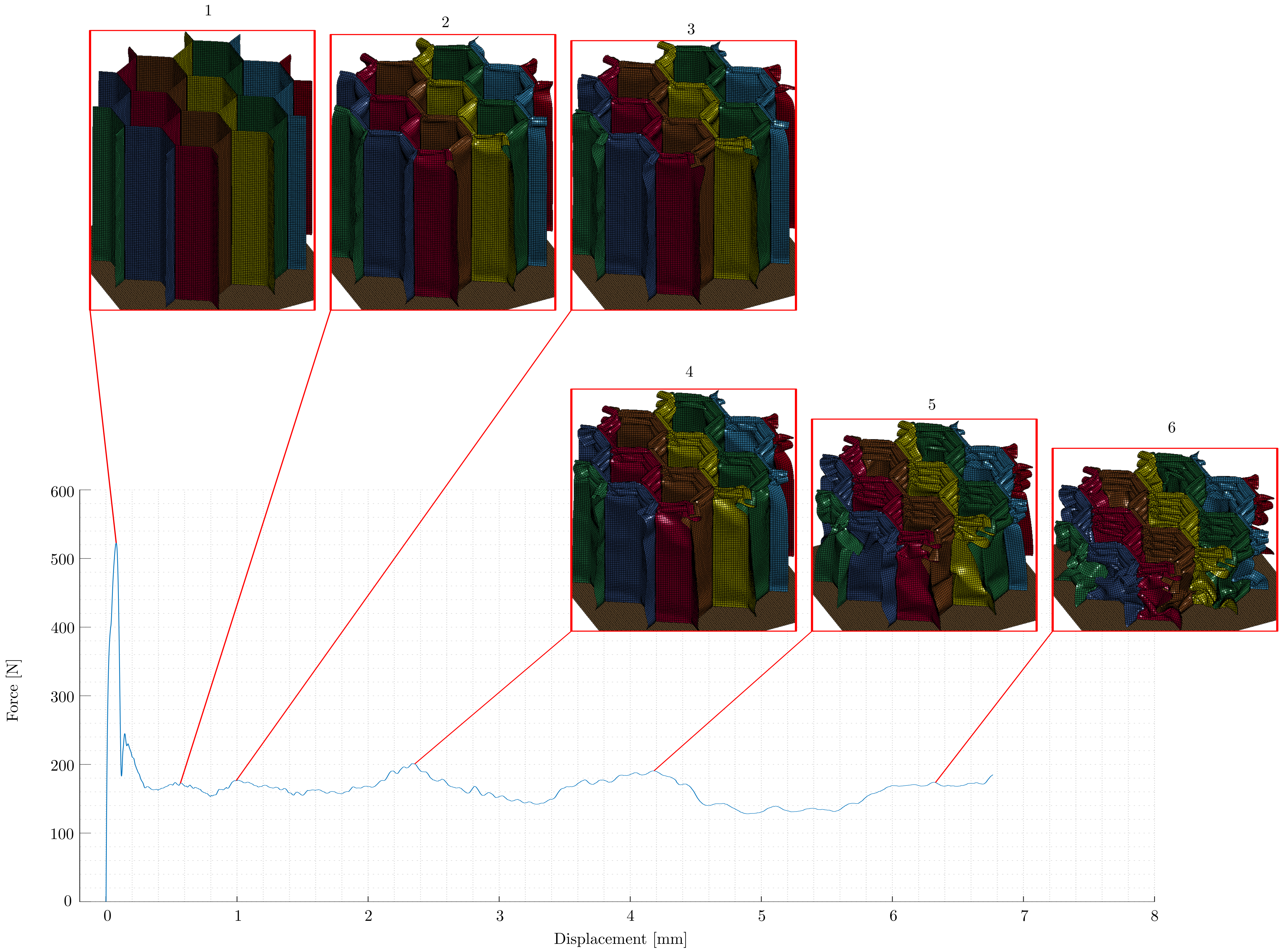

Figure 5.14: Force-displacement curve with Mat Model 4 without symmetry conditions.

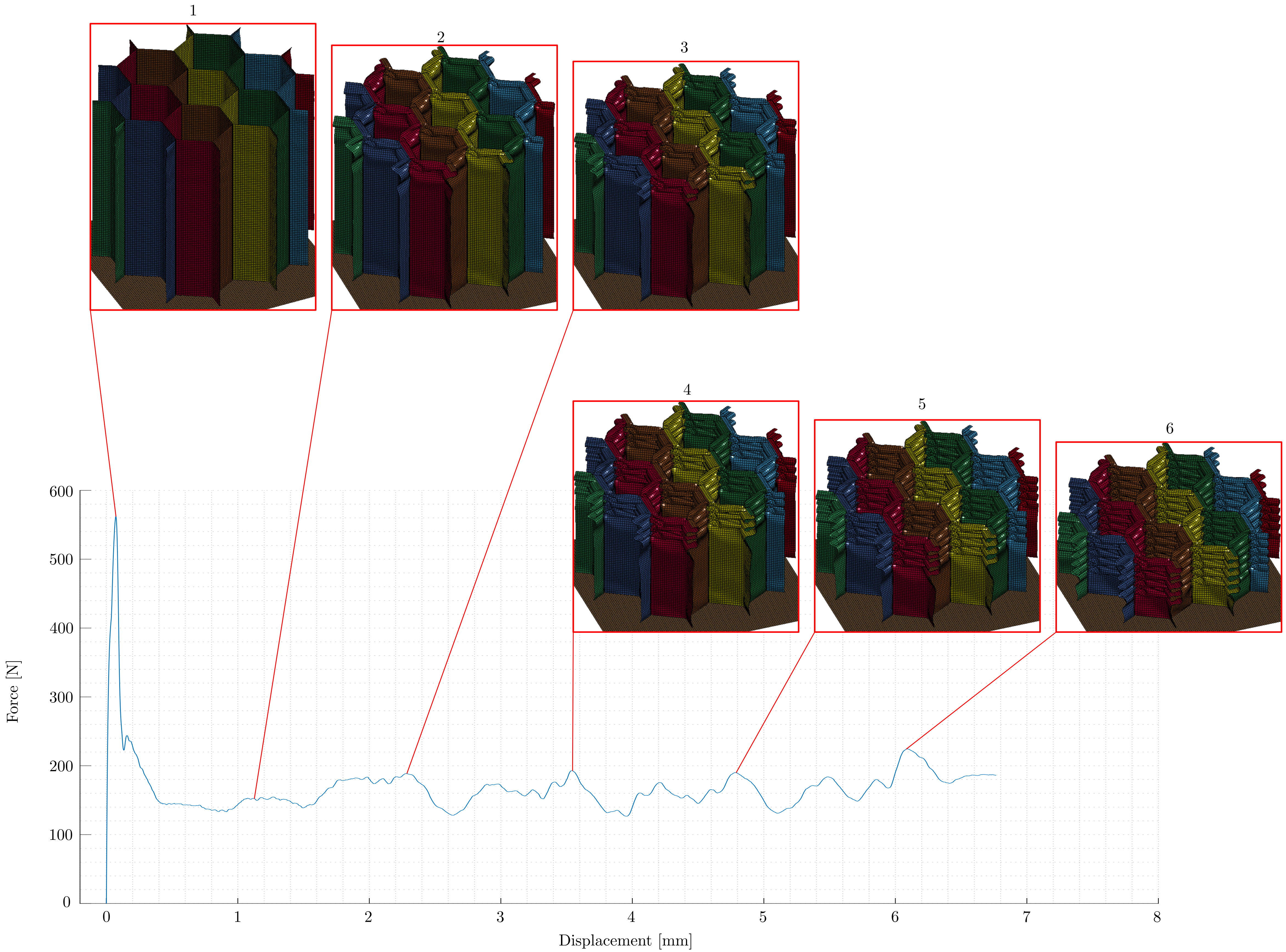

Figure 5.15: Force-displacement curve with Mat Model 4 with symmetry conditions.

When comparing the deformation between the model with symmetry conditions and the experiments, it is found that they are similar. These similar deformation modes are seen in Figure 5.16, where close-ups of the deformations are seen, where both deformations mostly follow the deformation mode described in [Wierzbicki, 1983].

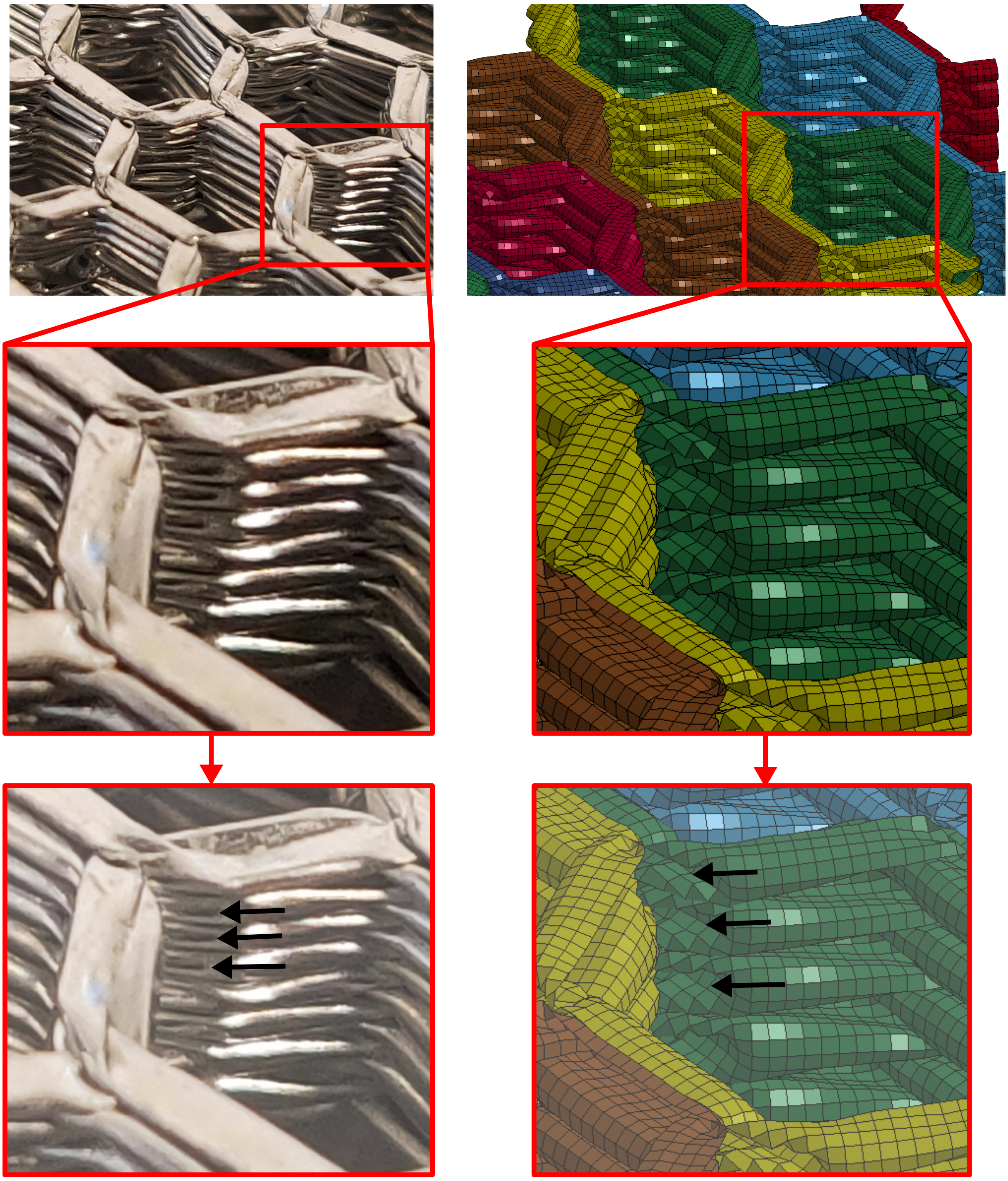

Figure 5.16: Comparison of deformation. The folds marked by the arrows indicate that the deformation occur as [Wierzbicki, 1983] proposes.

In Figure 5.16, it is seen that there are more folds in the experiment than there is in the simulation. This difference is mainly because the honeycomb in the model is modelled as 10 mm high before deformation. In contrast, the experimental test sample is 20 mm high, as it is explained in section 4.2.1. Furthermore, the honeycomb in Figure 5.16 is completely densified, whereas the simulated honeycomb is compressed to approximately 6.8 mm, where complete densification is not reached.

As stated in [Lund and Lindgaard, 2018] and [Cook et al., 2001], symmetry conditions must be used with care, especially when modelling dynamic and stability problems. This is because symmetry conditions can remove the possibility of some modes. In this project, symmetry conditions are applied both in-plane and out-of-plane, i.e. in-plane of the "Y" section and in the height of the models. By using the in-plane symmetry conditions, the possibility for the structure to collapse on itself is removed, as it is seen in Figure 5.17.

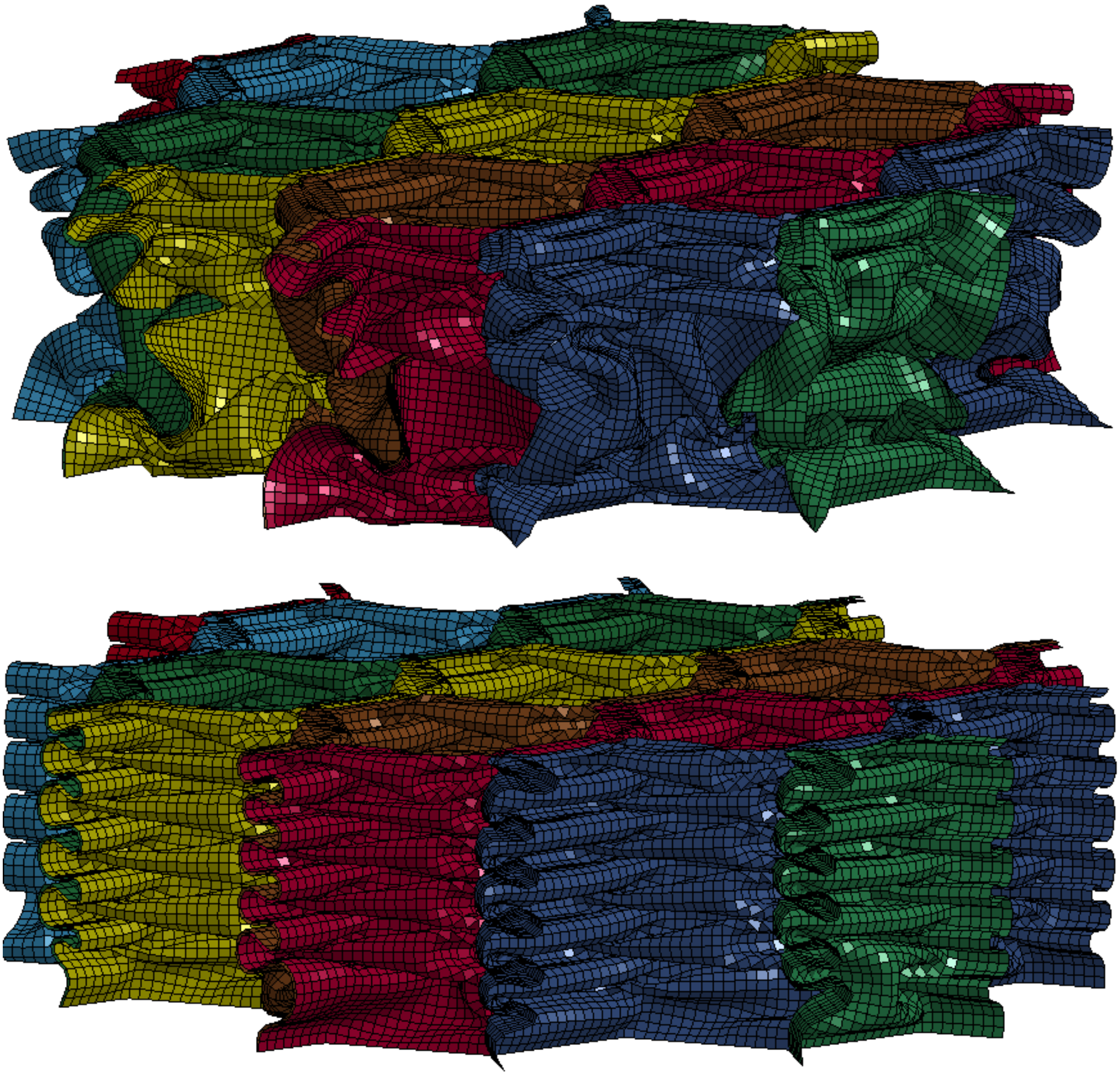

Figure 5.17: Buckling modes without (top) and with (bottom) in plane symmetry conditions.

However, as it is seen in Figure 5.18, the collapse occurs around the free cell wall edges of the honeycomb. Thus, the deformation mode with the symmetry conditions is the deformation mode which occurs most frequently. Therefore, it is determined that it is more representative to keep using symmetry conditions.

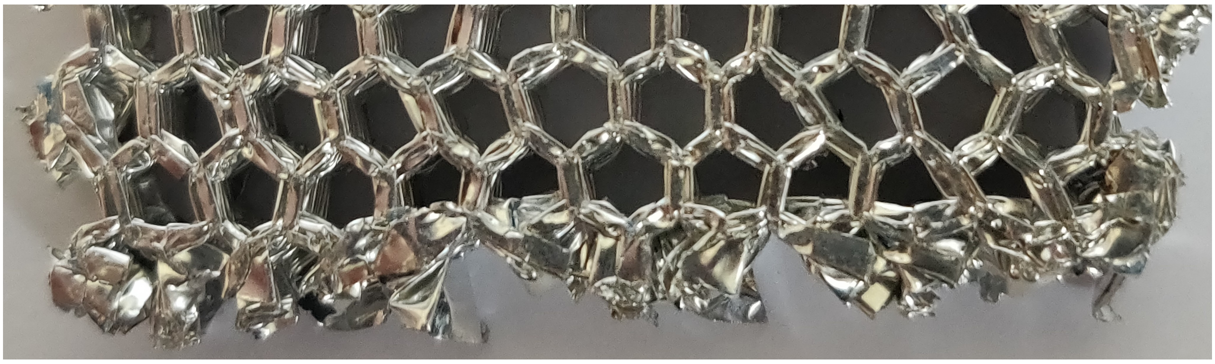

Figure 5.18: Collapsing effect on test sample. Only the cells closes to the edge are effected by the effect.

To find out whether or not the symmetry in the height is applicable a full model is needed because the stability is dependent on the in-plane dimensions of the honeycomb. However, to verify the full-scale model, experiments with larger honeycombs are needed. Considering the minimum dimensions of the impact attenuator, described in chapter 1, and the dimensions of the honeycomb test samples in the experiments:
Minimum impact attenuator dimensions:

$$w_{min} = 200\text{mm};\ l_{min} = 100\text{mm};\ h_{min} = 200\text{mm} \tag{5.10}$$

Test sample dimensions:

$$w = 42.5\text{mm};\ l = 42.5\text{mm};\ h = 20\text{mm} \tag{5.11}$$

It is seen that the height of the impact attenuator is at minimum ten times as high as the test samples. Thus, the collapsing effect could be significant for the design. However, such simulations and experiments are beyond the scope of this project.

Finally, when comparing the scaled mean loads of the seven cell model to the scaled mean load the "Y" section model, it is seen that the mean load deviates with:

$$1 - \frac{2.91\,\text{kN}}{278\,\text{kN}} = -4.68\% \tag{5.12}$$

This is considered a small enough deviation such the "Y" section can be used further on for the optimisation.

5.3 Final remarks

In this section, a few final remarks regarding the adhesive bond and the simulation time is made.

5.3.1 Adhesive bond

After finishing the model a question arises: Is it worth the trouble to simulate the adhesive bond? To answer this question the model is altered such the deformation follows that of the left of Figure 5.19 i.e. the deformation as if the joints in the honeycomb are firm. The model is developed such the two adjacent walls are one wall with double thickness. Otherwise, the model has the same parameters as the final model in section 5.1, which is shown on Figure 5.10. The force-displacement curves for the two models are shown on Figure 5.20. Further, the force-displacement curve of the simulation with double wall thickness is shown on Figure 5.21 with the deformation.

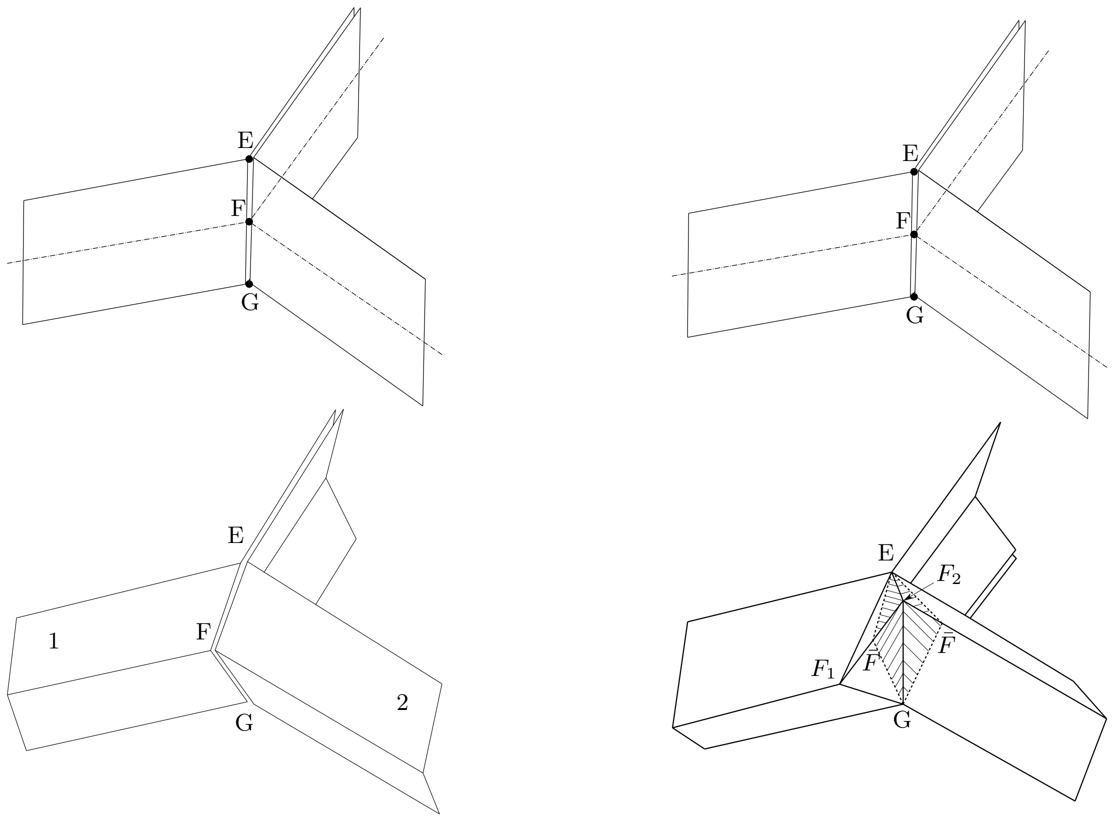

Figure 5.19: Joint before and after deformation. *Left:* Firm joint where the cell walls remains coincident at points E, G, and F. *Right:* Bonded joint where the cell walls remains coincident at points E and G. However at point F the cell walls splits such F becomes F_1 and F_2. The marked areas constructed with $\bar{F}$ are four identical triangles which represents the area where the adhesive bond is broken. Modified from [Wierzbicki, 1983] and repeated from Figure 4.6.

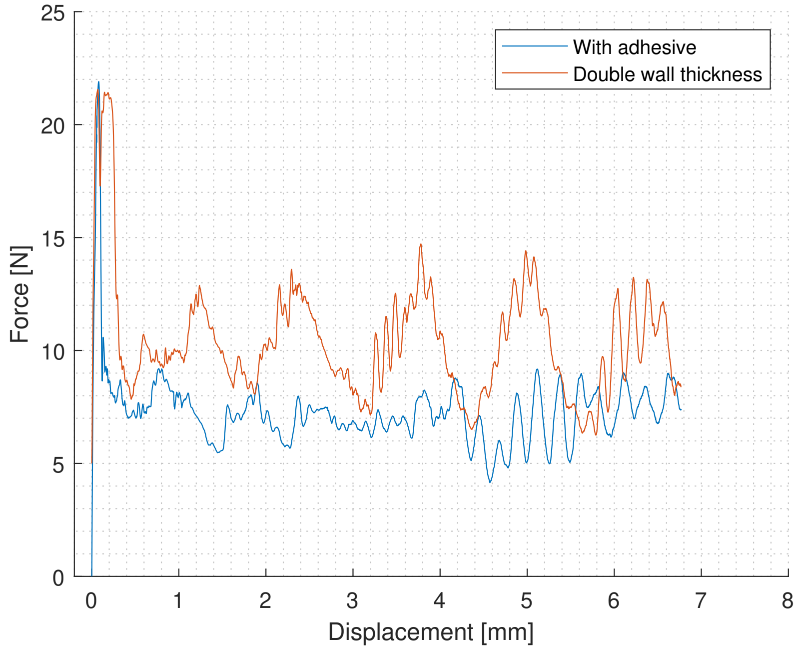

Figure 5.20: Force-displacement curves for the "Y" section with adhesive bond and double wall thickness.

The deformation of this simulation is similar to the simulation with the firm joint as in section 4.4.1, i.e. the deformation shown in the left of Figure 5.19. This deformation mode is hypothesised in [Wierzbicki, 1983] to require more energy to deform, than a deformation mode which partially breaks in the adhesive. These simulations support this hypothesis, where the comparison between the two model's force-displacement curves are seen in Figure 5.20. From these force-displacement curves, it is seen that the model with double-wall thickness has a larger mean load, while also having a larger difference between its peaks and valleys. The scaled mean load, for the model with double-wall thickness, is found to be $P_{m\Delta} = 4.13\,\text{kN}$, whereas the model in section 5.1, has a scaled mean load of $P_{m\Delta} = 2.91\,\text{kN}$, which means that the mean load is 41.9% larger if the adhesive is not taken into account.

$$\frac{4.13\,\text{kN}}{2.91\,\text{kN}} - 1 = 41.9\% \tag{5.13}$$

Based on this, it is needed to take the adhesive into account. Such the simulation does not overestimate the energy absorbed by the honeycomb.

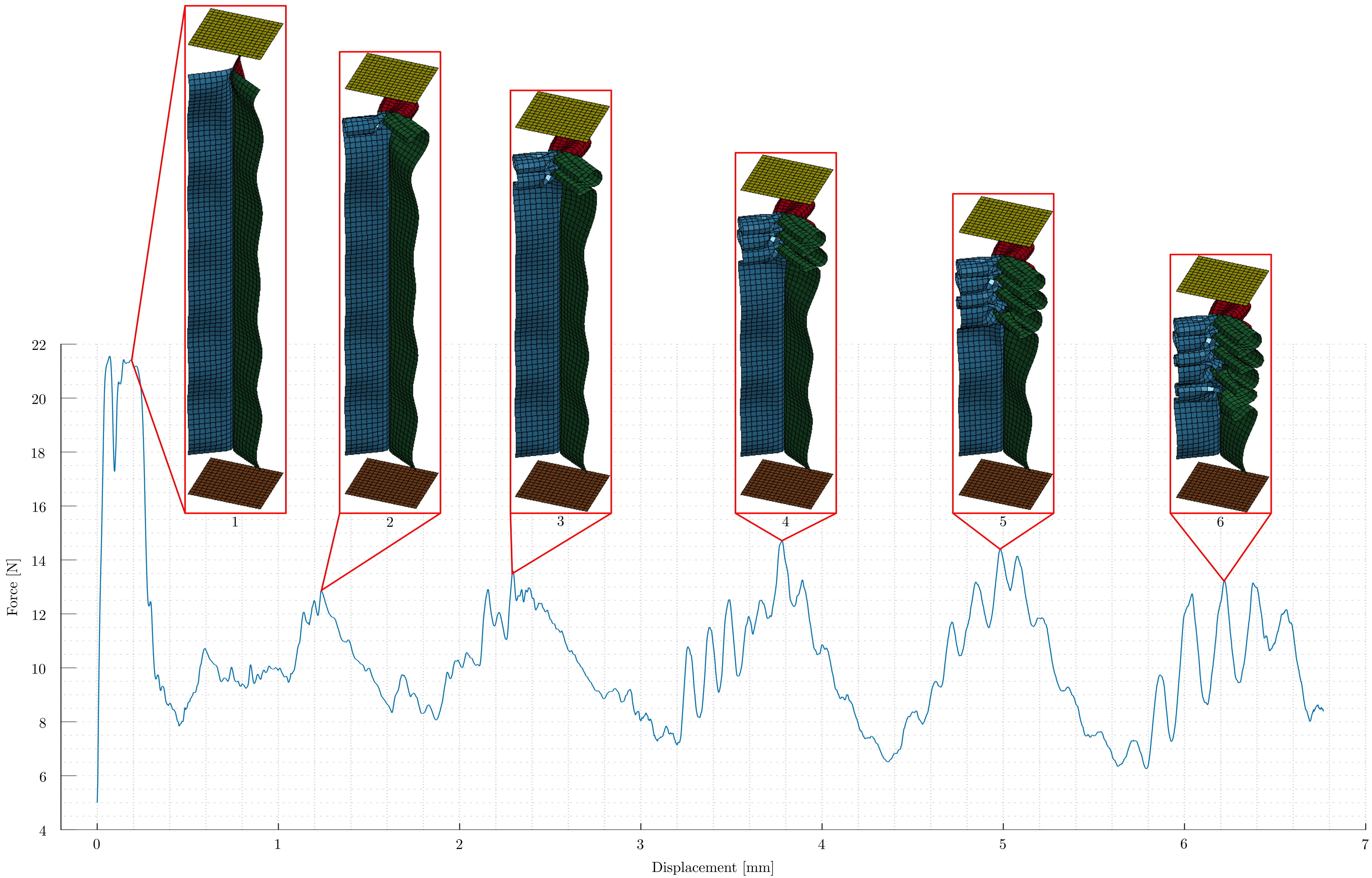

Figure 5.21: Force-displacement curve with Mat model 4 with symmetry conditions.

5.3.2 Cell size, wall thickness, and element length

In section 4.1.2, the problem with the element length/wall thickness ratio is introduced. The problem is that: For a constant thickness, the more the element length is decreased, the worse the kinematic assumptions of the element formulations becomes. However, the larger the element length becomes, the worse is the discretisation becomes.

[Gibson and Ashby, 1997] states that the length of a fold, λ, is roughly equal to the length of the cell wall, l, e.g. for the honeycomb in the experiments:

$$\lambda \approx l = \frac{\sqrt{3}\ S}{3} \approx 1.8\text{mm} \tag{5.14}$$

This means that over a distance of 1.8 mm, the bending moment switches sign twice. Thus, in order to avoid elements which in one end has a large positive bending moment, and in the other end has a large negative bending moment, several elements are needed such the bending moment progressively changes sign. Therefore, an algorithm is implemented, to satisfy both of these problems, where a suitable element length based on the element length/thickness ratio and the cell wall length is calculated. This algorithm is illustrated in Figure 5.22.

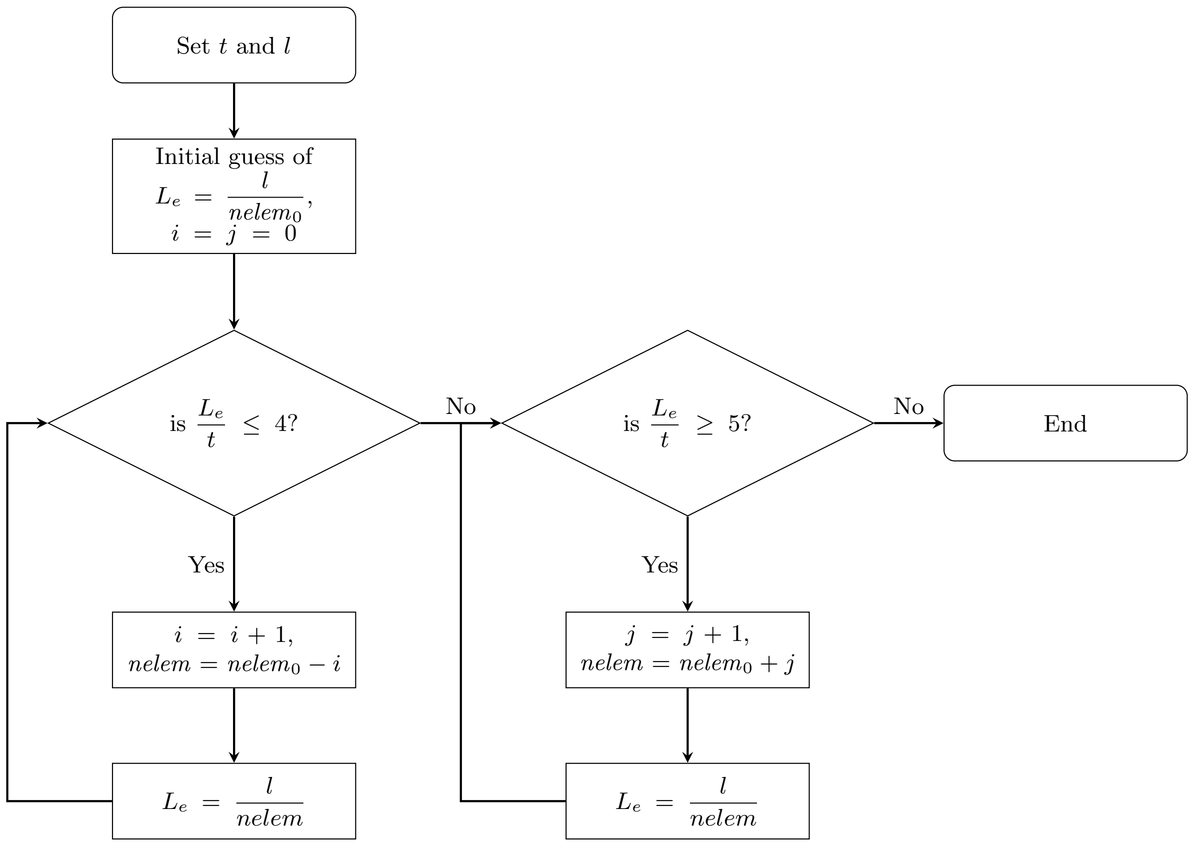

Figure 5.22: Flowchart of algorithm to determine suitable element length. $nelem$ is the number of elements along the wall length and $nelem_0$ the initial guess of $nelem$. In this project $nelem_0 = 20$.

By using this algorithm, it is found that 16 elements are needed to discretise one cell wall length, which gives an element length of 0.113 mm i.e.

$$L_e = \frac{1.8\text{mm}}{16} \approx 0.113\text{mm} \tag{5.15}$$

However, this is not a perfect method, and for some configurations of cell size and wall thickness, a satisfactory element length cannot be found. This problem is what sets the boundaries of this models applicability, i.e. for honeycombs with small cells and thick walls, the model becomes inapplicable. This problem is encountered in section 6.3.

5.3.3 Simulation time

In section 4.1.4 it is mentioned that it would be suitable to use mass scaling for a problem of this type. However, because of two reasons, the effect and consequences of applying mass scaling will not be thoroughly studied in this project.

The first reason is that the total CPU time of the final "Y" section model is 712 s (11 min and 52 s), which is fairly low when using multiple CPU's. In this project, 8 CPU's have been used, which means that the elapsed time is down to 92 s (1 min 32 s). Due to this low simulation time, it does not make sense to intentionally apply an error in the model to save time. Though, the seven cell model's total CPU time is 23,417 s (6 hr, 30 min, and 17 s) which gives an elapsed time of 3,277 s (54 min and 37 s) with 8 CPU's. If this had been the model to use in the optimisation, it would have made sense to apply mass scaling.

To test the effects mass scaling has on this problem, it has been applied to the seven cell model. The mass is scaled by a factor of 5, which decreases the CPU time to 6,990 s (1 hr, 56 min, and 30 s), i.e. the elapsed time is 881 s (14 min and 41 s) which is approximately 3.3 times faster. Note, the simulations are run on a remotely controlled computer, thus, when the simulation for the seven cell model is completed it takes approximately 1 hr and 30 min to download the D3PLOT files which is around 5 GB worth of data (Downloading goes through a VPN, which slows it down). The D3PLOT files are the main output files containing the history of the entire model. Thus, instead of needing 2 hr and 25 min without mass scaling, before the results of the simulation can be analysed, 1 hr and 45 min are needed, which still is an improvement, but it is only approximately 1.4 times faster.

However, as it is seen in Figure 5.23, the force-displacement curve is similar, but it is seen that the model with mass scaling has a larger difference between its peaks and valleys.. Further, the deformations do not change significantly — the only difference is that the folds are initiated in the opposite direction, which is random.

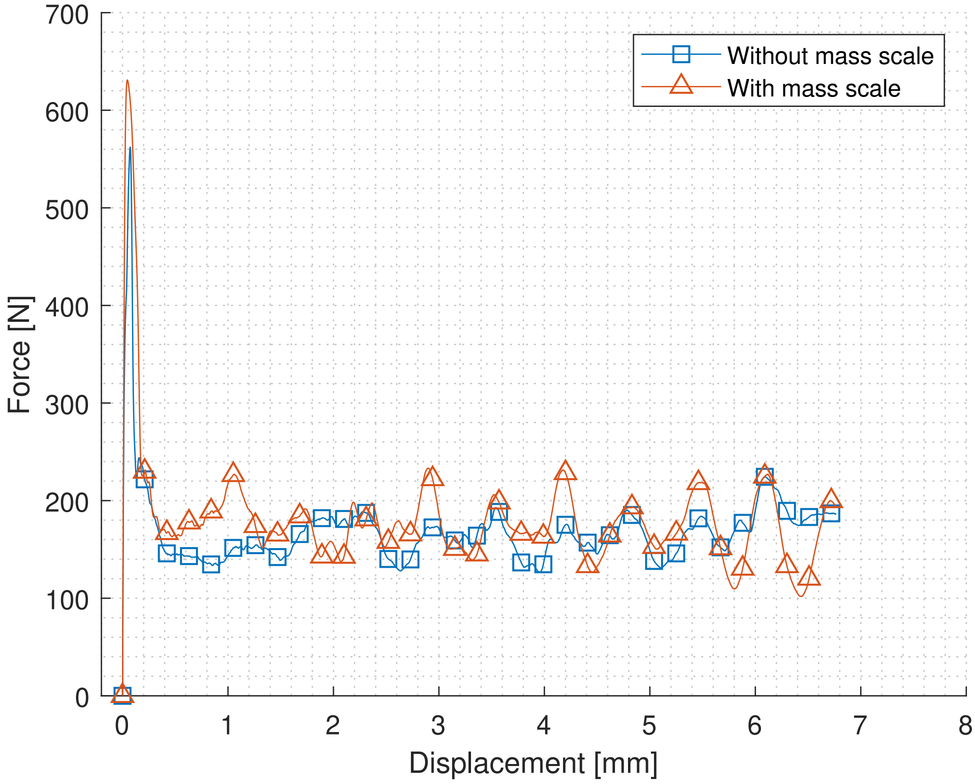

Figure 5.23: Force-displacement curves

The scaled mean loads are: $P_{m\Delta} = 2.95\text{kN}$ and $P_{m\Delta} = 2.78\text{kN}$ with and without mass scale, respectively. This means that a mass scaling of five would be applicable to this problem, which is the initial assessment of the problem. This also makes sense as the mass scaling affects the inertia forces, which are small compared to the internal forces. The inertia forces are small compared to the internal forces because the plates fields are quite small and undergo large plastic deformation.

5.4 Summary

In summary: A model of the deformation of an aluminium honeycomb has been developed such the deformation is consistent with [Wierzbicki, 1983] and experiments. The model is developed using a contact formulation in LS-DYNA which can simulate the adhesive bond used in the manufacturing of aluminium honeycombs. It is found that the model simulates the mean load to sufficient accuracy, when considering the lack of experimental data to verify further. Also, it is found that mass scaling is unnecessary to apply.

6 — Optimisation

In this chapter, the simulation model achieved in chapter 5 is used to develop a meta-model to see the influence of the design variables on the objective. Thus, an optimisation of this meta-model provides an optimised design of the impact attenuator. As part of the chapter "Further Work" in [Simonsen et al., 2019], the optimisation of a crash absorber was described. In this project, the objective is to minimise the mass of the impact attenuator assembly, rather than maximise the specific energy absorption. Though the objective is different, some of the initial considerations are still applicable. Thus, the relevant parts of the section "Optimisation" is repeated in appendix F. Further, the optimisation is subjected to the constraints given in section 1.2. Thus, when calculating the mass of the honeycomb as the four walls in the "Y" section, the optimisation problem can be expressed as:

$$\begin{cases} Minimise \quad f(S,\, t,\, h) = m_{IA} = 4\,\dfrac{l}{2}\,t\,\rho\,h\,N_{\Delta} = \dfrac{8\,l_{IA}\,w_{IA}\,\rho\,t\,h}{3S} \\ s.t. \qquad W\left(P_m,\, h\right) \geq 7350 \text{ J} \\ \qquad P_m\left(S,\, t\right) \leq 60 \text{ kN} \\ \qquad l_{IA} \geq 100 \text{ mm} \\ \qquad w_{IA} \geq 200 \text{ mm} \\ \qquad 200 \text{ mm} \leq h \leq 357\text{mm} \end{cases} \tag{6.1}$$

The requirement regarding peak load is removed, since precrushed honeycombs are intended for the impact attenuator, and therefore no peak load is achieved. Before doing the simulation based optimisation, a preliminary investigation of commercially available honeycombs is conducted to see what can be obtained without the simulation model. Afterwards, the design variables of the optimisation is described, followed by the steps of the optimisation and a description of the applied method.

6.1 Data sheet optimisation

Before making an optimisation algorithm based on the model in chapter 5, a preliminary optimised impact attenuator is designed. This preliminary optimisation is based on the mean stress and density of commercially available honeycombs, with the constraints of equation 6.12. All material properties in the following are based on data sheet information of available honeycombs and not experimental or simulation results obtained in this project.

As stated in Chapter 1, the current impact attenuator's mass is only 20 % of total mass. Thus, by reducing the in-plane dimensions to their minimum values, $w = 200$mm and $l = 100$mm the mass of the front bulk head and the anti intrusion plate is reduced to:

$$m_{FBH} + m_{AIP} = 0.88\text{kg} \tag{6.2}$$

rather than 2.72 kg. Thus, an impact attenuator is designed with the minimum allowable dimensions. The minimum required displacement at densification should be 122.5 mm, with a mean load of 60 kN, to obtain the required energy absorption:

$$60\,\mathrm{kN} \cdot 122.5\,\mathrm{mm} = 7350\,\mathrm{J} \tag{6.3}$$

Assuming a densification strain of 0.7 the height of the impact attenuator is 175 mm. Since this does not satisfy the constraints, the minimum height of 200 mm is used. This gives a displacement of 140 mm at densification, resulting in a mean load of 52.5 kN to achieve an energy absorption of 7350 J.

$$\frac{7350\,\mathrm{J}}{140\,\mathrm{mm}} = 52.5\,\mathrm{kN} \tag{6.4}$$

Based on the minimum dimensions of the impact attenuator, the minimum mean stress of the honeycomb is determined.

$$\frac{52.5\,\mathrm{kN}}{(100\,\mathrm{mm} \cdot 200\,\mathrm{mm})} = 2.625\,\mathrm{MPa} \tag{6.5}$$

and the maximum

$$\frac{60\,\mathrm{kN}}{(100\,\mathrm{mm} \cdot 200\,\mathrm{mm})} = 3.0\,\mathrm{MPa} \tag{6.6}$$

As the data sheets provides a density, the optimisation problem can be expressed as:

$$\begin{cases} Minimise \quad f(\rho) = m_{IA} = l_{IA}\, w_{IA}\, h\, \rho \\ \\ s.t. \qquad W\left(P_m\right) \geq 7350 \text{ J} \\ \qquad 52.5\,\mathrm{kN} \leq P_m\left(\sigma_m\right) \leq 60 \text{ kN} \\ \qquad l_{IA} = 100 \text{ mm} \\ \qquad w_{IA} = 200 \text{ mm} \\ \qquad h = 200\,\mathrm{mm} \end{cases} \tag{6.7}$$

With this, 35 honeycomb configurations from [Plascore, 2020] and [Easycomposites] are investigated. One of the available honeycombs has a mean stress of 2.62 MPa and properties given in Table 6.1. With a mean stress of 2.62 MPa, the impact attenuator can be made with the minimum length and width, whereas the height has to be increased to 200.5 mm, due to the slightly lower mean stress and the assumption of 0.7 densification strain. With these dimensions and the density of the honeycomb in Table 6.1, the mass of the impact attenuator is,

$$(100\,\mathrm{mm} \cdot 200\,\mathrm{mm} \cdot 200.5\,\mathrm{mm}) \cdot 91.3\,\mathrm{kg/m^3} = 366.1\,\mathrm{g} \tag{6.8}$$

which is a mass reduction of 334 g i.e. a reduction of

$$\frac{334\mathrm{g}}{700\mathrm{g}} = 48\% \tag{6.9}$$

from the standard impact attenuator, which has a mass of 700 g. Since the outer dimensions of the front bulkhead and anti intrusion plate is decreased, the total mass of the impact attenuator, front bulkhead and anti intrusion plate is decreased to 1.25 kg, giving a mass reduction of 2.17 kg i.e.

$$\frac{2.17\,\mathrm{kg}}{3.42\,\mathrm{kg}} = 63\% \tag{6.10}$$

of the original mass. Simulations of the front bulkhead and anti intrusion plate with smaller outer dimensions are carried out in appendix G.

In the calculations, it is assumed that the mean load is reached immediately, which is a fair approximation, since the densification strain is set to the minimum expected. Also, the peak load is not accounted, since the honeycombs from [Plascore, 2020] and [Easycomposites] are intended to be precrushed.

Density	**Cell size**	**Cell thickness**	**Mean stress**	**Aluminium alloy**
91.3 kg/m^3	4.76 mm	50.8 μm	2.62 MPa	5052

Table 6.1: Properties of the optimum honeycomb with fixed mean force and densification displacement [Plascore, 2020].

A different approach is to focus on the energy absorption of $W = 7350$J, without focusing on the minimum height. By doing so, a higher densification displacement is possible, and thereby a lower mean stress is required, which could result in a lighter impact attenuator. To investigate this, the mean loads of the 35 honeycomb configurations are calculated based on the minimum area of the impact attenuator and the mean stress. From this, the required height of the impact attenuator is calculated as

$$P_m = w_{min}\, l_{min}\, \sigma_m; \quad W = P_m\, \delta_d = 7350\,\text{J}; \quad \delta_d = h\, \varepsilon_d; \quad \Rightarrow h = \frac{W}{P_m\, \varepsilon_d} \tag{6.11}$$

Where P_m is the mean load, w_{min} and l_{min} the minimum width and length of the impact attenuator, σ_m the mean stress of the honeycombs W the work needed, δ_d the densification displacement, and ε_d is the densification strain, which is set to 0.7. As the height now is variable the optimisation problem is expressed as:

$$\begin{cases} Minimise \quad f(\rho,\, h) = m_{IA} = l_{IA}\, w_{IA}\, h\, \rho \\ \\ s.t. \qquad W\,(P_m,\, h) \geq 7350 \text{ J} \\ \qquad P_m\,(\sigma_m) \leq 60 \text{ kN} \\ \qquad l_{IA} = 100 \text{ mm} \\ \qquad w_{IA} = 200 \text{ mm} \\ \qquad 200\,\text{mm} \leq h \leq 357\,\text{mm} \end{cases} \tag{6.12}$$

The height and corresponding mass of the honeycomb configurations, which meet the required energy absorption and height constraints, are plotted in Figure 6.1.

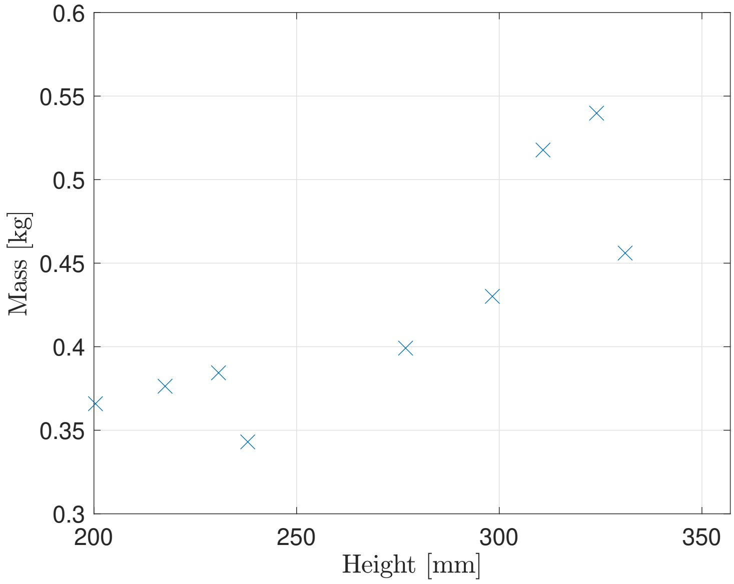

Figure 6.1: Plot of required height and corresponding mass to meet requirement of energy absorption within the height constraint of 200-357 mm.

The optimum based on this approach is different than the previous, as seen in Table 6.2, where the properties of the honeycomb are tabulated. The height of the impact attenuator is 238 mm, and the mass is 343 g, which gives a mass reduction of 357 g i.e.

$$\frac{357\,\text{g}}{700\text{g}} = 51\% \tag{6.13}$$

for the impact attenuator. The mass reduction of the front bulkhead, anti intrusion plate and impact attenuator is 2.2 kg i.e.

$$\frac{2.2\text{kg}}{3.42\text{kg}} = 64\% \tag{6.14}$$

The mean load is reduced to 44.13 kN.

Density	**Cell size**	**Cell thickness**	**Mean stress**	**Aluminium alloy**
72.1 kg/m^3	3.18 mm	25.4 μm	2.21 MPa	5056

Table 6.2: Properties of the optimum honeycomb without fixed values of mean force and densification displacement [Plascore, 2020].

These preliminary calculations serve as a guideline for what is possible for available honeycombs, and also shows that the minimum mass, might not be found with the minimum volume. It is important to note that the results in Table 6.2 are from a 5056 alloy, which generally has a larger mean stress. The influence of cell size and thickness is not investigated, which is the aim of the upcoming simulation based optimisation.

6.2 Optimisation set-up

Several aspects are considered to ensure a reliable optimisation procedure, where an overview of the procedure is seen in the flowchart in Figure 6.2. The steps in the flowchart are described in more detail in the following.

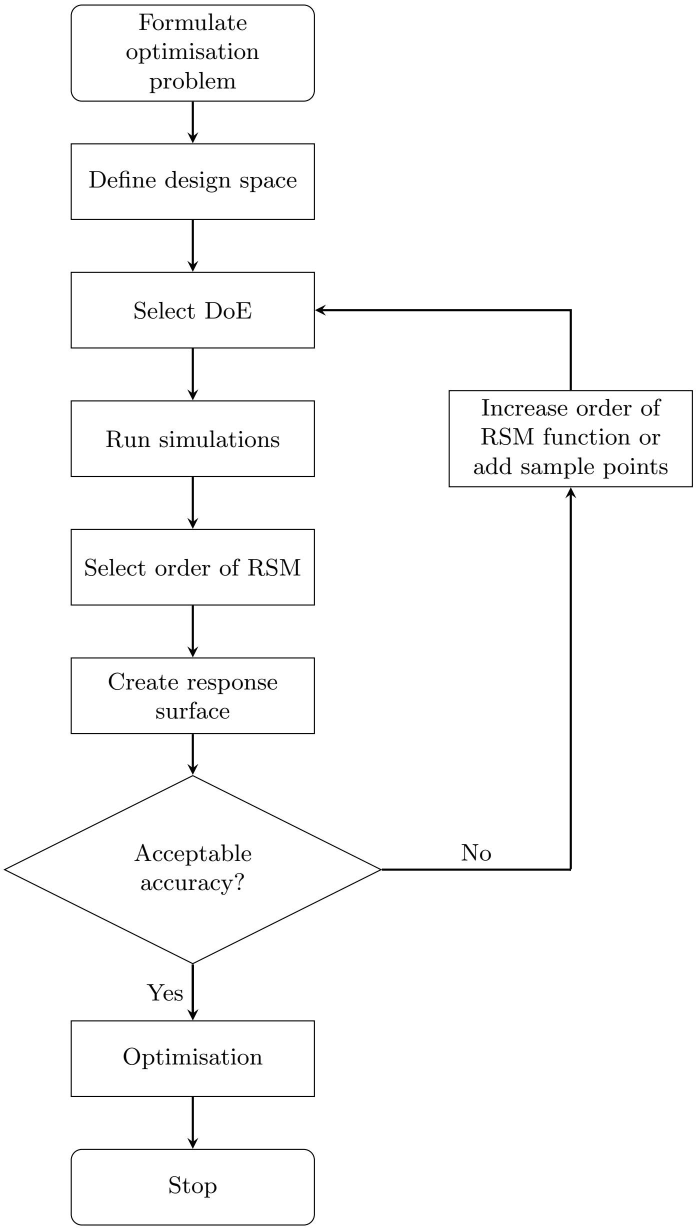

Figure 6.2: Flowchart of optimisation. RSM is short for Response Surface Method, and DoE is short for Design of Experiment. Both are elaborated in section 6.2.3 and 6.2.4, respectively.

6.2.1 Design variables

After formulating the optimisation problem, the design space is defined, starting with defining the design variables. Honeycombs are usually defined by their cell thickness and size. In addition to that, design variables of the outer dimensions, such as height, width, length and stacking of different honeycombs, are available. To limit the number of design variables, the observations gained in section 6.1 are used. In section 6.1 it is found that an impact attenuator with the minimum required area by [FSG, 2020], is a possibility with commercially available honeycombs. By having the minimum area, the minimum mass of the front bulkhead and anti intrusion plate is also achieved. Since these parts represent 80% of the total mass of the current impact attenuator assembly, the width and length of the impact attenuator is set to 200 and 100 mm, respectively.

Stacking of honeycombs with varying dimensions and properties, is not considered in this optimisation. This is because of the increasing complexity of the simulations as well as the increase in design variables, for each of the varying honeycombs. Furthermore, a plate is needed in between the stacked honeycombs to transfer the load between the honeycombs. This plate add mass to the impact attenuator, which needs to be compensated by the decrease in mass of the honeycombs.

With these considerations in mind, the remaining design variables are, cell thickness, cell size and height of the impact attenuator. For simplicity, the optimisation is done in the following two steps:

1. Optimise "Y" section of honeycomb in regards of cell thickness and cell length. Length, width and height of the impact attenuator is set to the minimum values — Two design variables.
2. Optimise "Y" section of honeycomb and the height of the impact attenuator. Length and width of the impact attenuator is set to the minimum values — Three design variables.

The definition of the cell thickness and size is shown in Figure 6.3.

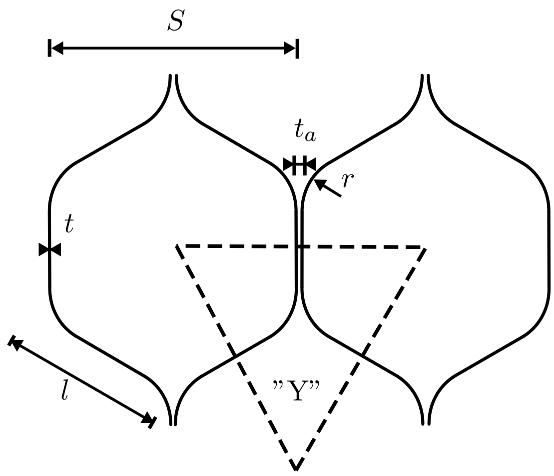

Figure 6.3: Definition of cell parameters, repeated from 5.1

6.2.2 Design space

With the design variables determined, the design space of the optimisation can be defined. The design space of the first optimisation run is limited by the cell thickness and cell size. The minimum and maximum of these are based on available honeycomb configurations from [Plascore, 2020] and [Easycomposites] and are as following:

$$\begin{gathered} 2\,\mathrm{mm} \leq S \leq 26\,\mathrm{mm} \\ 0.015\,\mathrm{mm} \leq t \leq 0.105\,\mathrm{mm} \end{gathered} \tag{6.15}$$

The interval for the third design variable, the height of the impact attenuator, is defined by [FSG, 2020] as:

$$200\,\mathrm{mm} \leq h \leq 357\,\mathrm{mm} \tag{6.16}$$

6.2.3 Response Surface Method

Since the optimisation is based on a FEM model, no explicit function of the design variables can express the mean load. Thus, a surrogate model or meta-model of the mean load is established. The meta-model is based on a polynomial fit to a number of simulations, with varying values of the design variables. Several methods can be used to obtain the meta-model, such as Radial Basis Functions (RBF), Kriging Method (KG) and Response Surface Method (RSM). It is chosen to use RSM due to its simplicity and since it is used in literature for this kind of problem, such as [Meng et al., 2014] and [Fazilati and Alisadeghi, 2016], where a good correlation between the simulation results and response surface is achieved. A more detailed description of RSM is found in appendix F together with the error evaluation of the method. Appendix F is a representation of the previous project [Simonsen et al., 2019].

Depending on the number of design variables and order of the response surface, a minimum number of sampling points are needed to avoid singularities, when determining the coefficients of the response surface function, e.g. a quartic function with two and three design variables requires 16 and 36 sampling points, respectively.

6.2.4 Design of Experiments

When applying RSM, it is important to have enough, and well distributed, sampling points to achieve a true and fair approximation, where the simulation time has a significant influence on the number of sampling points. In the following, it is chosen to do a full factorial design, since this will give a good representation of the objective in the entire design space. As described in section 5.3.3, the simulation time for the "Y" section quit low, meaning a full factorial DoE is suitable. If the simulation time was larger, techniques such as Central Composite Design or Latin hypercube could be applied, to reduce the amount of simulations needed.

6.2.5 Energy absorption of the impact attenuator

From the simulation of the "Y" section, a mean load is determined and scaled to the appropriate dimensions, as described in section 5.1.1. From this, a theoretical energy absorption is determined by multiplying the scaled mean load with an assumed deformation of the honeycomb, taken as 70% of the height, i.e. it is assumed that the densification strain is minimum 0.7. This densification strain, is determined based on the data sheets from [Plascore, 2020], results from the previous project [Simonsen et al., 2019] and the results from the experiments conducted in this project work.

Since the energy absorption is scaled with respect to the mean load, the constraints regarding the mean load and energy absorption are dependant on each other. This dependency narrows the feasible region in the first optimisations, since the height is constrained, whereby the mean load needs to be between 52.5 - 60 kN to ensure a sufficient energy absorption. Whereas the second optimisation has a larger feasible region, since the height of the impact attenuator is a design variable.

6.2.6 Optimisation algorithm

The choice of the optimisation algorithm depends on the problem, in regards of design variables, the number of objective functions and the nature of the objective function(s). Since the problem in this case is to minimise a multivariable function with non-linear constraints, the MATLAB algorithm "fmincon" is used. Within fmincon, several algorithm options are available. For this problem, the difference between the possible algorithm options in regards to computational time is not that pronounced, but sequential quadratic programming, SQP, is the fastest. The optimum point is the same for all options. Because of this SQP is chosen. The overall idea is illustrated by the flowchart in Figure 6.4.

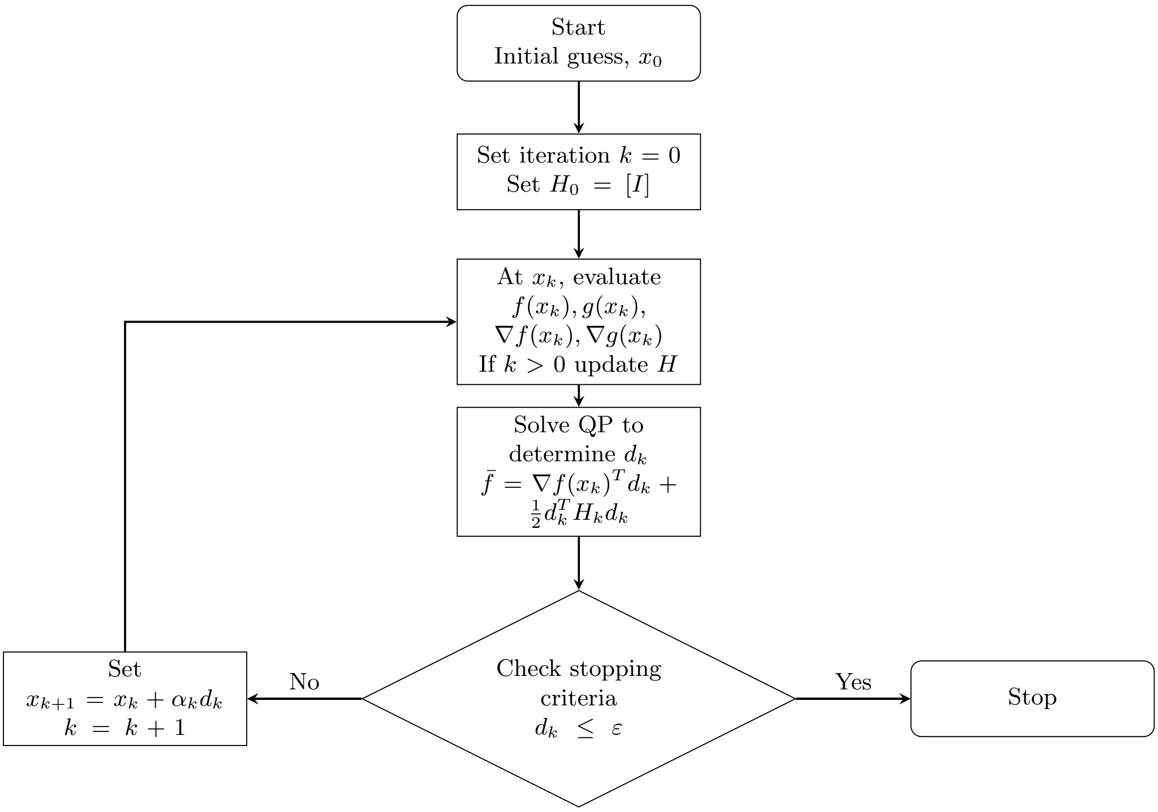

Figure 6.4: Flowchart of fmincon. [Arora, 2016], [Aji et al., 2018] and [MathWorks, 2020]

Where H is the Hessian of the Lagrangian function.

$$L(x,u) = f(x) + \sum_{k=1}^{m} u_k \, g_k(x) \tag{6.17}$$

As for many other optimisation algorithms, the minimum might not be the global one. If multiple local minimums are present, the one closest to the initial guess, x_0, is found. One way of securing finding the global minimum, is to use multiple starting points, and run the optimisation, collect function values and select the minimum of these. This is done by using the "MultiStart" algorithm provided by MATLAB, where a number of starting points are generated and the minimum function value is selected as the global minimum.

6.3 Optimisation 1

For the first optimisation, the following objective and constraints are used.

$$\begin{cases} Minimise \quad f(S,\, t,) = m_{IA} = \dfrac{8\, l_{IA}\, w_{IA}\, \rho\, t\, h}{3S} \\ \\ s.t. \qquad W\,(P_m) \geq 7350 \text{ J} \\ 52.5\,\text{kN} \leq P_m\,(\sigma_m) \leq 60 \text{ kN} \\ l_{IA} = 100 \text{ mm} \\ w_{IA} = 200 \text{ mm} \\ h = 200\,\text{mm} \\ 2 \text{ mm} \leq S \leq \; 26 \text{ mm} \\ 0.015 \text{ mm} \; \leq t \leq \; 0.105 \text{ mm} \end{cases} \tag{6.18}$$

Where S is the cell size, and t is the cell thickness. Before conducting numerous simulations for the entire design space, a preliminary study is made, where nine samples points are used. The sample points are tabulated in Table 6.3. The sample points are chosen as the minimum, the middle, and the maximum of both variables and are only used to give an indication of the area of interest. No results are available for sample no. 7, because the shell elements used in the simulation fails, due to the low cell size / thickness ratio.

Sampling no.	**Cell thickness, t** [mm]	**Cell size, S** [mm]	**Mass** [g]	$\boldsymbol{P_{m\Delta}}$ [kN]	W [kJ]
1	0.015	2	224.0	15.54	2.18
2	0.015	11	40.7	0.99	0.14
3	0.015	26	17.2	0.11	0.02
4	0.060	2	896.0	201.24	28.17
5	0.060	11	162.9	9.87	1.38
6	0.060	26	68.9	2.20	0.31
7	0.105	2	N/A	N/A	N/A
8	0.105	11	285.1	30.08	4.21
9	0.105	26	121.6	5.37	0.75

Table 6.3: Results from simulation with cell size and thickness as design variables.

With the results obtained from Table 6.3, it is possible to construct a response surface, but because of the low number of sample points, it is only possible to construct a quadratic function for the response surface. The response surface for the mean load and contour plot, with the constraints from equation 6.18, are shown in Figure 6.5.

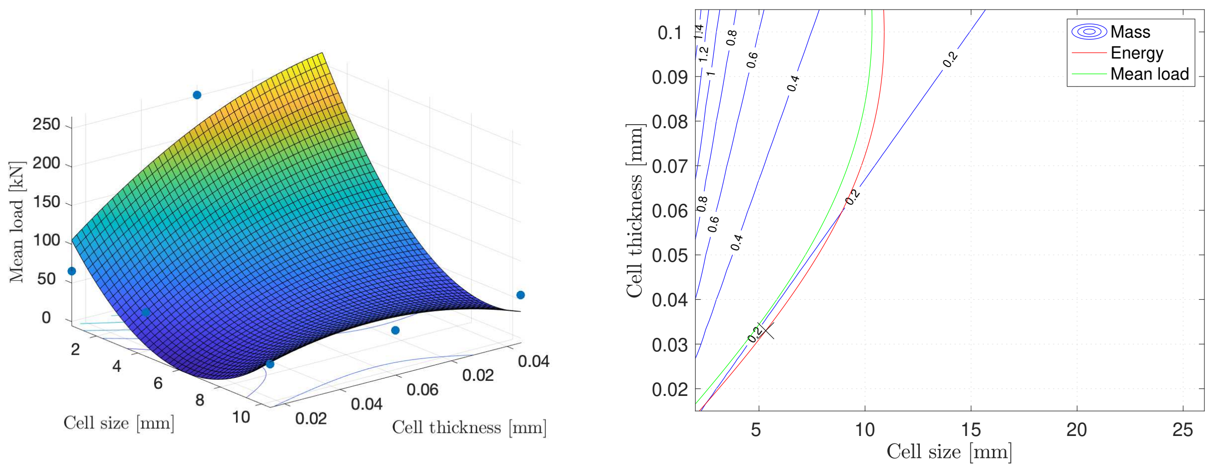

Figure 6.5: First iteration with two design variables and eight sampling points. *Left*: Response surface for the mean load with simulation data plotted as blue circles. *Right*: Contour plot of the objective function and the constrains. The feasible area is between the red and green curve and the optimum point is shown by the black cross.

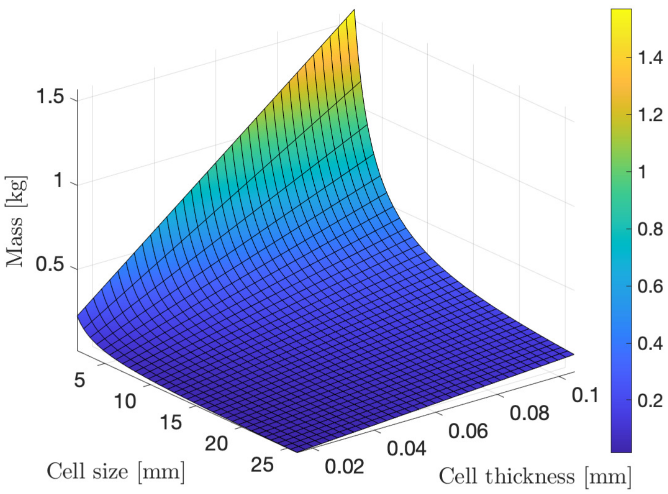

Figure 6.6: Surface plot of the mass obtained by the mass function giving in equation 6.18

As a consequence of the low numbers of sampling points, the values for the coefficient of determination, R^2, becomes 0.40 for the mean load function. This R^2 value indicates that the response surface is a poor fit of the sampling points, which is also seen on the left of Figure 6.5, where the sampling points are indicated with blue circles. Based on this, it is clear that more sampling points are needed to obtain a good fit of the response surface. However, this response surface still provides an indication of the area of interest, from which an optimum is found to be at:

$$S = 5.32\text{mm} \qquad t = 0.033\text{mm} \tag{6.19}$$

Based on the contour plot in Figure 6.5, the optimisation formulation is changed to.

$$\begin{cases} Minimise \quad f(S,\, t,\, h) = m_{IA} = \dfrac{8\, l_{IA}\, w_{IA}\, \rho\, t\, h}{3S} \\[2ex] s.t. \qquad\qquad W\,(P_m) \geq 7350 \text{ J} \\ \qquad 52.5\,\text{kN} \leq P_m\,(\sigma_m) \leq 60 \text{ kN} \\ \qquad l_{IA} = 100 \text{ mm} \\ \qquad w_{IA} = 200 \text{ mm} \\ \qquad h = 200\,\text{mm} \\ \qquad 2\text{mm} \;\leq\; S \leq\; 12\text{mm} \\ \qquad 0.015\text{mm} \;\leq\; t \leq\; 0.07\text{mm} \end{cases} \tag{6.20}$$

In this new design space, it is decided to expand the number of sampling points to 25. Thereby a relatively good fit should be ensured, since it is possible to make the response surface with a quartic function. The design variables are evenly distributed in these 25 sampling points, as shown in Table 6.4.

Sampling no.	**Cell thickness** [mm]	**Cell size** [mm]	**Mass** [g]	$\boldsymbol{P_{m\Delta}}$ [kN]	**Energy** [kJ]
1	0.015	2.0	224.0	15.54	2.18
2	0.015	4.5	99.6	3.94	0.55
3	0.015	7.0	64.0	2.01	0.28
4	0.015	9.5	47.2	1.16	0.16
5	0.015	12.0	37.3	0.78	0.11
6	0.029	2.0	433.1	52.54	7.36
7	0.029	4.5	192.5	11.90	1.67
8	0.029	7.0	123.7	6.12	0.86
9	0.029	9.5	91.2	3.30	0.46
10	0.029	12	72.2	2.22	0.31
11	0.043	2.0	642.1	113.12	15.84
12	0.043	4.5	285.4	24.85	3.48
13	0.043	7.0	183.5	11.39	1.59
14	0.043	9.5	135.2	6.78	0.95
15	0.043	12.0	107.0	5.18	0.73
16	0.056	2.0	836.3	178.48	24.99
17	0.056	4.5	371.7	40.00	5.60
18	0.056	7.0	238.9	17.14	2.40
19	0.056	9.5	176.1	10.71	1.50
20	0.056	12.0	139.4	6.90	0.97
21	0.070	2.0	1,045.3	272.65	38.17
22	0.070	4.5	464.6	58.30	8.16
23	0.070	7.0	298.7	26.61	3.72
24	0.070	9.5	220.1	15.39	2.15
25	0.070	12.0	174.2	10.27	1.44

Table 6.4: Results from simulation with cell size and thickness as design variables.

From the data in Table 6.4, it is possible to illustrate the influence of the design variables on the mass, energy absorption and mean load. The cell size and thickness influence on the mass and mean load are shown in Figure 6.7 and 6.8, respectively. Similar for the two plots, is that the influence of the mass and mean load is much more sensitive at small cell sizes (up to 4.5 mm), whereas the influence is less significant at larger cell sizes.

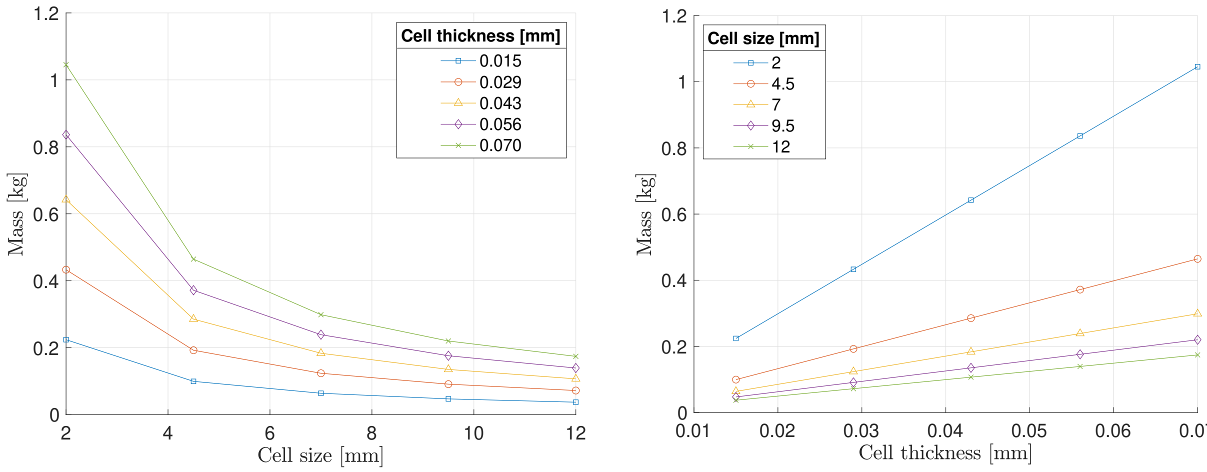

Figure 6.7: Influence of the design variables on the mass of the impact attenuator. The data is from Table 6.4

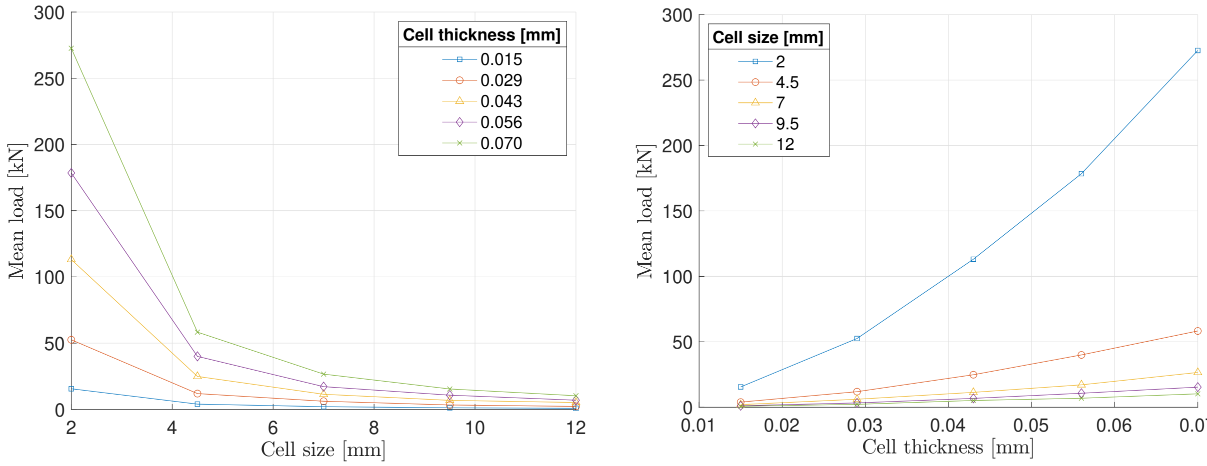

Figure 6.8: Influence of the design variables on the mean load of the impact attenuator. The data is from Table 6.4

With these 25 sampling points, a quadratic, cubic and quartic response surface is made and evaluated with their R^2 and R^2_{adj} values, see Table 6.5. In Table 6.5, it is seen that the R^2 value for the quadratic response surface of the objective function is increased significantly with the extra sampling points. However, it is the quartic function that fits the mean load function best and therefore the chosen order of the response surface. The quartic response surfaces for the mean load is plotted in Figure 6.9, together with the mass in the new design space. Since the energy absorption is a scaling of the mean load, the shape of the response surface and the values for the R^2 and R^2_{adj} values are identical.

	Mean load	
	R^2	R^2_{adj}
Quadratic	0.826	0.780
Cubic	0.984	0.975
Quartic	0.999	0.999

Table 6.5: Error evaluation of quadratic, cubic and quartic function for the response surface.

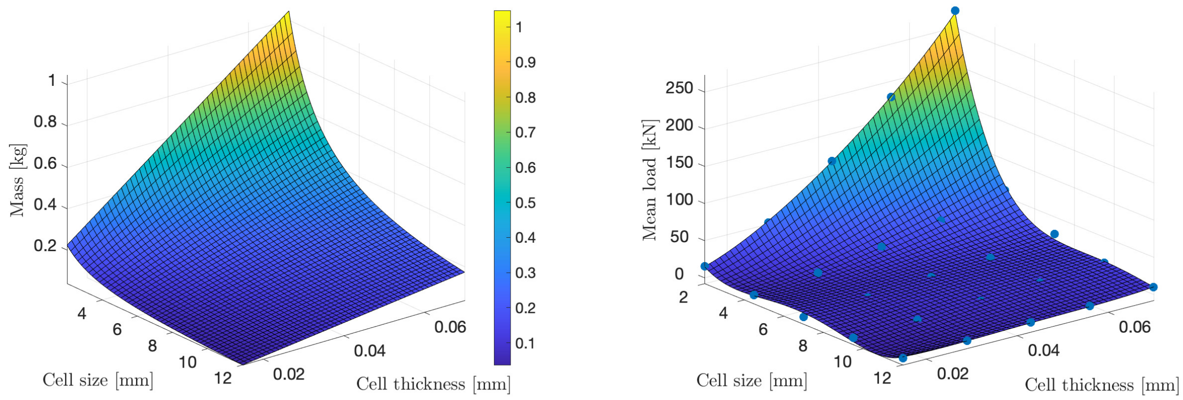

Figure 6.9: Response surfaces of the second iteration with two design variables and 25 sampling points (blue circles). *Left*: Objective function for the mass. *Right*: Mean load. The response surface for energy absorption is identical, since the energy absorption is scaled based on the mean load.

The shape of the response surfaces are as expected, where a rapid increase in the mass and mean load is seen in the corner with the largest cell thickness and smallest cell size. This response surface characteristic is also found in other researches work [Meng et al., 2014] and [Fazilati and Alisadeghi, 2016], which optimises a hexagonal honeycomb structure with respect to mass and energy absorption. The contour plot of the objective function and the constraint functions are plotted in Figure 6.10.

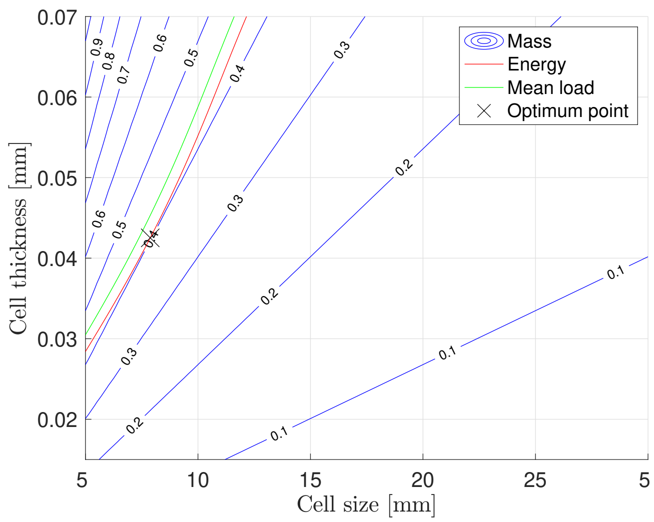

Figure 6.10: Contour plot of the objective function (blue), mean load constraint (green) and energy absorption constraint (red) for the second iteration with two design variables and 25 sampling points. The black cross represents the optimum point.

From the contour plot, it is seen that a feasible solution is found to the optimisation problem. By applying the optimisation algorithm to this problem, the optimum is found to be at:

$$S = 3.15\text{mm} \qquad t = 0.043\text{mm} \tag{6.21}$$

With this configuration of the honeycomb, the mass, energy absorption and mean load is 402.9 g, 7350 J and 52.5 kN, respectively. Which gives a mass reduction of 2.13 kg i.e.

$$\frac{2.13}{3.42} = 62\% \tag{6.22}$$

The values of the energy absorption and the mean load is as expected, since the found mean load is what is needed to achieve the minimum required energy absorption with the specified displacement. This optimisation is comparable to the first study of the data sheet optimum in section 6.1, where it is seen that the cell sizes and thickness are quite different for the two optimums. This results in different densities for the two, which are 100.7 kg/m^3 and 91.3 kg/m^3 for Optimisation 1 and data sheet optimisation, respectively. As stated in section 5.1.1, the simulation of the "Y" section underestimates the mean load required to deform the scaled honeycomb structure. Therefore, it is expected that the honeycomb configurations from the simulation requires less energy to deform, resulting in a denser honeycomb configuration than compared to the honeycomb configurations from the data sheet, to achieve a higher mean load. From Figure 6.10, it is observed that the mass of several configurations are more or less identical to the minimum. This means that a broader range of honeycomb configurations might be used for the impact attenuator, depending on available commercial honeycombs.

6.4 Optimisation 2

With the optimisation carried out for the two design variables, the height of the impact attenuator is added as a design variable. The reasoning behind this is to investigate whether a lighter impact attenuator might be achieved by decreasing the mean load and increase the densification displacement. For the second optimisation, the following objective and constraints are used.

$$\begin{cases} Minimise \quad f(S,\, t,\, h) = m_{IA} = \dfrac{8\, l_{IA}\, w_{IA}\, \rho\, t\, h}{3S} \\ \\ s.t. \qquad W\,(P_m) \geq 7350 \text{ J} \\ \qquad\qquad P_m\,(\sigma_m) \leq 60 \text{ kN} \\ \qquad\qquad l_{IA} = 100 \text{ mm} \\ \qquad\qquad w_{IA} = 200 \text{ mm} \\ \qquad\qquad 200\text{mm} \ \leq h \leq \ 357\text{mm} \\ \qquad\qquad 2 \text{ mm} \leq S \leq \ 12 \text{ mm} \\ \qquad\qquad 0.015 \text{ mm} \ \leq t \leq \ 0.07 \text{ mm} \end{cases} \tag{6.23}$$

Where S is the cell size, t is the cell thickness, and h is the impact attenuator height. The three design variables are evenly distributed between their boundaries, with five points each, leading to a total of 125 sampling points. Since the only difference between this optimisation and the previous is the height of the impact attenuator, it is not necessary to conduct further simulations, because the theoretical energy absorption is based on the scaled mean load and an assumed displacement of the impact attenuators height. Therefore it is possible to determine the influence of the height without further simulations.

To choose the order of the response surface, the R^2 and R^2_{adj} values are calculated and listed in Table 6.6. Based on these results, it is chosen to use a quartic polynomial, since the quartic function most accurately fits the sampling points and describes the influence of the three design variables on the mean load function.

	Mean load	
	$\mathbf{R^2}$	$\mathbf{R^2_{adj}}$
Quadratic	0.826	0.812
Cubic	0.984	0.981
Quartic	0.999	0.999

Table 6.6: Error evaluation of quadratic, cubic, and quartic function for the response surface.

Since three design variables are used for this optimisation, the response surface is not possible to plot. To visualise the response, first, the cell thickness is fixed at three values, smallest, middle and highest thickness, and the mass and energy absorption is plotted in relation to the cell size and height of the impact attenuator, see Figure 6.11.

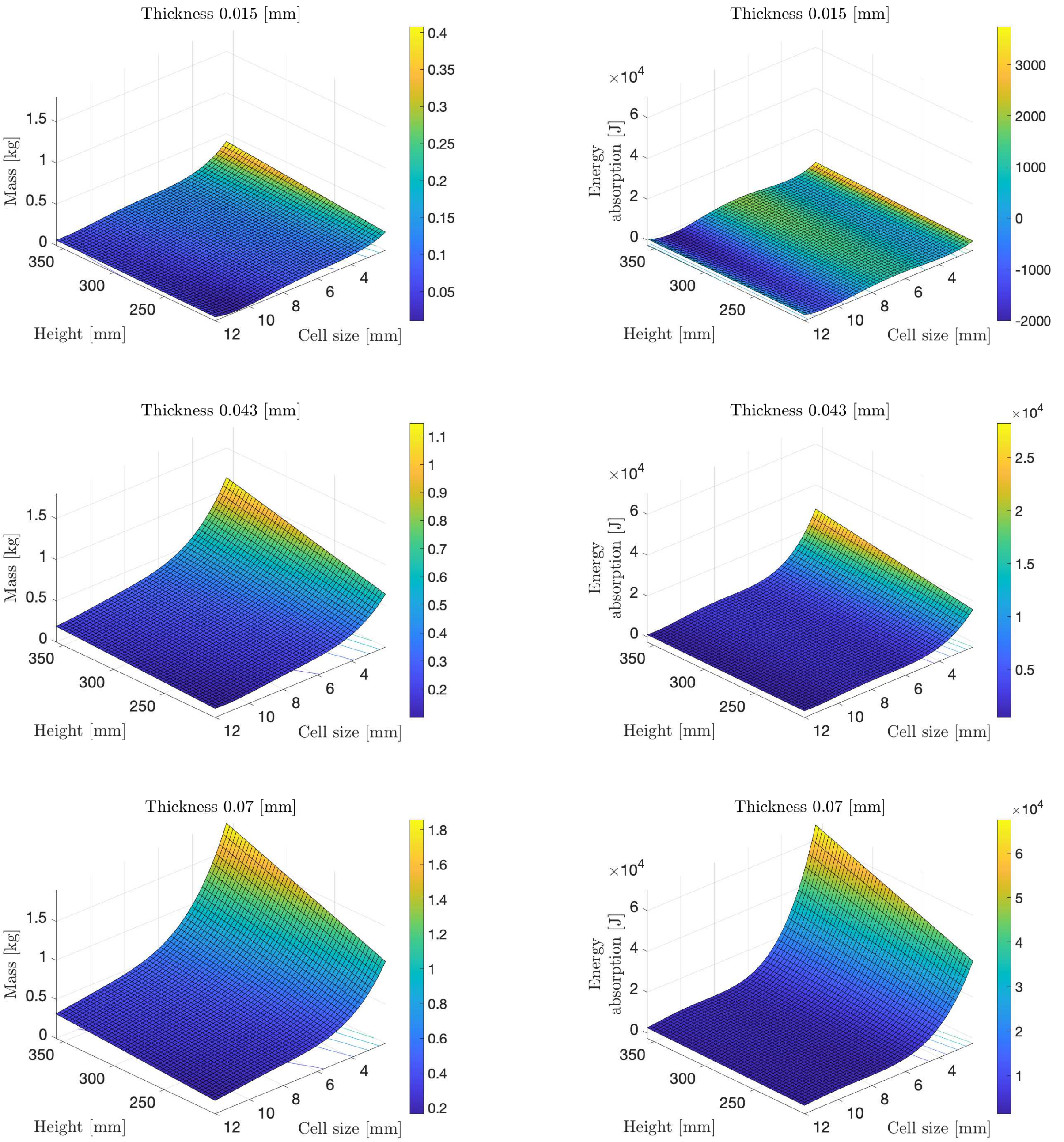

Figure 6.11: Response surfaces at three constant cell thickness; *top*: 0.015 [mm], *middle*: 0.043 [mm] and *top*: 0.07 [mm]. *Left*: Mass. *Right*: Energy absorption.

The overall trends for Figure 6.11 are as expected, where the maximum mass and energy absorption is achieved at the smallest cell size and largest height. However, a substantial deviation in the shape and values of the response surface for the energy absorption, where the cell wall thickness is fixed at 0.015 mm, is seen compared to the other two plots. From this plot, it is clear that the quartic function for the energy absorption at a cell wall thickness of 0.015 mm, does not represent the actual energy absorption, since it is possible to obtain a negative energy absorption. The reason for this comes down to the Response Surface Method, since one polynomial is used to satisfy the position of 125 sampling points, something like this might come up. The waving behaviour of this response surface, is also seen in the response surface for the first optimisation, where the cell thickness is fixed at 0.015 mm, which for better visualisation is plotted in Figure 6.12.

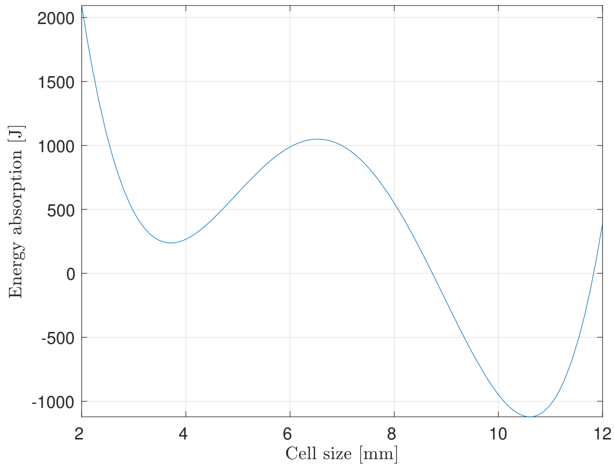

Figure 6.12: Energy absorption from optimisation 1, where the thickness is fixed at 0.015 mm

From this plot, it is seen that the response surface for the energy absorption in Optimisation 1, also can have negative values, which comes from the fitting of the function. This behaviour is most pronounced at the smallest thickness, but with a slight increase in the cell wall thickness, this behaviour is more or less gone. Due to this discovery, an optimum with a cell thickness of 0.015 mm, should not be accepted at first, but investigated further. However, this will not be the case since the constraint regarding energy absorption cannot be met with this response surface. Next, the cell size is fixed at three values, and the mass and energy absorption is plotted in Figure 6.13.

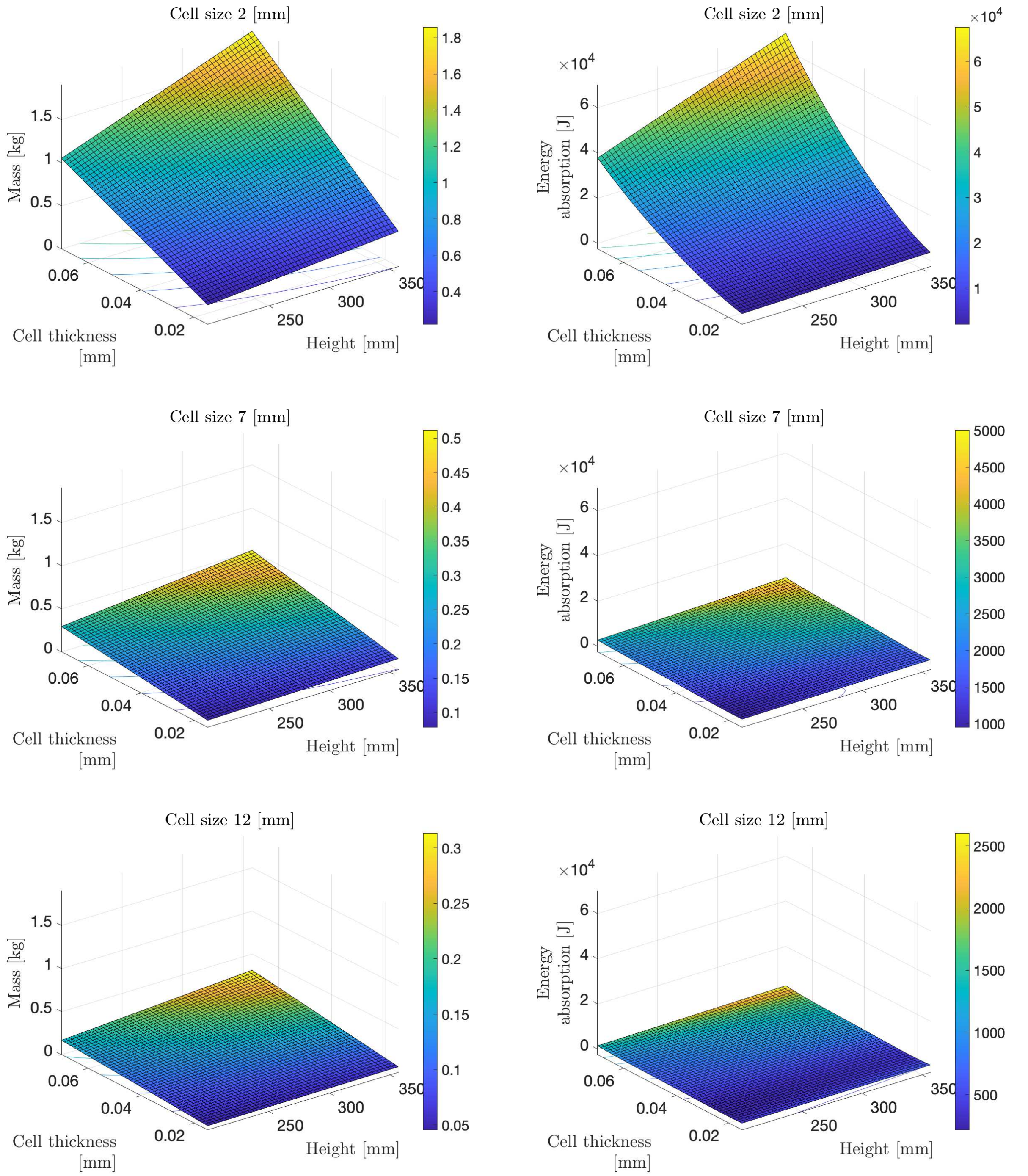

Figure 6.13: Response surfaces at three constant cell size; *top*: 2 [mm], *middle*: 7 [mm] and *top*: 12 [mm]. *Left*: Mass. *Right*: Energy absorption.

The response surfaces for constant height is not considered, since these are Figure 6.9 scaled according to the height. With these considerations regarding the response surfaces, the optimisation is carried out, and the optimum point with three design variables becomes:

$$S = 3.15 \text{ mm} \qquad t = 0.043 \text{ mm} \qquad h = 200 \text{ mm} \tag{6.24}$$

This optimisation gives the same optimum point as Optimisation 1, with two design variables and a fixed height of 200 mm. Thereby is the mass of the impact attenuator, with this optimisation is also 402.9 g, which gives a mass reduction of 2.13 kg for the front bulkhead, anti intrusion plate and impact attenuator i.e.

$$\frac{2.13\,\text{kg}}{3.42\,\text{kg}} = 62\% \tag{6.25}$$

This optimisation concludes the optimisation of the "Y" section for the impact attenuator based on the simulation model. The optimisation based on the simulations shows that the minimum mass is achieved with the minimum height of the impact attenuator and that the optimum cell size and thickness is found to be 3.15 mm and 0.043 mm, respectively. As stated previously, the simulations underestimate the mean load, meaning a lighter impact attenuator might be achieved. Furthermore, the densification strain is assumed to be 0.7 for all the honeycomb configurations, why it is possible to have a larger displacement and thereby larger energy absorption, resulting in a lighter impact attenuator. However, investigations of the material properties and the densification strain needs to be conducted, to improve the simulations and optimisation. If further investigation is carried out, the optimisation described in this chapter is still applicable. In the case that the mean load is changed significantly, it might be necessary to reformulate the design space.

6.5 Simulation of optimum

With the optimum design variables for the "Y" section, simulations with these are carried out, to see whether the optimisation algorithm and simulation end up with the same results. The result of the simulation and optimisation is tabulated in Table 6.7.

	Optimisation		
	Sim.	Opt.	Dev.
Mean load [kN]	48.01	52.50	-8.56 %

Table 6.7: Results of the simulation of the optimum point. Sim. is the simulation results, opt. is the results from the optimisation and dev. is the deviation between the two.

From the table it is seen that the meta-model over estimate the mean load compared the simulation. Even though the simulation result is lower than the optimisation results, the deviation is acceptable. Looking at Figure 6.7 and 6.8, it is observed that small changes in the region of the optimum, have a large influence on the mass and energy absorption, for the simulation results. Due to this, further investigation of this area might be needed to achieve a better response surface and thereby better agreement between the simulation and optimisation results. Due to [FSG, 2020], testing of the impact attenuator is required, since the standard impact attenuator is no longer used. In appendix G a simulation of the front bulkhead and anti intrusion plate with length and width of 100 mm and 200 mm, respectively, is carried out, to see whether the smaller dimensions of the front meets the requirements. Since physical testing of the impact attenuator is required, the results from the simulation is not sufficient to determine whether the impact attenuator satisfy the requirements. Therefore physical testing is needed to verify simulation and the [FSG, 2018] requirements.

7 — Conclusion

The goal of this project is to develop a model which can simulate the energy absorption of an impact attenuator during impact, and to use this model to design an optimised impact attenuator for AAU Racing's race car.

The selection of the material for the impact attenuator, is based on analyses of four different materials — honeycombs, balsa wood, foams, and fibre-reinforced polymers. From this analysis precrushed aluminium honeycombs is chosen, based on a large energy absorption to mass ratio, almost ideal stress-strain curve and previous work with such structures in [Simonsen et al., 2019].

Experimental work is conducted to test if impact velocities of approximately 7 m/s, has a significant influence on the deformation and stress plateau of the aluminium honeycomb. These tests are made with a drop test, where a high-speed camera records the impact, from which velocities and accelerations is derived. Based on these tests, it is concluded that it is possible to determine the mean load applied to the honeycomb at a frame rate of 5,400 fps, with agreement between the tests and data sheet for the honeycomb. However, it is also concluded that it is impossible to determine the peak load of the honeycomb from video analysis. Because of the lockdown caused by COVID-19, a limited amount of testing is done and the small amount of testing that has been done, were intended as a preliminary investigation of the test set-up and data collection system. Despite the uncertainties and limited amount of testing, it is concluded that the dynamic effects of impact velocities up to 8.40 m/s is negligible.

From preliminary considerations it is found that the model can be simplified to a "Y" section, with reduced height, due to the manufacturing method and deformation mode an adhesive bond needs to be taken into account.

The adhesive bond is modelled using the *CONTACT_AUTOMATIC_SURFACE_TO_SURFACE_TIEBREAK keyword with option = 5. While implementing the contact formulation, inconsistencies between the manual [Livermore Software Technology Corporation, 2019] and results of the simulations is observed. Therefore, simplified models are made, from which it is concluded that the yield criterion for the contact formulation is not consistent with what is stated in the manual, i.e. it should be:

$$f\left(\sigma_n,\sigma_s\right) = \frac{\sqrt{\sigma_n^2 + 3\ \left|\sigma_s\right|^2}}{NFLS\ SF_{dmg}} \leq 1 \Rightarrow \frac{\sqrt{\sigma_n^2 + 3\ \left|\sigma_s\right|^2}}{NFLS} \leq SF_{dmg} \tag{7.1}$$

With an understanding of the contact formulation, it is implemented in the model for the "Y" section, where it is seen that the deformation mode is consistent with the description in [Wierzbicki, 1983] and the conducted experiments.

With the model able to simulate the correct deformation mode and the variables in the contact formulation determined, the simulation is compared to the experimental data. It is found that the first material model used for the aluminium provides a significant lower mean load than that obtained in the experiments. Therefore is different material parameters implemented and the material model is developed gradually. A plausible material model is found where the mean load deviates -1.4% for the minimum mean load obtained in the experiments and -21.1% for the maximum.

To validate the use of the "Y" section a seven cell honeycomb model is developed. It is found that there is a deviation of -4.68% from the scaled mean load of a "Y" section. However, this is considered a small enough deviation such the "Y" section can be used for the optimisation. With these results it is concluded that the model simulates the mean load to sufficient accuracy, when considering the lack of experimental data to verify further.

The optimisation of the impact attenuators mass is based on constraints determined by the formula student rules and the scaling of the mean load obtained in the simulation. An initial optimisation of the impact attenuator is made from the data sheets of available commercial honeycombs, which resulted in a minimum mass of $m_{IA} = 366.1$g, for a honeycomb made in the same material as in the model. This optimised impact attenuator reduced the mass of the original impact attenuator by 48%. Since this impact attenuator is constrained by the minimum nominal area, the mass of the front bulkhead, anti intrusion plate and impact attenuator is also reduced, whereby the total mass is reduced by 2.17 kg, which is a reduction of 63%.

Since there is no explicit function for the mean load obtained from the simulations, it is decided to use the Response Surface Method. By using the Response Surface Method, a meta-model is made from a number of sampling points for the mean load, dependant on the design variables. From this it is decided to initiate the optimisation with two design variables, the cell thickness and size, and afterwards add the height of the impact attenuator as a design variable. With the chosen sampling points it is decided to describe the response surface by a quartic function. The optimum for the two optimisation runs end up identical, meaning that there is no benefit in increasing the height of the impact attenuator. The mass of the optimised impact attenuator is $m_{IA} = 402.9\,$g, which is a reduction of 42% from the original impact attenuator. Since both optimisations have the minimum nominal area as a constraint, the total mass reduction of the front bulkhead, anti intrusion plate and impact attenuator is reduced by 62%.

The optimum "Y" section is simulated to test the agreement between the meta-model and simulation. It is found that the meta-model over estimates the mean load compared to the simulations, with a deviation of -8.56 % and is considered acceptable. Since physical testing of the impact attenuator is required, the found optimum is considered a good starting point for further testing.

8 — Perspectivation

Throughout this project, several choices and decisions have been made. In this chapter, these decisions is revised and alternative approaches which could have been taken is discussed. This discussion is mainly based on the primary decisions, which has a large influence on the design of the impact attenuator and the simulations, i.e. the material selection, honeycomb geometry, optimisation algorithm etc.

8.1 Material selection

In this project it is chosen to use aluminium honeycombs in the design of the impact attenuator. However, as described in chapter 2, several materials are suited for this. These materials have either been used in impact attenuator designs, as seen in Figure 8.1, or have shown a high specific energy absorption — energy absorption relative to the mass. By changing the material to one of those mentioned in chapter 2, it might be possible to minimise the mass of the impact attenuator further than that obtained from an optimisation of the honeycomb structure.

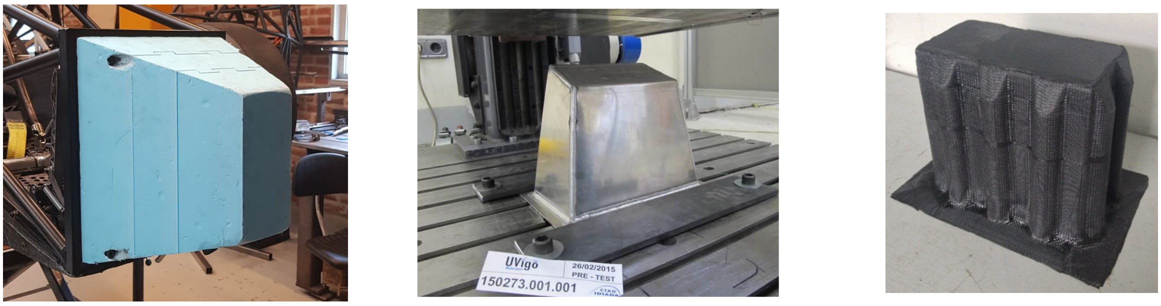

Figure 8.1: *Left:* Formula Seven's standard impact attenuator. *Centre:* Aluminium impact attenuator [López-Campos et al., 2020]. *Right:* Carbon fibre reinforced polymer impact attenuator [Wang et al., 2016].

The change from an aluminium honeycomb structure, to either a foam, balsa or carbon fibre reinforced polymer based impact attenuator, requires a new approach to the design of the impact attenuator. This approach needs to focus on the shape of the impact attenuators geometry, instead of focusing on the cell size and thickness, which could result in some interesting geometries of the impact attenuator as seen from Figure 8.1. Furthermore, each of these materials also has their own defining parameters, which needs investigation e.g. a carbon fibre reinforced polymer needs a definition of the lay-up.

Finally, as it is found in chapter 2 balsa wood shows high specific energy absorption, which is an excellent feature for this problem. Thus, if considering to make a design of balsa wood rather than using a solid block, balsa shows great potential — same can be said for aluminium, which is not tested.

8.1.1 Cell shape

Only honeycombs with hexagonal regular cells have been considered in this project. However, [Meng et al., 2014], have investigated the energy absorption and peak stress for square cells honeycomb and compared it with hexagonal cells. Here it is shown that the square cells absorb a larger amount of energy for the same thickness and wall length. The peak stress is higher too, which is not a desired property of the honeycomb. However, if pre-crushed the larger peak might be smaller as with hexagonal honeycombs. Therefore it could be interesting to investigate honeycombs with a square cell structure.

It could also be interesting to analyse other cell shapes than regular cells e.g. cells where the walls with adhesive is either shorter or longer than the other cell walls.

8.2 Dynamic experiments

The experiments in this project has several uncertainties mainly the size of the test samples and in the calculation of the velocity and acceleration, when analysing the video at high frames per second. Some of these problem is due to the current situation with the lockdown, which has resulted in a limited amount of testing. However, additions to the experimental set-up could be made to ensure a more reliable method of determining the energy absorbed and the deceleration of the impactor. Two of these additions is to implement an accelerometer on the impactor and use a strain gauge set-up on the structure which the impactor hits. With these two measures it would be possible to relate the decelerations obtained from the video analysis with those obtained from the accelerometer while being able to relate the force derived from the decelerations with the force derived from the strain gauge set-up. Furthermore, it would be possible to make a stress-strain curve from the three different data collection methods and compare them. These two additions to the experiment would thereby add to the verification of the data, providing more reliable measurements.

8.2.1 Dynamic impact test

To verify whether the optimised honeycomb impact attenuator complies with the formula student rules, the dynamic test described in chapter 1 must be performed. Therefore, is the next step in the design process, physical testing of the impact attenuator. This step means that the impact attenuator needs to be made with a test rig meeting the requirements in [FSG, 2020].

8.3 Automation of optimisation with gradient based line search

To make the optimisation automated it would probably make sense to implement gradient based line search rather than using Response Surface Method. Further, it would probably also make sense only to use one computer, either do everything on the remotely controlled computer, or everything on a PC. At least initially to avoid the troubles it would bring. Next, an automation of data extraction from LS-PrePost is needed. Macros made with command files, see appendix C, can be used to extract data, though, the automation of running such a macro would require a different macro, which should be run through the OS or maybe MATLAB. Otherwise, the transition to an automated algorithm does not seem too troublesome. This is due to the model is parameterised through a MATLAB script already. A display of the required work flow is shown in Figure 8.2.

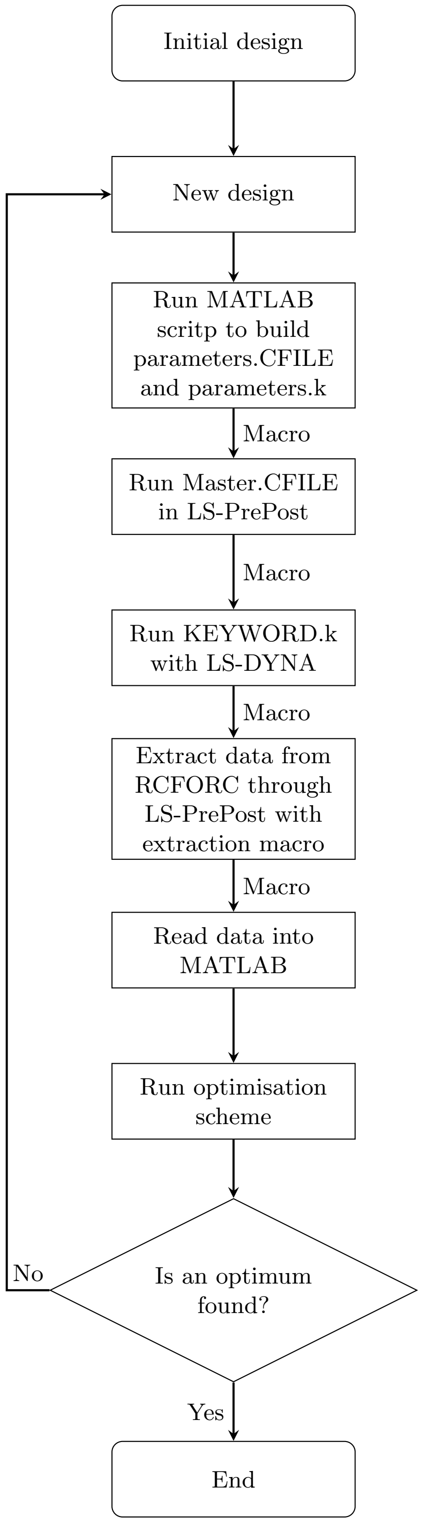

Figure 8.2: Flowchart of automated optimisation.

Bibliography

Aji et al., 12 2018. Satriya Aji, Young Kim, Kook Ahn and Young Lee. *Life-Cycle Cost Minimization of Gas Turbine Power Cycles for Distributed Power Generation Using Sequential Quadratic Programming Method.* Energies, 11, 3511, 2018. doi: 10.3390/en11123511.

ANSYS, 2015. ANSYS. *ANSYS Mechanical APDL Element Reference*, 2015.

Arora, 2016. Jasbir Singh Arora. *Introduction to Optimum Design Fourth Edition.* ISBN: 978-0-12-800806-5, Elsevier Academic Press, Hardcover. Elsevier, 2016.

Bitzer, 1997. Tom Bitzer. *"Honeycomb Technology".* ISBN: 0-412-54050-9. Chapman and Hall, 1997.

Cook et al., 2001. Robert D. Cook, Davis S. Malkus, Michael E. Plesha and Robert J. Witt. *Concepts and Applications of Finite Element Analysis.* ISBN: 978-0-471-35605-9. John Wiley & sons, INC., 2001.

Cooman et al., 2017. Bruno C. De Cooman, Yuri Estrin and Sung Kyu Kim. *Twinning-induced plasticy (TWIP) steels.* Acta Materialia, 2017. URL `https://www.sciencedirect.com/science/article/pii/S1359645417305219`.

deMilked, 2015. deMilked. *Cheet Sheet for Every Beginner Photographer.* https://www.demilked.com/photography-shutter-speed-aperture-iso-cheat-sheet-chart-fotoblog-hamburg-daniel-peters/, 2015. Downloaded: 13-03-2020.

Easycomposites, 2020. Easycomposites. *Aluminium Honeycomb.* `https://www.easycomposites.co.uk/#!/core-materials/aluminium-honeycomb/3mm-aluminium-honeycomb.html`, 2020. Downloaded: 25-02-2020.

Easycomposites. Easycomposites. *Technical data sheet - Aluminium honeycomb core material.* URL `https://system.eu2.netsuite.com/core/media/media.nl?id=5262&c=3937524&h=49cb64c8432f549df1f8&_xt=.pdf`. Downloaded: 2019-11-14.

Endelt, 2018. Benny Endelt. *Notes for course on Process Modelling and Simulation, 2018*, 2018. Downloaded: 18-09-2019.

Fang et al., 02 2005. H. Fang, M. Rais-Rohani, Z. Liu and M.F. Horstemeyer. *A comparative study of metamodeling methods for multiobjective crashworthiness optimization.* Computers & Structures, 83, 2121–2136, 2005. doi: 10.1016/j.compstruc.2005.02.025.

Fazilati and Alisadeghi, 2016. Jamshid Fazilati and Maryam Alisadeghi. *Multiobjective crashworthiness optimization of multi-layer honeycomb energy absorber panels under axial impact.* Thin-Walled Structures, 2016. ISSN 0263-8231. doi: https://doi.org/10.1016/j.tws.2016.06.008. URL `http://www.sciencedirect.com/science/article/pii/S0263823116303391`.

Formula Seven, 2020. Formula Seven. *Formula Seven homepage.* http://www.formula-seven.com/, 2020. Downloaded: 4-02-2020.

FSG, 2018. FSG. *Formula Student Germany Rules 2019 v1.1.* https://www.formulastudent.de/fsg/rules/, 2018. Downloaded: 05-02-2019.

FSG, 2020. Formula Student Germany FSG. *Formula Student Rules 2020.* https://www.formulastudent.de/fsg/rules/, 2020. Downloaded: 5-02-2020.

Gibson and Ashby, 1997. Lorna J. Gibson and Michael F. Ashby. *Cellular Solids: Structure and Properties.* Cambridge Solid State Science Series. Cambridge University Press, 2 edition, 1997. doi: 10.1017/CBO9781139878326.

Hansen et al., 2018. Kristian Hansen, Frederik E. Jensen, Morten V. Jensen, Oliver H. O. Kragh, Casper H. Larsen and Mikkel J. Njor. *P1 - Impact Attenuator*, 2018.

Heimbs et al., 2009. Sebastian Heimbs, F. Strobl, Peter Middendorf, S. Gardner, B. Eddington and J. Key. *Crash Simulation of an F1 Racing Car Front Impact Structure.* 2009. URL https://www.dynamore.de/en/downloads/papers/09-conference/papers/B-I-02.pdf/view.

Hou et al., 2007. Shujuan Hou, Qing Li, Shuyao Long, Xujing Yang and Wei Li. *Design optimization of regular hexagonal thin walled columns with crashworthiness criteria.* Finite Elements in Analysis and Design, 2007. URL https://www.sciencedirect.com/science/article/pii/S0168874X06002046.

Hull, 1991. D. Hull. *A unified approach to progressive crushing of fibre-reinforced composite tubes.* Composites Science and Technology, 1991. URL http://www.sciencedirect.com/science/article/pii/026635389190031J.

Khan et al., 2011. M. K. Khan, T. Baig and S. Mirza. *Experimental investigation of in-plane and out-of-plane crushing of aluminium honeycomb.* Materials Science and Engineering, 2011. URL https://www.sciencedirect.com/science/article/pii/S0921509312001062.

Livermore Software Technology Corporation, 2019. Livermore Software Technology Corporation. *LS-DYNA Support.* https://www.dynasupport.com, 2019. Downloaded: 01-10-2019.

López-Campos et al., 2020. José A. López-Campos, Jacobo Baldonedo, Sofía Suárez, Abraham Segade, Enrique Casarejos and José R. Fernández. *Finite Element Validation of an Energy Attenuator for the Design of a Formula Student Car.* 2020. ISSN 2227-7390. doi: 10.3390/math8030416. URL https://www.mdpi.com/2227-7390/8/3/416.

Lu and Yu, 2003a. Guoxing Lu and T. Yu. *Energy Absorption of Structures and Materials.* Energy Absorption of Structures and Materials, 2003a.

Guoxing Lu and Tongxi Yu. 11 - Composite materials and structures. In Guoxing Lu and Tongxi Yu, editor, *Energy Absorption of Structures and Materials*, Woodhead Publishing Series in Metals and Surface Engineering, pages 317 – 350. Woodhead Publishing, 2003b. ISBN 978-1-85573-688-7. doi: https://doi.org/10.1533/9781855738584.317. URL http://www.sciencedirect.com/science/article/pii/B9781855736887500150.

Lund and Lindgaard, **2018**. Erik Lund and Esben Lindgaard. *Notes for course on Finite Element Methods, 2018*, 2018. Downloaded: 21-09-2018.

Magee and Thornton, **02 1978**. Christopher Magee and P.H. Thornton. *Design Considerations in Energy Absorption by Structural Collapse*. SAE Prepr, 87, 2041–2055, 1978. doi: 10.4271/780434.

MathWorks, **2020**. MathWorks. *Constrained Non linear Optimization Algorithms*. https://se.mathworks.com/help/optim/ug/constrained-nonlinear-optimization-algorithms.html#bsgppl4, 2020. Downloaded: 10-05-2020.

MatWeb, **2020**. MatWeb. *Aluminum 5052-O*. http://www.matweb.com/search/DataSheet.aspx?MatGUID=b3430ccca1334449b0d59cde9f977b57&ckck=1, 2020. Downloaded: 18-05-2020.

Meng et al., **2014**. Li Meng, Deng Zong-quan and Guo Hong-wei. *Optimizing crashworthiness design of square honeycomb structure*. 2014. URL https://www.researchgate.net/publication/278123866_Optimizing_crashworthiness_design_of_square_honeycomb_structure.

Min et al., **2011**. HE Min, LI Fuguo and Wang Zhigang. *Forming Limit Stress Diagram Prediction of Aluminum Alloy 5052 Based on GTN Model Parameters Determined by In Situ Tensile Test*. 24, 2011.

Overgaard, **2014**. Lars Overgaard. *Mechanics of Composite Materials and Structures*, 2014. Downloaded: 27-2-2019.

Physlets. Physlets. *Autotracker*. URL https://physlets.org/tracker/help/autotracker.html. Downloaded: 2019-11-05.

Physlets. Physlets. *Tracker 5.0 Help*. Downloaded: 21-04-2020.

Plascore, **2020**. Plascore. *Plascore CrushLite*. https://www.plascore.com/honeycomb/energy-absorbtion/crushlite/, 2020. Downloaded: 02-03-2020.

Silva and Kyriakides, **2007**. A. Da Silva and S. Kyriakides. *Compressive response and failure of balsa wood*. Solids and Structures, 2007. URL https://www.sciencedirect.com/science/article/pii/S0020768307002727.

Simonsen et al., **2019**. C. Simonsen, N. Broberg and J. Sørensen. *Analysis and Modelling of the Deformation Behaviour of Metallic 2D Cellular Structures*, 2019.

Slik et al., **02 2020**. Gerhard Slik, Gavin Vogel and Virendra Chawda. *Material Model Validation of a High Efficient Energy Absorbing Foam*. 2020.

Tagarielli et al., **2007**. V. L. Tagarielli, V. S. Deshpande and N. A. Fleck. *The high strain rate response of PVC foams and end-grain balsa wood*. Composites, 2007. URL https://www.sciencedirect.com/science/article/pii/S1359836807000406.

Varmint Al, 2019. Varmint Al. *Varmint Al's Engineering Page.* https://www.varmintal.com/aengr.htm, 2019. Downloaded: 12-09-2019.

Wang et al., 2016. Jianfeng Wang, Na Yang, Jinghui Zhao, Dafang Wang, Yongtai Wang, Kun Li, Zhongqing He and Baoming Wang. *Design and experimental verification of composite impact attenuator for racing vehicles.* 2016. doi: https://doi.org/10.1016/j.compstruct.2016.01.013. URL http://www.sciencedirect.com/science/article/pii/S026382231600026X.

Wierzbicki, 1983. Tomasz Wierzbicki. *Crushing analysis of metal honeycombs.* International Journal of Impact Engineering, 1(2), 157 – 174, 1983. ISSN 0734-743X. doi: https://doi.org/10.1016/0734-743X(83)90004-0. URL http://www.sciencedirect.com/science/article/pii/0734743X83900040.

Xu et al., 2012. S. Xu, J. H. Beynon, D. Ruan and G. Lu. *Experimental study of the out-of-plane dynamic compression of hexagonal honeycombs.* Composite Structures, 2012. URL https://www.sciencedirect.com/science/article/pii/S0263822312000773.

Yamashita and Gotoh, 2004. M. Yamashita and M. Gotoh. *Impact behavior of honeycomb structures with various cell specifications - numerical simulation and experiment.* International Journal of Impact Engineering, 32, 618 – 630, 2004. URL https://www.sciencedirect.com/science/article/pii/S0734743X04001897.

Zhou et al., 08 2012. Zhiwei Zhou, Zhihua Wang, Longmao Zhao and Xuefeng Shu. *Experimental investigation on the yield behavior of Nomex honeycombs under combined shear-compression.* Latin American Journal of Solids and Structures, 9, 515 – 530, 2012. ISSN 1679-7825. URL http://www.scielo.br/scielo.php?script=sci_arttext&pid=S1679-78252012000400006&nrm=iso.

ZwickRoell. ZwickRoell. *statische materiaaltestmachine.* URL https://www.zwickroell.com/nl-nl/products. Downloaded: 28-11-2019.

A — Experiments

The following is a duplication of the chapter "Experiments", from [Simonsen et al., 2019]. It should not be a part of the evaluation, but as a help for the reader. Some parts have been left out, such only relevant content is repeated.

To verify the finite element model, the deformation behaviour of metal honeycomb structures is investigated for static out-of-plane loads, by experiments carried out on test samples provided by Sintex, aluminium honeycombs and aluminium square profiles. Based on the observed deformation and the force-displacement curves, the finite element model is compared and verified. In this chapter the experimental setup and results is described and presented.

A.1 Experiment set up

In this project static compression tests is performed, to observe the deformation and out-of-plane characteristics of several test samples. These static tests are done with two different testing machines, a ZWICK Z100/TLl3s 100 kN testing machine and a Schenck-Trebel 600 kN testing machine, shown on Figure A.1. This is due to the force required to crush the Sintex honeycomb test samples, determined from an initial test.

The difference between these testing machines, besides the amount of force which the two machines can apply, is that the ZWICK applies the load by an electric screw-driven crosshead and the Schenck-Trebel moves the crosshead with a hydraulic piston and cylinder. By these two different mechanisms the two test machines drives a crosshead at a controlled rate. Where the ZWICK testing machine, is given a constant testing velocity (m/s) as input, at which the upper crosshead is moving, until a given force and/or displacement is reached. It is advised to use maximum 80% of the 100 kN the ZWICK can apply, to avoid failure of the machine. Therefore, a stopping criteria is set at 80 kN. Whereas the Schenck-Trebel testing machine is given a linearly increasing force over time (N/s) as input, at which the lower crosshead is moving. When the test sample becomes dense and acts as a solid block, the test is stopped manually or automatic because the maximum force is reached. The following procedure for the experiment is used.

1. A test sample is placed at the centre of the lower cross head, where solid steel plates is mounted on the upper and lower crossheads, providing a flat plane at which the test sample is crushed between. These steel plates are assumed to be rigid and not affecting the absorbed energy.
2. When the test sample is placed, the test begins, where the movable crosshead is driven at a controlled rate at the given inputs.
3. A computer connected to sensors mounted in the machines, logs the force and the travel distance of the movable crosshead, at a given frequency, giving the force-displacement curve.
4. To analyse and document the deformation process, a video recording of the tests, is taken.

Figure A.1: *Left:* ZWICK Z100/TLl3s 100 kN testing machine [ZwickRoell]. *Right:* Schenck-Trebel 600 kN testing machine.

A.2 Aluminium honeycomb

To check the test set up for possible sources of errors, a hexagonal aluminium honeycomb is tested. This aluminium honeycomb is tested since it is expected to have a typical force-displacement behaviour for a metallic honeycomb.

A.2.1 Test samples

The aluminium honeycomb is an expanded honeycomb made from aluminium 5052, with a cell diameter of 3.2 mm and a height of 20 mm, see Figure A.2. This manufacturing technique bonds the rows of cells by an adhesive. This means that some of the walls has twice the thickness of the others. Since the main focus of this project is to understand the behaviour of powder metal extruded honeycombs, is these tests only used as a control for the test set up.

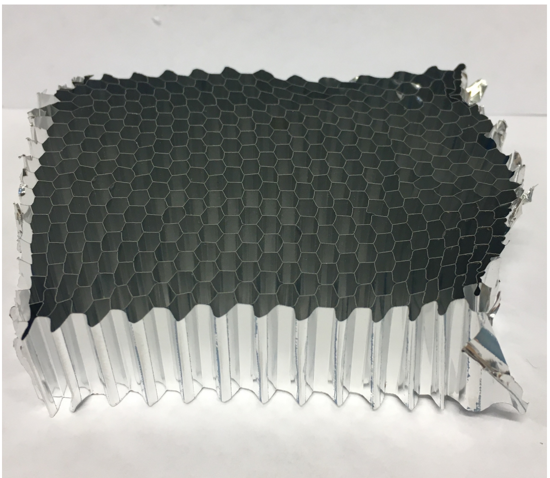

Figure A.2: Aluminium honeycomb test sample 1, before the test.

From the honeycombs data sheet [Easycomposites], a bare compressive strength and a stabilised compressive strength is given. The difference between these two, is how the specimen is tested. Stabilised specimens have a thin facing applied to one or both sides, and the bare specimens have no facings. Since there is not applied any facings to the test samples, the samples is bare specimens. In the data sheet, the bare compressive strength is given as 539 psi which is approximately 3.72 MPa, while the crushing strength is given as 255 psi which is approximately 1.76 MPa. These values are for typical properties and should not be considered minimum or maximum. The compressive strength, σ_c, is defined as,

$$\sigma_c = \frac{P_{max}}{A} \tag{A.1}$$

where P_{max} is the maximum/peak load reached before buckling, and A is the in-plane area including areas with no material. For the test, two test samples are used. These samples is not completely rectangular or quadratic, as seen in Figure A.2. Therefore only approximations of the two samples area is calculated, by simplifying the specimens to be described by one length and one width, given in Table A.1.

	Width [mm]	Length [mm]	Area [mm^2]
Sample 1	75	70	5,250
Sample 2	80	80	6,400

Table A.1: Approximated dimensions of the two aluminium honeycomb samples, along with their nominal area.

Based on the approximated nominal areas, the compressive strength and the crush strength, an estimate of the peak and mean load is calculated, see table A.2.

A.2.2 Results

The ZWICK is used for these tests, since the maximum estimated peak load is 23.81 kN, see Table A.2. In these tests a velocity of 10 mm/min is used, whereby inertia effects are assumed negligible. The first test, is stopped at 60% deformation of the honeycomb while the second test is stopped when the honeycomb reaches densification. The reason for stopping the tests at different deformations is to see the deformation of a semi-crushed structure and a fully crushed structure.

By visual inspection during and after the tests, it is seen that the expected deformation occurs. Where a folding mechanism develops as the deformation is continued after the peak load, see Figure A.3.

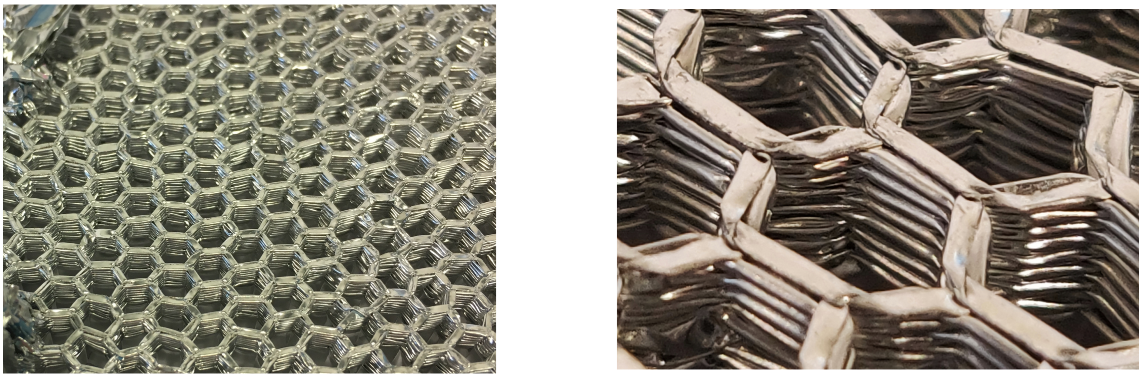

Figure A.3: *Left:* Aluminium honeycomb test sample 1, after the test. *Right:* Zoom of the aluminium honeycomb sample 1, after the test, where folding mechanism is seen.

This is also seen in the force-displacement curves in Figure A.4, where several peaks and valleys indicates when a new fold is made. From the force-displacement curves, it is seen that they follows the same pattern, as that of a typical metallic honeycomb. Where a peak load is reached followed by a drop to a mean load, leading to densification of the honeycomb. Where the densification of the honeycomb occurred at a displacement of approximately 16 mm, which is a deformation of 80%.

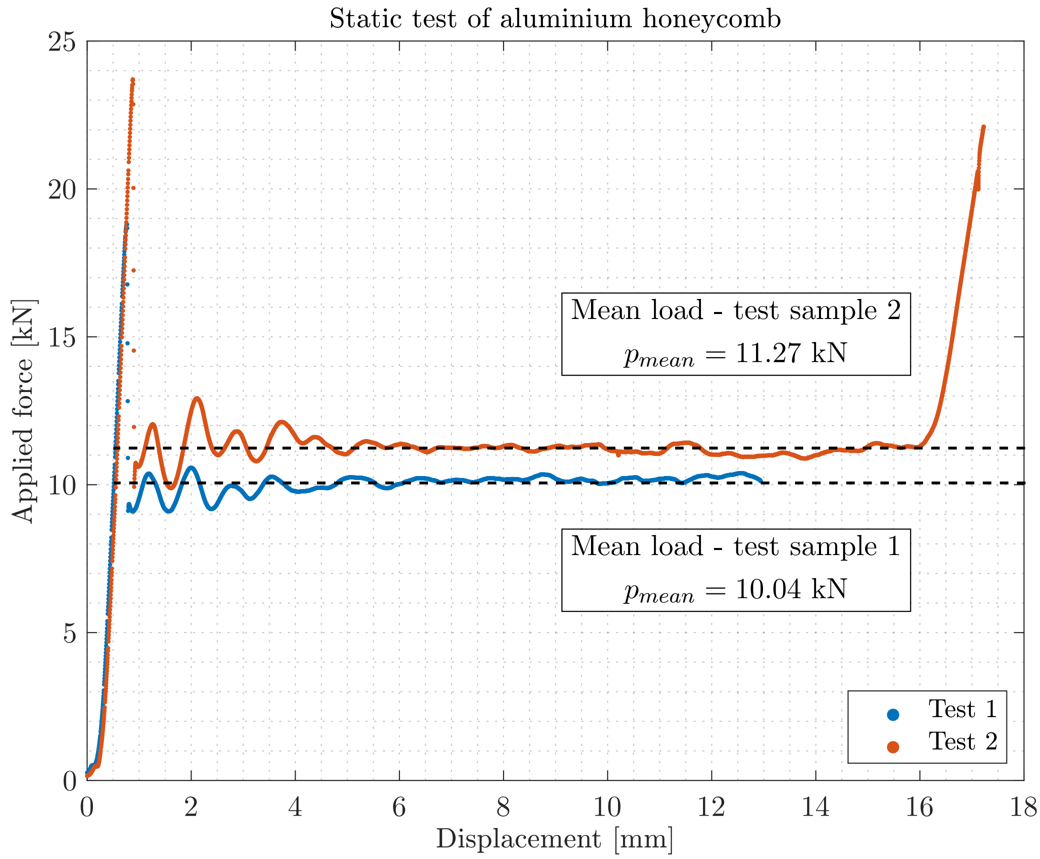

Figure A.4: Force-displacement curve for the aluminium honeycombs. Two tests are conducted, where Test 1 has an original width of 75 mm, a length of 70 mm and a height of 20 mm. Test 2 has an original width of 80 mm, a length of 80 mm and a height of 20 mm. Test 1 is deformed 60% of the original height and Test 2 is deformed to densification, occurring at approximately 16 mm. Sample rate is 36 Hz.

The difference between the two curves is caused by a difference in outer dimensions, where the honeycomb sample 2 has a larger area, however the size of the cells are the same for the two tests.

	Sample 1	Sample 2
Estimated peak load [kN]	19.53	23.81
Measured peak load [kN]	18.80	23.71
Deviation [%]	3.74	0.42
Estimated mean load [kN]	9.24	11.26
Measured mean load [kN]	10.04	11.27
Deviation [%]	-8.66	-0.09

Table A.2: Estimated peak and mean load. The mean loads are derived from the data after the drop from the peak load to a point before densification for test 2.

From these tests, it is seen that the aluminium honeycomb deforms and behaves as a typical metallic honeycomb. Furthermore the estimated peak and mean load values are close to the measured. With these results, it is determined that the test procedure is a valid method of testing statically the honeycomb structures.

B — Tracker

To analyse the data from the high-speed camera, the free video analysis and modelling tool Tracker is used. The following is based on [Physlets]. To analyse the impactors position, velocity and acceleration, the image series, obtained from the high-speed camera, is pre-processed. This pre-processing consists of selecting the initial and end frame in the image series, calibrating the series by setting a fixed distance, setting a coordinate system and tracking a target on the impactor between each frame. Thereby, the position is determined from the number of pixels which the target has moved from the previous frame. The velocity and acceleration are determined based on the position to time data, using the Central Finite Difference scheme:

$$\begin{aligned} v_i &\approx \frac{x_{i+1} - x_{i-1}}{2dt} \\ a_i &\approx \frac{v_{i+1} - v_{i-1}}{2dt} \approx \frac{x_{i-2} - 2x_i + x_{i+2}}{4dt^2} \end{aligned} \tag{B.1}$$

Where x_i refers to the position at the i^{th} frame and, dt is the time between each frame. The tracking of the target can be done manually, but it is chosen to use the auto-tracking feature within the program. Figure B.1 shows a picture from Tracker, where the fixed distance, coordinate system and points to auto-track are shown. Where the fixed distance (blue) is set from the calibration zone, the coordinate system (purple) is set, such the y-axes follow the target, which is to be auto-tracked (red, cyan and purple dots).

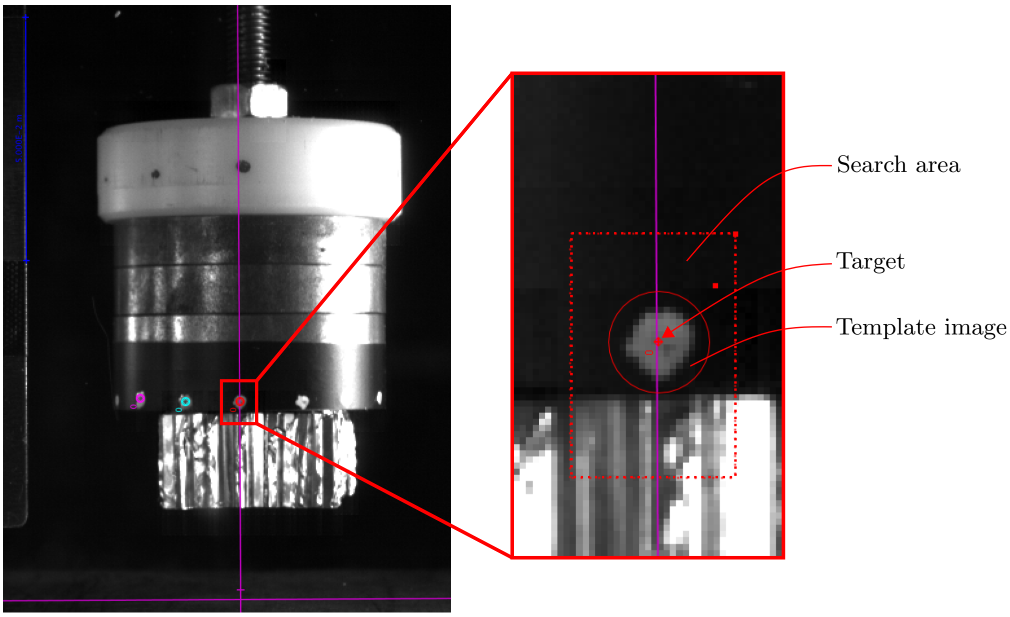

Figure B.1: Picture from Tracker showing the pre-processing and initialisation of the auto-tracking. With the fixed distance (blue line to the left), coordinate system (purple lines) and points to auto-track (red, cyan and purple dots) are shown.

The auto-tracking is started by defining a template image, search area and target, see B.1. The template image is the image that every other test images are trying to match, the search area is the area in which the algorithm is searching for test images and the target is the point at which the program measures position from the given coordinate system.

The auto-tracker works by computing the RGB difference between the template image and every test image in the search area, whereby the smallest RGB difference identifies a match image. The RGB difference is calculated with equation B.2 [Physlets].

$$\text{RGB diff} = \sum_{i=1}^{N} \left[(\Delta R_i)^2 + (\Delta G_i)^2 + (\Delta B_i)^2 \right] \tag{B.2}$$

Where ΔR, ΔG and ΔB are the difference of the red, green and blue pixel value between the test and template image, respectively, which is summed over all pixels contained in the test image. Since the high-speed camera captures all images in black and white, the red, green and blue pixels values are the same. An example of the RGB difference between two pixels is illustrated by two squares, representing the template pixel and the test pixel, see Figure B.2.

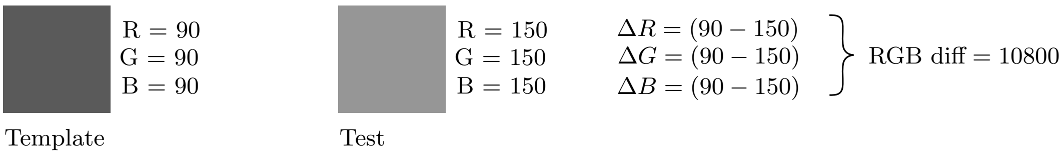

Figure B.2: Example of RGB difference between a template pixel and a test pixel.

Afterwards, a match score is determined. This score determines whether the identified match image is good enough to continue to the next frame. This score is determined as the mean RGB difference of all the test images, divided by the RGB difference in the matched image minus one.

$$\text{Match score} = \left(\frac{\text{mean RGB diff}}{\text{match RGB diff}} \right) - 1 \tag{B.3}$$

Thus a poor match image scores zero and a perfect match score infinitely high. According to [Physlets], a good match has a score higher than four. When the best match is found, a point is automatically marked at the target position, and it analyses the next frame.

The targets must be clear and visible to get a high match score. Because of that, black tape is attached to the lowest of the blocks whereon white markers are painted, giving a high contrast between the white and black, resulting in high match scores. Another benefit of using tape is that the reflection is reduced compared to the steel blocks. Furthermore, multiple targets are auto-tracked to ensure that the measured target is not an outlier. These markers are placed over the width of the block to get a fair estimation of the motion, see Figure B.1.

C — Model Structure in LS-PrePost and LS-DYNA

LS-DYNA is the solver and can only read the so-called keyword files with the extension ".k", where LS-PrePost is used for pre and post processing LS-DYNA simulations i.e. LS-PrePost generates and reads keyword files, while it also reads the different types of LS-DYNA result files.

Macros can be used in LS-PrePost to generate keyword files, these macros are called command files and has the extension ".CFILE". The syntax in keywords and command files are completely different. Further, no official documentation of the LS-PrePost commands exists which makes it troublesome to write a macro. However, when ever using the graphical user interface (GUI), LS-PrePost prints the command that is used in a log file. Though, deciphering the purpose of each entity in a command can be difficult and are time consuming. However, it is necessary to use command files to make use of the preprocessing in LS-PrePost somewhat automatic. The most important feature of the preprocessing in LS-PrePost is that a mesh can be generated from a CAD drawing. If the mesh were to be manually generated in keyword format, all node coordinates would have to be written in a code. Further, it must be defined which nodes belong to which elements which actually is quite a difficult task, as the nodes in a element must be defined in a correct sequence. If an incorrect sequence is used, the mapping in the isoparametric formulation is wrong, which typically results in a negative Jacobian, meaning the element volume is negative in the element coordinates. This is non-physical and returns an error.

The model is structured such every parameter in the model can be changed through one MATLAB script. This means that interdependent parameters are changed accordingly, which reduces the risk of user errors. Furthermore, this also makes it easier to implement an optimisation scheme for the aluminium honeycomb. The model structure is illustrated in Figure C.1.

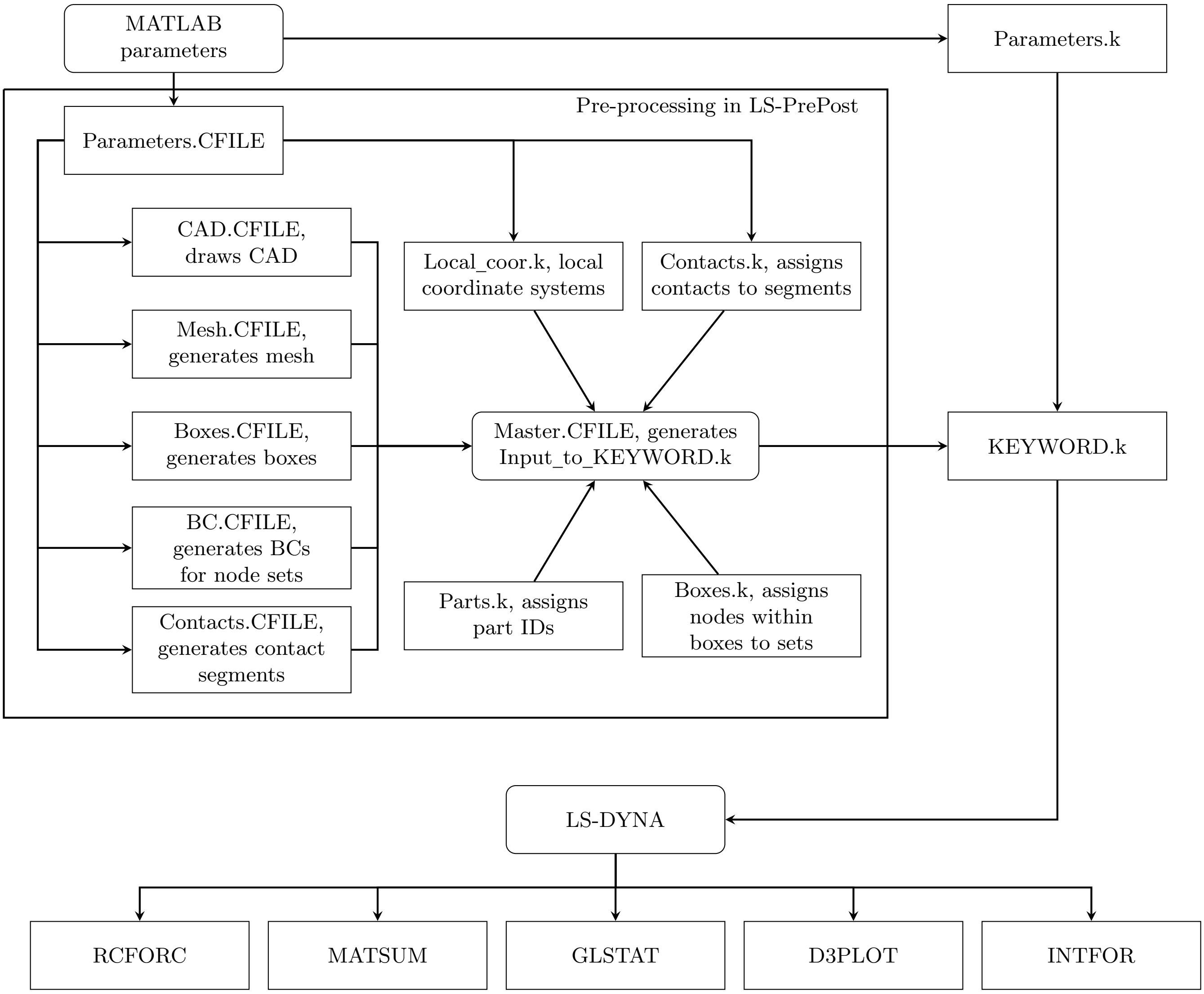

Figure C.1: Model Structure. A box in a keyword is a selection method. Here it is used to select nodes, such a set of nodes can be defined. Segments are surfaces which are in contact. RCFORC, MATSUM, GLSTAT, D3PLOT, and INFOR are result files containing different information.

D — LS-DYNA Contacts

In LS-DYNA, the general 3D contact algorithms are given by the keyword *CONTACT_{*OPTION1*}_{*OPTION2*}_..._{*OPTION5*}, where *OPTION2* to *OPTION5* adds more expressions to the contact formulations, such as thermal terms, which is not necessary for this model, why *OPTION2* to *OPTION5* is not considered in this project. The following options for *OPTION1* in the contact keyword have been investigated:

- *CONTACT_AUTOMATIC_SURFACE_TO_SURFACE_TIEBREAK
- *CONTACT_TIED_SURFACE_TO_SURFACE_FAILURE
- *CONTACT_TIEBREAK_NODES_TO_SURFACE
- *CONTACT_TIEBREAK_SURFACE_TO_SURFACE

Each of these different contact formulations has further options which need to be defined in the model, called Cards. The first four cards are the same for nearly all the contact formulations, where the only exception is *CONTACT_TIED_SURFACE_TO_SURFACE_FAILURE, where Card 2 is defined differently. The first four cards are:

- ID Card
  - A unique contact number and a name can be assign to the contact.
- Card 1
  - Slave and master segments are defined (i.e. nodes, elements, parts, etc.). This card also defines whether or not to write interface data to the database.
- Card 2
  - Card 2 has two purposes: Defining the friction in the contact and when the contact should be active.
    - For the friction part; a static and a dynamic friction coefficients are defined. Settings for more advance friction models are also applied here.
    - For the second part; a maximum allowable penetration, a birth time, and a death time can be defined.
    - If *OPTION1* is "TIED_SURFACE_TO_SURFACE_FAILURE" then a failure strength in both tension and shear are defined.
- Card 3
  - In this card scale factors for; penalty stiffness, shell element thickness, and friction coefficients can be defined.

Card 4 is where the failure of the contact is defined if *OPTION1* is one of the above mentioned. The settings in this card are dependent on the first variable of the card, which is called "OPTION", see Figure D.1. With this variable, one of 14 different contact failure formulations is applied to the model. Though all the different formulations are not suitable for modelling an adhesive bond, and not all formulations are supported for all the different contact formulations in *OPTION1*.

Card 4a	1	2	3	4	5	6	7	8
Variable	OPTION	NFLS	SFLS	PARAM	ERATEN	ERATES	CT2CN	CN
Type	I	F	F	F	F	F	F	F
Default	required	required	required	0.0	0.0	0.0	1.0	

Figure D.1: Card 4 for *CONTACT_AUTOMATIC_SURFACE_TO_SURFACE_TIEBREAK, from [Livermore Software Technology Corporation, 2019].

E — Comments on LS-DYNA documentation

The *CONTACT_AUTOMATIC_SURFACE_TO_SURFACE_TIEBREAK keyword is an example of this.

In the Keyword Manual it is stated for OPTION=5 that:

"tiebreak is active for nodes which are initially in contact. Stress is limited by the yield condition described in Remark 5 below. Damage behavior is modeled by a curve which defines normal stress vs. gap (crack opening). This option can be used to represent deformable glue bonds." [Livermore Software Technology Corporation, 2019].

Further, for $NFLS$ it is stated that:

"For OPTION = 5 NFLS becomes the plastic yield stress as defined in Remark 5." [Livermore Software Technology Corporation, 2019].

And for $SFLS$

"For OPTION = 5 SFLS becomes the curve ID which defines normal stress vs. gap." [Livermore Software Technology Corporation, 2019].

Where Remark 5 states:

"For OPTION = 5, the stress is limited by a perfectly plastic yield condition. For ties in tension, the yield condition is

$$\frac{\sqrt{\sigma_n^2 + 3|\sigma_s|^2}}{NFLS} \leq 1$$

For ties in compression, the yield condition is

$$\frac{\sqrt{3|\sigma_s|^2}}{NFLS} \leq 1$$

The stress is also scaled by the damage function which is obtained from the load curve. For ties in tension, both normal and shear stress are scaled. For ties in compression, only shear stress is scaled." [Livermore Software Technology Corporation, 2019].

To contribute the confusion some information is implemented in the graphical user interface (GUI) in LS-PrePost. Usually the information in the GUI is exactly the same as in the Keyword Manual. However, for OPTION = 5 it is stated that:

"tiebreak is active for nodes which are initally in contact. Damage is a nonlinear function of the crack width opening and is defined by a load curve which starts at unity for a crack width of zero and decays in some way to zero at a given value of the crack opening. This interface can be used to represent deformable glue bonds. " [Livermore Software Technology Corporation, 2019].

Further, there is no reference to the Theory Manual on how the interface stiffness is calculated for this specific contact formulation. In the Theory Manual a standard method of calculating interface stiffness is described for solids and shells based on element size and bulk modulus, as shown in equation 4.15 and 4.16. However two more methods are presented, though, it is explicitly stated to used for the so-called "Soft Constraint Penalty Formulation", which is not applied in the simulations. Thus, one must assume the standard method is used

F — Optimisation

The following is a duplication of the section "Optimisation", which is a part of the chapter "Further Work" from [Simonsen et al., 2019]. It should not be a part of the evaluation, but as a help for the reader. Some parts have been left out, such only relevant content is repeated.

In the further work of the model, a robust simulation of a honeycomb structure must be performed. With a robust model capable of simulate the peak load, mean load and energy absorption, an optimisation of the honeycomb can be performed with the results obtained from the model. In this section a possible optimisation process is described which can be utilised in the further work of making an optimised crash absorber.

F.1 Objective function

The goals of the optimisation is to maximise the energy absorption while minimising the mass. This requires quantifiable objective function(s), at which these can be measured, such scalar values determines the performance of the crash absorber. One of these evaluations is the specific energy absorption (SEA), which is defined by the ratio of the energy absorption to the mass of the structure, see equation F.1. This measurement is used in literature when crash absorption or crashworthiness is of interest and seen in [Meng et al., 2014], [Hou et al., 2007] and [Cooman et al., 2017].

$$SEA = \frac{\int P(\delta)\, dx}{m} \tag{F.1}$$

With this expression containing both the absorbed energy and the mass of the structure it is a good measurement for this optimisation problem. This also simplifies the optimisation problem, from being a multi objective optimisation problem to only concern one objective function. Which means the optimisation can be formulated as follows.

$$\begin{cases} Maximise & f(x_i) = SEA \\ s.t. & constraints \end{cases} \tag{F.2}$$

Since the objective function, is non-linear function of multiple variables and is not directly described by any geometrical or material properties, it is difficult to set up a parameter based objective function for the SEA with established expressions. Therefore, the Response Surface Method (RSM) could be used to obtain the objective function for the optimisation. When an objective function is determined along with constraints on the design variables, an optimisation scheme/algorithm can be chosen and implemented.

F.1.1 Response Surface Method

The following is based on [Arora, 2016]. With RSM a meta model of the objective function is made, which is a simplified function, constructed of explicit terms of the design variables.

This is done by evaluating the objective function at different sampling points i.e. with different values of the design variables. With these values the meta model is constructed as a function of a given order. For example, a meta model described by a first order function, with two design variables, x_1 and x_2, becomes,

$$f(x_1,x_2) = b_0 + b_1 x_1 + b_2 x_2 + b_{12} x_1 x_2 \tag{F.3}$$

Where the coefficients of the meta model is determined by minimising the error between the original model (FEM model) and the meta model, equation F.4. This means that the response surface is approximated by an explicit polynomial function.

$$\varepsilon(x_i) = f(x_i) - \tilde{f}(x_i) \tag{F.4}$$

The approximated function of the response surface is denoted $\tilde{f}$, and is defined in equation F.5.

$$\tilde{f}_i = d_0 + \sum_{j=1}^{l} d_j \xi_{ij}, \qquad i = 1 \text{ to } k \tag{F.5}$$

Where d are the unknown coefficients of the function, l is the number of coefficients in $\tilde{f}$, k is the number of sampling points and ξ is a simplified notation for the design variables, given as,

$$x_1 \rightarrow \xi_1, \ldots, x_1^2 \rightarrow \xi_{n+1}, \ldots, x_{n-1}x_n \rightarrow \xi_l \tag{F.6}$$

for quadratic approximation. By taking the sum of the squared error, equation F.4, equation F.7 can be used to determine the coefficients d. This is the same as the least squares method.

$$E = \sum_{i=1}^{k} \varepsilon_i^2 = \sum_{i=1}^{k} \left(f_i - \tilde{f}_i \right)^2 = \sum_{i=1}^{k} \left[f_i - \left(d_0 + \sum_{j=1}^{l} d_j \xi_{ij} \right) \right]^2 \tag{F.7}$$

Applying the following condition to minimise the error,

$$\frac{\partial E}{\partial d_j} = 0, \quad j = 0 \text{ to } l \tag{F.8}$$

the coefficients, d, is determined by solving the system of equations in equation F.9.

$$\begin{bmatrix} k & \sum_{i=1}^{k} \xi_{i1} & \sum_{i=1}^{k} \xi_{i2} & \cdots & \sum_{i=1}^{k} \xi_{il} \\ \sum_{i=1}^{k} \xi_{i1} & \sum_{i=1}^{k} \xi_{i1}^2 & \sum_{i=1}^{k} \xi_{i1}\xi_{i2} & \cdots & \sum_{i=1}^{k} \xi_{i1}\xi_{il} \\ \vdots & \vdots & \vdots & \vdots & \vdots \\ \sum_{i=1}^{k} \xi_{il} & \sum_{i=1}^{k} \xi_{il}\xi_{i1} & \sum_{i=1}^{k} \xi_{il}\xi_{i2} & \cdots & \sum_{i=1}^{k} \xi_{il}^2 \end{bmatrix} \begin{bmatrix} d_0 \\ d_1 \\ \vdots \\ d_l \end{bmatrix} = \begin{bmatrix} \sum_{i=1}^{k} f_i \\ \sum_{i=1}^{k} \xi_{i1} f_i \\ \vdots \\ \sum_{i=1}^{k} \xi_{il} f_i \end{bmatrix} \tag{F.9}$$

Knowing the coefficients, the function for the response surface can be made, by inserting the coefficients in equation F.5 and replacing ξ with the design variables. To avoid numerically instability of equation F.9, it is useful to normalise the variables. The normalisation procedure used is given by equation F.10, where ξ is transformed to w having a value between -1 and 1.

$$w_j = \frac{\xi_j - \left[\max\limits_m(\xi_{mj}) + \min\limits_m(\xi_{mj}) \right] / 2}{\left[\max\limits_m(\xi_{mj}) - \min\limits_m(\xi_{mj}) \right] / 2} \tag{F.10}$$

As mentioned earlier, a series of simulations needs to be conducted at different sampling points to create the meta model. Therefore it is a must that a robust simulation is established that can predict the SEA of the honeycomb structure, when the design variables is changed.

F.1.2 Error Evaluation

Since the RSM is an approximation of the response surface, the relative error (RE) between the simulation and the approximation is calculated as.

$$RE = \frac{\tilde{f}(x_i) - f(x_i)}{f(x_i)} \tag{F.11}$$

To check the accuracy of $\tilde{f}$, the coefficient of determination (R^2) and the adjusted R^2 (R^2_{adj}) equation, is determined, see equation F.12. The closer these values are to 1, the better.

$$R^2 = 1 - \frac{\text{SSE}}{\text{SST}} \quad \text{and} \quad R^2_{\text{adj}} = 1 - \frac{\left(1 - R^2\right) k - 1}{k - l - 1} \tag{F.12}$$

Where SSE and SST is the sum of squared errors and the total sum of squares, respectively [Fang et al., 2005]. These are given by,

$$SSE = \sum_{i=1}^{k} \left(f_i - \tilde{f}_i\right)^2 \quad \text{and} \quad SST = \sum_{i=1}^{k} \left(f_i - \overline{f}_i\right)^2 \tag{F.13}$$

where $\overline{f}_i$ is the mean value of the simulation results f_i.

F.2 Optimisation scheme

Depending on the number of design variables, different optimisation schemes might be favourable. If only two design variables are considered, it is possible to use graphical optimisation, where the optimum is found by the contour plot of the objective function together with the constrains.

If more design variables are introduced another optimisation scheme is needed. This could be applying the Karush-Kuhn-Tucker (KKT) conditions. For the KKT condition, the Lagrangian function is constructed, which include the objective function and constrains. The KKT conditions can also be used for two design variables or to check whether a point is the local optimum. To find the global maximum, all of the local maximums in the design space needs to be found. The highest value of these is the global maximum.

G — Anti intrusion plate and front bulkhead

To ensure a good design of an impact attenuator with the minimum mass, it is also necessary to consider the design of the front bulkhead and the anti intrusion plate. This is because of the testing requirements of the impact attenuator, where physical testing of the impact attenuator is required before it can be approved. As stated in section 1.2, it is required that the test fixture has geometry, stiffness and strength representative of the intended chassis. Meaning that the test fixture should consist of the impact attenuator, the anti intrusion plate, the front bulkhead and supporting tubes resembling that of the chassis, where:

"No part of the anti intrusion plate may permanently deflect more than 25mm beyond the position of the AIP before the test" [FSG, 2020].

Previous test of the front bulkhead and anti intrusion plate with a honeycomb impact attenuator has resulted in failure, see figure G.1. These tests were made with an impact attenuator following the minimum dimensions i.e. 200 mm $\times$ 100 mm, placed in the centre of the anti intrusion plate. Where the front bulkhead is made of 25 mm $\times$ 25 mm square tubes, that has a thickness of 1.5 mm. Whereas the anti intrusion plate is a steel plate that has a length of 361 mm, a width of 310 mm and a thickness of 1.5 mm, which extends to the centreline of the front bulkhead tubing.

Figure G.1: Picture taken after the test of a honeycomb impact attenuator were performed [Hansen et al., 2018].

From figure G.1, it is clear that severe failure of the front bulkhead occurs. Therefore an analysis of the front bulkhead and anti intrusion plate is made.

G.1 Front bulkhead simulation

To analyse the front bulkhead, simplification of the front bulkhead support is made. The front bulkhead support, is the connection between the chassis and front bulkhead. This connection is simplified to four, 50 mm long round tubes, with a diameter of 25 mm and a thickness of 1.5 mm. Whereas the current connection between the front bulkhead and the rest of the chassis is comprised of several tubes with different dimensions. Furthermore, it is decided to use the same tubes for the Front bulkhead, as is used for the current chassis design i.e. square tubes with a cross-section of 25 mm × 25 mm × 1.5 mm. The current front bulkhead support and front bulkhead is made in steel grade S235. Therefore it is decided to model these parts with a similar material model. For the anti intrusion plate, a 1.5 mm solid steel plate or 4.0 mm solid aluminium plate satisfying the requirement of maximum 25 mm permanent deflection during the test, must be integrated into the impact attenuator. Here it is chosen to use a 4.0 mm solid aluminium plate.

With the use of precrushed honeycombs, the crushing is assumed to occur at a constant force, providing a reliable energy absorption. Since the rules prescribe the maximum mean load to be 60 kN and with the use of precrushed honeycombs, it is assumed that the maximum load the anti intrusion plate and the front bulkhead is subjected to is also 60 kN. Based on these considerations, the simulation is set-up as in Figure G.2. Where the front bulkhead support is fixed in both displacement and rotation and a uniformly distributed load of 60 kN is applied to the anti intrusion plate.

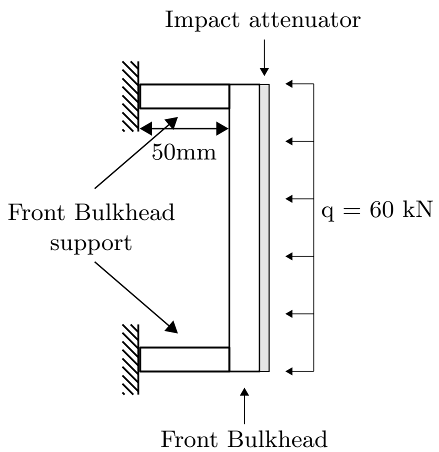

Figure G.2: Simulation set-up of the front bulkhead with the fixed boundary conditions and uniformly distributed load.

With this set-up in ANSYS Workbench, a contact formulation is made to model a bolt connection between the aluminium anti intrusion plate and the steel front bulkhead. Where a bonded contact formulation is used i.e. no sliding or separation is allowed between the faces. All the parts in the analysis are modelled with solid elements, while large deflections are taken into account, where the solver is using a full Newton-Raphson method.

From this simulation it is seen that stress singularities occur, near the tube connection to the front bulkhead, see Figure G.3. Beside the singularities, the maximum stress occurs at the middle of the 200 mm long front bulkhead beams. Where the equivalent stress reaches approximately 390 MPa, exceeding the yield stress of the material. This is in accordance with the previous test of the front bulkhead, where the longest front bulkhead tubes failed in the middle, see figure G.1. As for the anti intrusion plate, the equivalent stress reaches stresses of 187 MPa. However the largest deflection is in the middle of the anti intrusion plate, where a deflection of 0.858 mm is obtained.

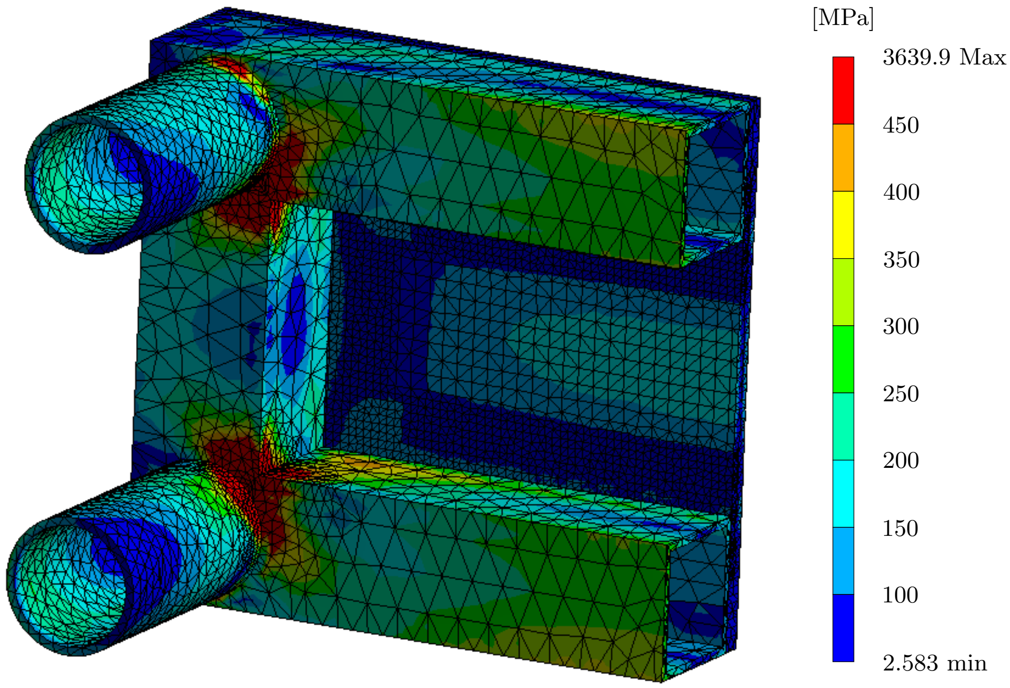

Figure G.3: Section view of the von Mises stress plot of the front bulkhead simulation with a 4 mm thick aluminium anti intrusion plate. Deformation is the true scale.

Therefore it is possible that the front bulkhead and anti intrusion plate does not fail in the impact test, with these smaller dimensions. However, by increasing the thickness of the front bulkhead tubes from 1.5 mm to 2.0 mm, and changing the material from S235 to S355, the maximum equivalent stresses becomes 302 MPa in the front bulkhead tubes. Whereas the equivalent stress in the anti intrusion plates, decreases to 167 MPa, with a maximum displacement of 0.65 mm. This change in dimensions reduces the equivalent stresses below the yield stress of S355, but increases the mass of the front bulkhead.

These simulations are based on the assumption that the load applied to front bulkhead and anti intrusion plate, does not exceed 60 kN. Therefore it is needed to do physical testing of this set-up to verify the crushing strength of the optimised impact attenuator while it also is a requirement in the rules. However, based on these results, it is seen that the front bulkhead and anti intrusion plate should not have a permanent deflection of more than 25 mm, with the current dimensions of the front bulkhead, while there should be no permanent deflection if the thickness of the tubes in the bulkhead is increased to 2 mm.